Structure and Function of the Yeast Metabolic Filament CTP Synthase

Jesse Michael Hansen

A dissertation
submitted in partial fulfillment of the
requirements for the degree of

Doctor of Philosophy

University of Washington
2022

Reading Committee: Justin M. Kollman, PhD, Chair
Dr. James B Hurley, PhD
Dr. Kelly Lee, PhD

Program Authorized to Offer Degree: Biochemistry

©Copyright 2022
Jesse M. Hansen

University of Washington

Abstract

Structure and Function of the Yeast Metabolic Filament CTP Synthase

Jesse M. Hansen

Chair of the Supervisory Committee:
Justin M. Kollman, PhD
Biochemistry

Many metabolic enzymes self-assemble into micron-scale filaments to organize and regulate metabolism. The appearance of these assemblies often coincides with large metabolic changes as in development, cancer, and stress. Yeast undergo cytoplasmic acidification upon starvation, triggering the assembly of many metabolic enzymes into filaments. However, it is unclear how these filaments assemble at the molecular level and what their role is in the yeast starvation response. CTP Synthase (CTPS) assembles into metabolic filaments across many species. Here, we characterize *in vitro* polymerization and investigate *in vivo* consequences of CTPS assembly in yeast. Cryo-EM structures reveal a pH-sensitive assembly mechanism and highly ordered filament bundles that stabilize an inactive state of the enzyme, features unique to yeast CTPS. Disruption of filaments in cells with non-assembly or pH-insensitive mutations decreases growth rate, reflecting the importance of regulated CTPS filament assembly in homeotstasis.

Acknowledgements

Raising two adorable children and earning a PhD in biochemistry have been two of the greatest challenges in my life so far, particularly since they were accomplished simultaneously. Those who have helped me to reach this point deserve acknowledgement. To my supervisor and friend, Justin Kollman, I thank you for your patience and guidance while I grew scientifically through these years and for the reminders that scientific research is hard work but with practice gets easier. Thank you for your helpful perspective when I needed it, and for teaching me how to frame my results in the bigger picture. Finally, thank you for encouraging and helping us move to Seattle, we will miss this city. From the bottom of my heart I thank my wife Kim. Thank you for putting up with my endless blathering about science and for joining me on this adventure together. Thank you for always loving me. Thank you to my kids, Ethan and Ella, whose bright smiles and laughs cheered me up after long days in the lab. Thank you to the members of the Kollman lab, past and present, many of whom have helped me to get to where I am today. In particular, a lab mate and good friend Eric Lynch, who taught me to be meticulous in every experiment I do. Thank you to my friends Dan and Kayla for helping us survive life with two small kids, and for all the fun we had together. Thank you to my friends in university family housing, a community which we were fortunate to have met and will miss dearly. Thank you to my brother Justen for his support. Thank you to my mom for the constant love and encouragement through these years, and to my second father Frank for his endlessly kind heart and support through every transition Kim and I make in life. Thank you all.

Dedication

This thesis is dedicated both to my oldest brother Aaron and to my father. From a young age, Aaron taught me the value of science and math. Bookshelves in his room filled with textbooks on science and engineering where I was free to open them and learn about our world. He patiently taught me that light is both a particle and a wave, and that nothing in the universe can move faster than light. This instilled in me at an early age an awe of nature and a profound respect for science. Aaron thoughtfully prepared daily math quizzes to nurture my academic ambition, even though I didn’t always enjoy it. I can see today he puts the same love and attention in with his three children. His support and encouragement are a cornerstone in me obtaining a PhD and for that I thank him deeply. To my father, who earned his PhD in philosophy many years ago, I thank for teaching me to question everything and to value truth over all else, if there is such a thing. Our conversations formed the curious and skeptical person I am today. He passed away many years before our children were born and prior to me even applying to a PhD program, but I like to think that he would be happy to see all that I’ve accomplished today. I love you dad.

List of Figures

List of Tables

Chapter 1: Introduction

1.1. Metabolic Filaments

Intermediate metabolism is finely tuned, carefully balanced, and robustly adaptable to changes in environmental conditions. More than a century of effort has gone into understanding the connections between pathways, the individual enzymes that drive the biochemistry, and the regulation of metabolic flux. Only recently, however, have we come to appreciate the role of metabolic enzyme self-assembly as a widespread mechanism of metabolic organization and regulation (Lynch and Kollman, 2020; Park and Horton, 2019; Simonet et al., 2020). These assemblies have been found in many core pathways including glycolysis (Kemp, 1971; Webb et al., 2017), fatty acid synthesis (Hunkeler et al., 2018; Kleinschmidt et al., 1969), amino acid synthesis (Cohen et al., 1976; Frey et al., 1975; Miller et al., 1974; Petrovska et al., 2014; Zhang et al., 2018), and nucleotide synthesis (Barry et al., 2014; Carcamo et al., 2011). Metabolic enzymes that form filaments are frequently found at rate-limiting and energetically committed steps of pathways, suggesting filaments play a role in regulating metabolic flux (Noree et al., 2019). Indeed, for most enzyme polymers that have been functionally characterized, assembly functions as a mechanism of allosteric regulation to tune enzyme activity (Barry et al., 2014; Hunkeler et al., 2018; Johnson and Kollman, 2020; Lynch et al., 2017; Lynch and Kollman, 2020; Stoddard et al., 2020).

1.2. Glutamine amidotransferases

Glutamine is a remarkably versatile metabolite. Access to nitrogen is a core challenge for many organisms, since it is an essential building block for biological molecules. However, free ammonia is potentially toxic to cells and therefore requires a mechanism of intracellular transport. Maintaining the balance of cytosolic ammonia is carried out by glutamine synthase through the generation of an ammonia-carrying intermediate – glutamine. Glutamine's side chain amide acts as a nitrogen source for the *de novo* synthesis of many nitrogen-containing biomolecules. Such metabolites include nucleotides (purines and pyrimidines), amino acids (asparagine, histidine, tryptophan, serine, alanine), aminated sugars, coenzymes, and some charged tRNAs (Massière and Badet-Denisot, 1998; Richards, Nigel G. J. et al., 2010). For this reason, glutamine is the most abundant free amino acid in the body (Purich, 1998).

Glutamine amidotransferase enzymes catalyze the cleavage of glutamine's amide side chain into ammonia, and its subsequent ligation to a substrate. This process occurs in two active sites which catalyze two distinct reactions. Modular domains separate activities, and in many cases there is a substrate channel connecting the active sites to avoid release of the intermediate free ammonia (Binda et al., 2000; Huang et al., 2001; Lynch and Kollman, 2020; Mouilleron and Golinelli-Pimpaneau, 2007; Thoden et al., 1999; Weeks et al., 2006). Another reason for a channel is to prevent the protonation of ammonia, since ammonium is not a good substrate for the synthase reaction (Huang et al., 2001). The glutamine amide transfer (GAT) domain is where glutamine is hydrolyzed, and the synthase domain is where the acceptor substrate sits (Buchanan, 1973).

There are three classes of glutamine amido-transferases which are known to hydrolyze glutamine's amide bond. The most common are class 1 glutaminases, which use a conserved Cys/Glu/His triad. There is a high degree of conservation of class 1 glutaminases since they bind the same glutamine substrate; this is further evidence that this domain evolved from a common evolutionary ancestor (Richards, Nigel G. J. et al., 2010). The reaction mechanism is as follows. Glutamine's amide bond undergoes a nucleophilic attack from the conserved cysteine's thiol group, creating a tetrahedral intermediate which is stabilized by nearby backbone nitrogens (Rishavy et al., 2000; Roux and Walsh, 1992; Thoden et al., 1999). The active site histidine protonates the side chain nitrogen, creating a good leaving group which can self-cleave to release ammonia (Richards, Nigel G. J. et al., 2010). The active site glutamic acid serves to correctly position the histidine in the active site (Massière and Badet-Denisot, 1998). The Cys/His triad is then regenerated through hydrolysis of the thioester connecting cysteine and glutamine, releasing glutamate.

Class 2 glutaminase domains use an amino-terminal cysteine to attack the amide bond (Massière and Badet-Denisot, 1998), generating a tetrahedral intermediate which is stabilized by a nearby "oxyanion hole" (Boehlein et al., 1997). Class 3 glutaminases are only found in glutamine-tRNA and instead use a serine residue for hydrolysis (Curnow et al., 1997). Of the three classes, class 1 are the most common and therefore the best characterized.

The second half of the glutamine amido-transferase process is the amination of an electrophilic substrate via a synthase reaction. Unlike the glutaminase reaction, this ligase reaction often proceeds via ATP-dependent activation of the substrate or ATP-dependent stabilization of the final product (Massière and Badet-Denisot, 1998). The lone electron pair of free ammonia creates a good nucleophile for the attack and displacement of a substrate leaving group. In contrast to the high structural conservation observed in class 1 glutaminase domains, synthase domains vary widely due to their ability to bind different substrates.

pH plays an important role in both the glutaminase and amido-ligase reactions. Class 1 glutaminases rely on protonation of the conserved histidine to generate the free ammonia group, and therefore this histidine must be in a state of protonation which occurs near or below physiological pH. Conversely, the ammonia substrate behaves poorly at lower pH when it is protonated ammonium. For this reason, some glutamine amido-transferases can have optimal activity near neutral pH when glutamine is used as substrate and almost no activity for free ammonia due to its protonation (Levitzki and Koshland, 1971). However at a more basic pH the enzymatic activity for ammonia can be drastically higher than the glutamine substrate.

1.3. Biochemistry of CTP Synthase

CTP Synthase (CTPS) is a class 1 glutamine amidotransferase, catalyzing the ATP-dependent amidiation of uridine triphosphate (UTP) to cytidine triphosphate (CTP) (**Figure 1.1a**). This reaction is the rate-limiting step in the *de novo* synthesis of CTP (Lieberman, 1956). Under normal conditions CTP is the least abundant of the four major ribonucleotides (Traut, 1994), suggesting that this reaction is tightly regulated. CTPS is regulated allosterically by nucleotides (Long and Pardee, 1967), through post-translational modifications (Choi et al., 2003; Park et al., 1999) and through quaternary assembly (Barry et al., 2014; Lynch et al., 2017; Lynch and Kollman, 2020; Zhou et al., 2021). The product CTP is an essential precursor for DNA, RNA, and CMP-linked phospholipids (Chang and Carman, 2008; Fairbanks et al., 1995; Traut and Evans, 1988). CTPS biochemistry and structure have been studied extensively, making it an ideal model enzyme for exploring the role of polymer assembly in regulating activity.

CTPS was first identified as the enzyme responsible for catalytic UTP amidation (Lieberman, 1956) just two years after the initial discovery of CTP in rat carcinomas (Schmitz et al., 1954). These early studies also established the role of ATP (and magnesium) as an energy source for the CTPS reaction. Initial studies on CTPS showed that ammonia can be used during catalysis, but it was later shown that glutamine, a more biologically appropriate molecule, can be substituted as a nitrogen source (Hurlbert and Kammen, 1960). These authors also established that low levels of GTP act as an allosteric enhancer of the reaction when glutamine is used. However it wasn’t until many years later that it was discovered that high levels of GTP actually inhibit activity (MacDonnell et al., 2004). Finally, last year it was demonstrated that GTP exerts its effect by filling a hole in the ammonia channel, thereby preventing ammonia leakage (Zhou et al., 2021). Enzyme kinetic studies of purified *E. coli* enzyme demonstrated that CTPS is subject to regulatory control by its substrates and negative feedback by its product CTP (Long and Pardee, 1967). These early studies laid the foundation of CTPS biochemistry by establishing reaction substrates UTP, ATP, and glutamine (or ammonia), and the dependence of low levels of GTP (**Figure 1.1a**). Taken together, CTPS began to emerge as a central regulatory node in metabolism, integrating regulatory signals of all four major ribonucleotides – UTP, ATP, GTP, and CTP.

Each CTPS monomer consists of a glutaminase domain and an amido-ligase domain connected by an α-helical linker (**Figure 1.1b**). In the amido-ligase domain, the γ-phosphate from ATP is transferred to the C4 oxygen of UTP, generating an iminophsophate (4-phosphoryl) intermediate (Lewis and Villafranca, 1989; von der Saal et al., 1985). Substrate binding induces rotation of the glutaminase domain which opens an ammonia channel between active sites (Lynch and Kollman, 2020). Then through an addition-elimination reaction with ammonia, this intermediate is converted to CTP and free phosphate. CTPS assembles X-shaped, D2 symmetric homotetramers through interactions of the amido-ligase domains, with multiple protomers participating in each substrate and regulatory binding site (**Figure 1.1c**). These D2 tetramers are the basic protomers which then stack one atop another in order to assemble CTPS filaments (**Figure 1.1d-e**).

1.4. Human CTP Synthase

Humans possess two isoforms of CTPS (hCTPS1 and hCTPS2) which are 74% identical in amino acid sequence. hCTPS1 appears to be particularly important in activated lymphocytes, where a loss-of-function mutation manifests as a life-threatening immunodeficiency (Martin et al., 2014). The observation that this is the only clinical manifestation of hCTPS1 disruption suggests hCTPS1's primary function is in these lymphocytic cells, despite measurable RNA levels in a variety of human tissues (Fagerberg et al., 2014). The corollary of this role of hCTPS1 in propagating an adaptive immune response is that it has become a target for antagonists to treat certain inflammatory diseases (Lynch et al., 2021; Sakamoto et al., 2017). In fact, inhibition of *de novo* pyrimidine pathways have been proposed for almost two decades as a possible means of overcoming allograft host rejection (Allison and Eugui, 1993; Dayton et al., 1992).

Cryo-EM structures of hCTPS1 provided the first molecular mechanism by which filaments assemble in eukaryotes (Lynch et al., 2017). Polymer assembly occurs at an α-helical insert in the glutaminase domain which is only present in eukaryotes (**Figure 1.1d-f**). This contact is largely mediated by a conserved histidine (H355) which abolishes assembly when mutated. hCTPS1 tetramers have the capacity to assemble polymers only when in the active substrate-bound conformation, suggesting that filaments are composed entirely of enzymatically active protomers (Lynch et al., 2017). This is hypothesized to maintain the active conformation churning out CTP to keep up with the increased metabolic demand in rapidly proliferating lymphocytes.

On the other hand, less is known about the physiological role of hCTPS2. Similar to hCTPS1, RNA levels are detectable in a variety of human tissues (Fagerberg et al., 2014), and therefore likely acts as the housekeeping isoform for CTP production throughout the body. hCTPS2 polymers assemble at the same conserved α-helical contact, however filaments can assemble in either substrate or product-bound states (Lynch and Kollman, 2020). These polymers dynamically switch between active and inactive states in a highly cooperative way which is hypothesized to respond to subtle fluctuations in cytoplasmic nucleotide pools. This isoform is further regulated through phosphorylation of the c-terminal region, which has been shown to have an inhibitory effect (Kassel et al., 2010) on activity. Interestingly, this region is near the filament assembly interface, suggesting a possible connection between phosphorylation and polymer assembly or stability.

Human CTPS expression and/or activity has been repeatedly demonstrated to be upregulated in malignant cancers (Kizaki et al., 1980; Maehara et al., 1982; van den BERG et al., 1993; Williams et al., 1978). Human CTPS filaments have been observed *via* fluorescent tagging in cancer cells (Carcamo et al., 2011; Chang et al., 2017). CTPS levels have even been suggested as a reliable biochemical marker to assess the aggressiveness of malignant lymphomas (Ellims et al., 1983; Rambotti, 1985). The proliferative phenotype of cancer cells require high nucleotide levels to maintain the increased metabolic demand. Making things worse, the associated increase in cellular CTP pools has been linked to further mutagenesis (Meuth, 1989). This is bad both for cancer prognosis and for the likelihood of therapeutic resistance. There has been a striking involvement of CTPS in lymphoproliferative cancers, leukemia and lymphoma (Berg et al., 1995; Fairbanks et al., 1995; Rambotti, 1985; van den Berg et al., 1994; van den BERG et al., 1993; Verschuur et al., 2000, 1998). This is likely due to the important role hCTPS1 plays in these specific cell types. This suggests that selective inhibition of this isoform may be a particularly promising therapeutic avenue. For more than 40 years CTPS has been explored as a viable drug target aimed at reducing nucleotide pools in rapidly proliferating cells (Brockman et al., 1975) however their efficacy has been limited by toxicity or drug resistance.

1.5. CTP Synthase Filaments in non-Human Organisms

Cellular CTPS filament assembly is widespread across the domains of life, having been observed in bacteria, archaea, and eukaryotes (Carcamo et al., 2011; Ingerson-Mahar et al., 2010; Liu, 2010; Noree et al., 2010; Zhou et al., 2021). We have previously shown that there are striking differences between the assembly mechanisms and filament architectures among species. These differences give rise to differences in function, with bacterial CTPS filaments providing a mechanism to allosterically inhibit the enzyme, while animal CTPS filaments act to increase activity and cooperativity of regulation (Barry et al., 2014; Lynch et al., 2017; Lynch and Kollman, 2020; Zhou et al., 2021, 2019).

Polymers formed by CTPS in *Escherichia coli* (*E. coli*) are the best characterized bacterial CTPS filament. In stark contrast to human CTPS1, *E. coli* CTPS tetramers only become filament-assembly competent when bound to the reaction product CTP (Barry et al., 2014). As a result, filaments assemble in the product-bound inactive conformation. Rather than assembling at the conserved eukaryotic interface they assemble via the α-helix linker (**Figure 1.1d**) (Barry et al., 2014). Here the role of polymers may act as a quaternary regulatory mechanism to sequester the enzyme when cytoplasmic CTP is in excess. Mutating the polymerization interface leads to an increase in CTP pools *in vivo* and an associated defect in growth (Barry et al., 2014).

The model organism *Drosophila melanogaster* assembles large rod-like foci during metabolic changes that accompany development or as part of a stress response (Azzam and Liu, 2013; Liu, 2010; Wu and Liu, 2019). Similar to human CTPS 2, *D. melanogaster* CTPS filaments assemble distinct substrate or product-bound polymers, although the reason for this remains unclear (Zhou et al., 2019). Nonetheless, it has been demonstrated that polymers are essential in normal development (Simonet et al., 2020; Strochlic et al., 2014). These findings point to an involvement of CTPS polymers in modulating circumstances of dramatic metabolic change, an emerging theme in filament-mediated regulation.

The bacterium *Caulobacter crescentus* CTPS has co-opted the CTPS filament to alter cell morphology. Through interaction with the intermediate filament crescentin, CTPS filaments serve bifunctional roles to regulate cell morphology in addition to generating *de novo* CTP (Ingerson-Mahar et al., 2010). CTPS assembles foci in plants as well. The plant *Arabidopsis thaliana* has five isoforms of CTPS, at least three of which form foci of varying shapes (Daumann et al., 2018). Interestingly, these plant CTPSs did not assemble foci when expressed in yeast cells, suggesting interacting partners which may direct large-scale assembly in plants. Even the extremophile archaea *Haloarcula hispanica* has been shown to assemble CTPS foci in what appears to be a response to osmotic stress (Zhou et al., 2020).

Given the apparent central role of CTP in all kingdoms of life, it is no surprise that it's biosynthetic enzyme CTPS has also been targeted by humans for selective inhibition in pathogenic bacteria and parasites. Examples of organisms validated or justified as targets include *Mycobacterium tuberculosis* (Chiarelli et al., 2018), *Streptococcus pneumonia* (Yoshida et al., 2012), *Trypanosoma brucei* (Hofer et al., 2001; Tamborini et al., 2012), *Helicobacter pylori* (Mendz et al., 1994), *Giardia intestinalis* (JimÉnez and O'sullivan, 1994), and *Chlamydia trachomatis* (Wylie et al., 1996). However, in most of these cases it is not demonstrated whether CTPS assembles polymers or, if so, whether these polymers modulate enzymatic activity. Investigating such behavior will be crucial in making progress on treatment in such organisms.

1.6. CTP Synthase bundles and co-localization with other enzymes

Fluorescence-based studies of tagged CTPS in yeast and other organisms demonstrated large foci or rods consistent with laterally associating filaments (Ingerson-Mahar et al., 2010; Liu, 2010), yet there are no high-resolution structures of bundled metabolic enzymes in any organism. These large foci or rods often serve as the identifier for filament assembly in cellular studies, but individual filaments are clearly below the resolution limits of such studies. Therefore, the relationship between individual filaments and large fluorescently-tagged cellular structures remains unclear. If fluorescent foci are indeed laterally associating filaments, it is not known whether they assemble non-specifically or with ordered repeating contacts. Low resolution cryo-EM tomography of *C. crescentus* CTPS revealed that polymers do indeed appear to associate laterally in an apparently organized way (Ingerson-Mahar et al., 2010). It has also been shown that small foci can undergo serial fusions, a finding consistent with growing lateral association of filaments (Gou et al., 2014). However, it is unclear whether lateral association mediates a specific function *in vivo* or whether bundling has an effect on catalytic turnover. Therefore it is important to also study the higher-order structures which filaments form.

In cellular fluorescence studies, tagged CTPS foci have repeatedly been shown to co-localize with similarly tagged metabolic enzymes. This raises the possibility that filaments or bundles provide a mechanism for direct physical interaction of enzymes for coordinated regulation of different pathways. Asparagine synthase not only co-localizes with CTPS in *S. cerevisiae*, but also influences the extent to which CTPS polymers assemble (Zhang et al., 2021). Under stress, CTPS strongly co-localizes with IMPDH in human cells (Carcamo et al., 2011; Chang et al., 2018; Keppeke et al., 2015) but not in yeast (Noree et al., 2019). However, yeast CTPS does co-localize with Prs5p, a metabolic enzyme involved in upstream nucleotide biosynthesis (Noree et al., 2019). CTPS co-localizes with the glycogen debranching enzyme Gdb1p, possibly linking pyrimidine biosynthesis with carbohydrate consumption (Noree et al., 2019). Co-localization of metabolic foci is frequently reported but there is currently very little indication for how or why such a process occurs.

1.7. Yeast Stress Response

The budding yeast (*Saccharomyces cerevisiae*) and fission yeast (*Saccharomyces pombe*) have played an instrumental role in human history through their uses in bread making and alcohol fermentation for thousands of years. However, these single-celled organisms are also commonly used as surrogate tools to study fundamental and conserved biological processes. These fungi share many of the core metabolic pathways which evolved early in life, making yeast a simplified but biologically intact system for studying these pathways. Their well studied genome and the relatively short life cycle have made yeast a highly tractable system for functional gene studies (Botstein et al., 1997). *S. cerevisiae* was the first eukaryotic genome sequenced (Goffeau et al., 1996) and despite 1 billion years of divergent evolution a quarter of its genes have human homologues (Jiang et al., 2006). For these reasons, both budding and fission yeast are conveniently used as model organisms to study, among other biological processes, aging (Zhang and Cao, 2017), cancer (Simon and Bedalov, 2004), and stress (Hansen et al., 2021; Petrovska et al., 2014). Here, we use budding yeast as a model organism to study stress-related metabolic enzyme re-organization into filaments.

Yeast prefer glucose or fructose as their primary carbon source but when starved of these carbon sources must undergo complex metabolic reprogramming. A central step in such reprogramming is the phosphorylation-based inhibition of eIF2α, resulting in attenuation of protein synthesis as the cell enters a state of dormancy (Postnikoff et al., 2017). Other yeast pathways involved in stress-related nutrient sensing include Ras-cAMP signaling and TOR signaling (Winderickx et al., 2003). A major consequence of starvation in yeast is intracellular acidification. Without energy, yeast membrane-bound proton pumps fail and the neutral cytoplasm is acidified (Orij et al., 2009). When deprived of glucose, cytoplasmic pH has been measured to go as low as 5.8 (Munder et al., 2016). This acidification triggers the assembly of many core metabolic enzymes into filaments and foci (Narayanaswamy et al., 2009; Noree et al., 2010; Petrovska et al., 2014;

Shen et al., 2016). For example, low pH is necessary and sufficient for glutamine synthase filament assembly, a process which protects cells and permits rapid growth upon readdition of nutrients (Petrovska et al., 2014). It is hypothesized that polymerization leads to increased cytoplasmic viscosity, limiting diffusion of metabolites and slowing growth (Petrovska et al., 2014). CTPS assembles stress-induced filaments in both budding yeast (Noree et al., 2010; Petrovska et al., 2014; Shen et al., 2016) and fission yeast (Andreadis et al., 2019; Li et al., 2018; Zhang and Liu, 2019). The precise molecular basis of assembly is unknown for CTPS, or any metabolic filament in yeast, and it remains an open question how polymerization of these enzymes is protective for the cell.

1.8. Yeast CTP Synthase

Yeast have two CTPS isoforms, Ura7 (Yang et al., 1994) and Ura8 (Nadkarni et al., 1995; Ozier-Kalogeropoulos et al., 1994), which share 78% identical residues. Yeast possessing only Ura7 have 78% normal cytoplasmic CTP levels, while the same measurement for Ura8 is 36% (Ozier-Kalogeropoulos et al., 1994). This may be explained by the observation that Ura7 mRNA is twofold more abundant than Ura8 *in vivo* (Nadkarni et al., 1995). Loss of either enzyme is detrimental to growth, while loss of both is lethal (Ozier-Kalogeropoulos et al., 1994). This suggests an overlapping role of isoforms but Ura7 may be the physiologically dominant isoform for CTP production in yeast.

Why does yeast, single celled organisms without capacity to pattern gene expression by tissue, express two isoforms of CTPS? One explanation for why yeast possess two functional copies of CTPS may reside in differences of their biochemical regulation. A notable difference between the yeast isoforms is the way they respond to cellular levels of substrates UTP and ATP: Ura7 exhibits cooperative kinetics while Ura8 exhibits saturation kinetics (Nadkarni et al., 1995). Further, the inhibitory concentration of product CTP is 3.5x higher for Ura7 than Ura8, (Nadkarni et al., 1995), perhaps further explaining why Ura7 is responsible for majority CTP production. Lastly, the optimal pH for activity differs between the two isoforms: Ura7 at pH 8.0 (Nadkarni et al., 1995), and Ura8 is pH 7.5 (Yang et al., 1994). To put this into perspective, yeast cytoplasm is maintained at a pH of between 7.0 and 7.4 (Orij et al., 2009). These differences in biochemical regulation of isoforms studied under identical conditions possibly reflects the different roles that these isoforms serve in different cellular conditions.

Native yeast CTPS is predominantly inactive dimers, which, in the presence of substrates UTP and ATP can shift equilibrium to favor a tetramerized active form (Long and Pardee, 1967; Nadkarni et al., 1995; Pappas et al., 1998; Yang et al., 1994). In response to stress, both isoforms assemble supramolecular structures in cells (Noree et al., 2010; Shen et al., 2016). Interestingly, both isoforms have been shown to co-localize very strongly in such studies, however whether the interaction is at the level of tetramer or the filament remains unclear.

An additional layer of CTPS regulation is derived from post-translational phosphorylation. Early studies on Ura7 revealed it is phosphorylation by protein kinases A and C (Nadkarni et al., 1995; Yang et al., 1996; Yang and Carman, 1996). Protein Kinase A (PKA) is the primary transducer of signals through RAS/cAMP, a pathway involved in nutrient sensing which is activated by glucose (Broach, 1991; Thevelein, 1994). Phosphorylation of Ura7 by PKA at Ser424 increases enzymatic turnover and reduces sensitivity to CTP inhibition (Yang and Carman, 1996). Protein kinase C (PKC), a secondary lipid messenger which mediates proliferation (Kaibuchi et al., 1985), also phosphorylates Ura7 at Ser424 and mutating this residue to alanine resulted in less membrane phospholipid production (Choi et al., 2003). PKC also activates Ura7 at S36, S354, and S454, while inactivating Ura7 at S330 (Park et al., 2003); these modifications correlated with phospholipid production *in vivo*.

Here, we investigate the structure and *in vivo* function of CTPS filaments in *S. cerevisiae*, hereafter referred to as “yeast”. We use cryogenic electron microscopy (cryo-EM) to determine the molecular mechanism of yeast CTPS filament assembly and higher-order bundled assemblies. The interface between tetramers in the yeast CTPS filament, which is unique among the existing CTPS filament structures, explains the pH sensitivity of assembly. Two engineered mutations at this assembly interface, one that disrupts filaments and one that stabilizes them, allow us to probe the functional role of filament assembly *in vitro* and *in vivo*. Yeast CTPS filaments stabilized a conformation that pinches shut the ammonia channel between catalytic sites, which reduces activity in the filament. Both non-assembling and pH-insensitive CTPS mutants lead to slowed proliferation, indicating the critical role of regulated CTPS assembly in both vegetative growth and recovery from starvation.

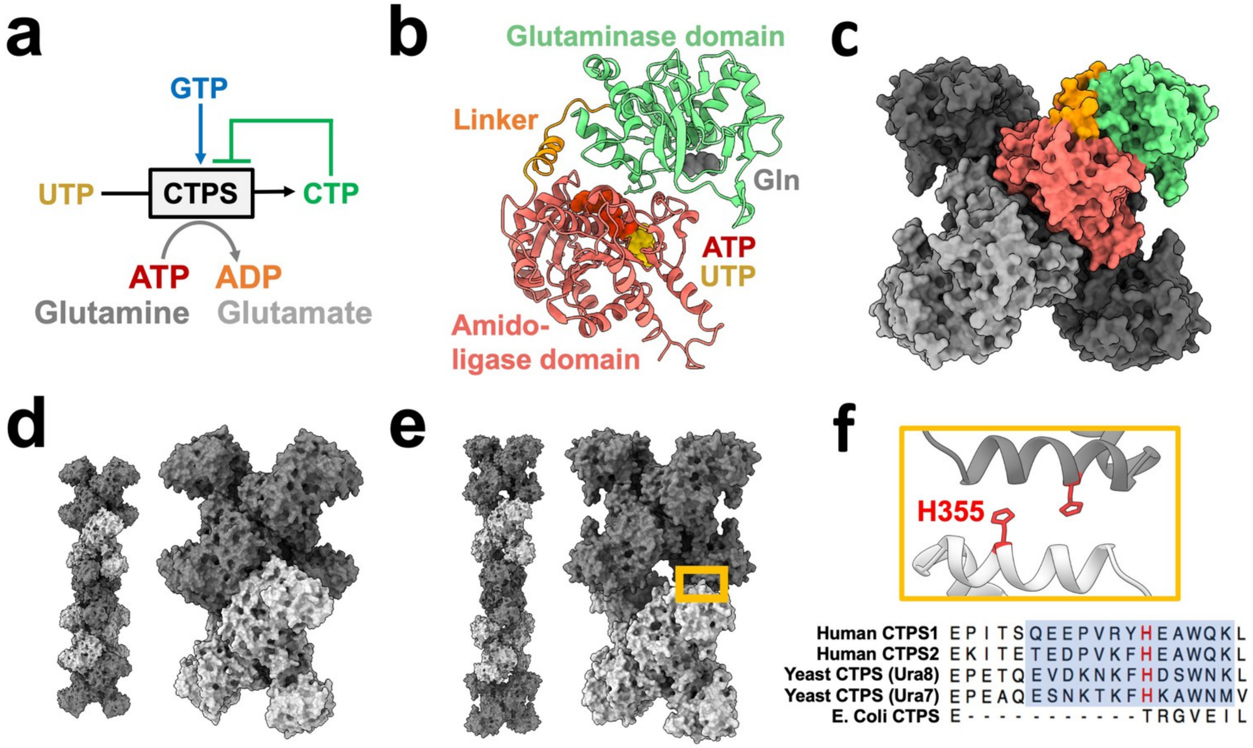

Figure 1.1: CTPS canonical structure and filament assembly. (a) *De novo* CTP synthesis reaction diagram. (b) Substrate-bound hCTPS2 (6PK4) monomer with glutamine modeled from 1VCO. (c) Canonical tetramer structure of CTPS (6PK4). Monomers are shaded differently, and domain colors from panel B are painted for one monomer. (d) Surface model display for filament assembly of stacked tetramers for product-bound E. coli CTPS (5U3C). (e) Surface model display for filament assembly of stacked tetramers for product-bound hCTPS2 (6PK7). (f) Zoom-in of box from panel E showing filament assembly interface, with conserved H355 in red. Below, sequence alignment of filament assembly interface, with blue shaded box for eukaryotic alpha helical insert and conserved key histidine in red.

Chapter 2: Results

2.1. Yeast CTPS filament assembly is pH-sensitive

It remains an open question whether pH-regulated assembly is an inherent feature of budding yeast CTPS, or whether other cellular factors are required for assembly. To address this, we first confirmed prior work that showed yeast CTPS assembles in cells upon cytoplasmic acidification (Petrovska et al., 2014); Ura7-GFP tagged at the endogenous locus forms foci upon nutrient deprivation (**Figure 2.1a**), or when cells are permeabilized with DNP (2,4-dinitrophenol) to manipulate cytoplasmic pH (**Figure 2.1b**). We next examined polymerization of purified recombinant Ura7 and Ura8 at different pHs by negative stain EM. Apo CTPS did not form polymers at any pH. At pH 7.4 both isoforms assembled short, single filaments on binding substrates or product, but pH 6.0 promoted assembly of much larger polymers that appeared to be bundled filaments (**Figure 2.1c, Figure 2.2**). We tested which nucleotides promoted assembly (**Figure 2.3**), and determined how salt influences polymer assembly (**Figure 2.4**). Thus, like other species (Barry et al., 2014; Lynch et al., 2017; Zhou et al., 2019), yeast CTPS assembly is dependent on ligand binding, and the pH sensitivity is intrinsic to the enzyme itself.

We wondered whether the intrinsic pH sensitivity of yeast CTPS was conserved among other species. Previous studies have not described the pH-sensitivity of human CTPS filament assembly, and have shown robust assembly at pH 8.0 (Lynch et al., 2017; Lynch and Kollman, 2020). The overall sequence conservation between human and yeast CTPS, and the presence of a histidine residue at the assembly interface in human CTPS filaments, led us to consider whether human CTPS assembly is also pH-dependent (**Figure 2.1d**). We observed equally robust polymerization of purified human CTPS2 (hCTPS2) at pH 6.0 and 8.0, and negative stain EM averages show that filaments formed at different pHs have similar architectures, suggesting that there is no direct effect of pH on hCTPS2 assembly or structure (**Figure 2.1d, inserts**). Thus, pH-driven assembly of CTPS appears to be specific to yeast, raising the question of what unique structural features might confer pH-sensitivity.

To assess the kinetics of pH-dependent CTPS assembly, we monitored right angle light scattering by CTPS after addition of CTP (**Figure 2.1e**). Both isoforms had very low signal at pH 7, consistent with our negative stain imaging. At pH 6, Ura8 assembly was much faster than Ura7, but inspection at early time points showed that both exhibited biphasic assembly which could not be fit with a single equation (**Figure 2.5**). Instead, early and late assembly kinetics fit well to separate four-parameter curves, indicating potentially distinct assembly phenomena with different kinetics in the early and late phases. We examined the growth of Ura7 filaments by negative stain EM over time, and found that single filaments appear at early time points and the thicker bundles at later time points, suggesting that the biphasic scattering kinetics can be explained by initial linear polymerization followed by lateral aggregation (**Figure 2.5**).

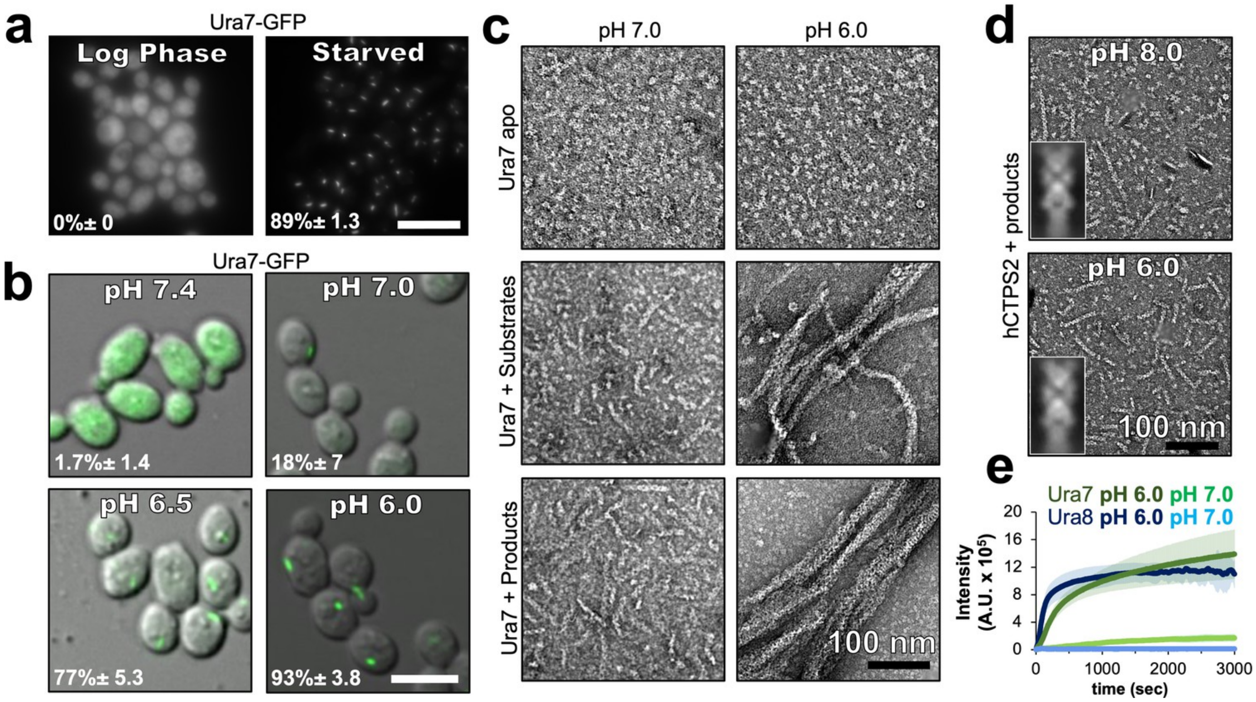

Figure 2.1: Yeast CTPS assembly is driven by pH with addition of substrates or products. (a) Yeast expressing GFP-tagged Ura7 in log phase and starvation media. Quantification is shown as a percentage of cells with foci. Scale bar 10 µm. (b) Yeast expressing GFP-tagged Ura7 with cell membrane permeabilized using 2 mM DNP supplemented with 2% glucose. Quantification is shown as a percentage of cells with foci. Scale bar 10 µm. (c) Negative stain EM of purified Ura7 assembled with substrate (2 mM UTP/ATP) or products (2 mM CTP). (d) Negative stain EM of purified hCTPS2 assembled with 2 mM CTP. Insets are representative 2D class averages. (e) Right angle light scattering with addition of 2 mM CTP. Units of intensity are in arbitrary units (A.U.).

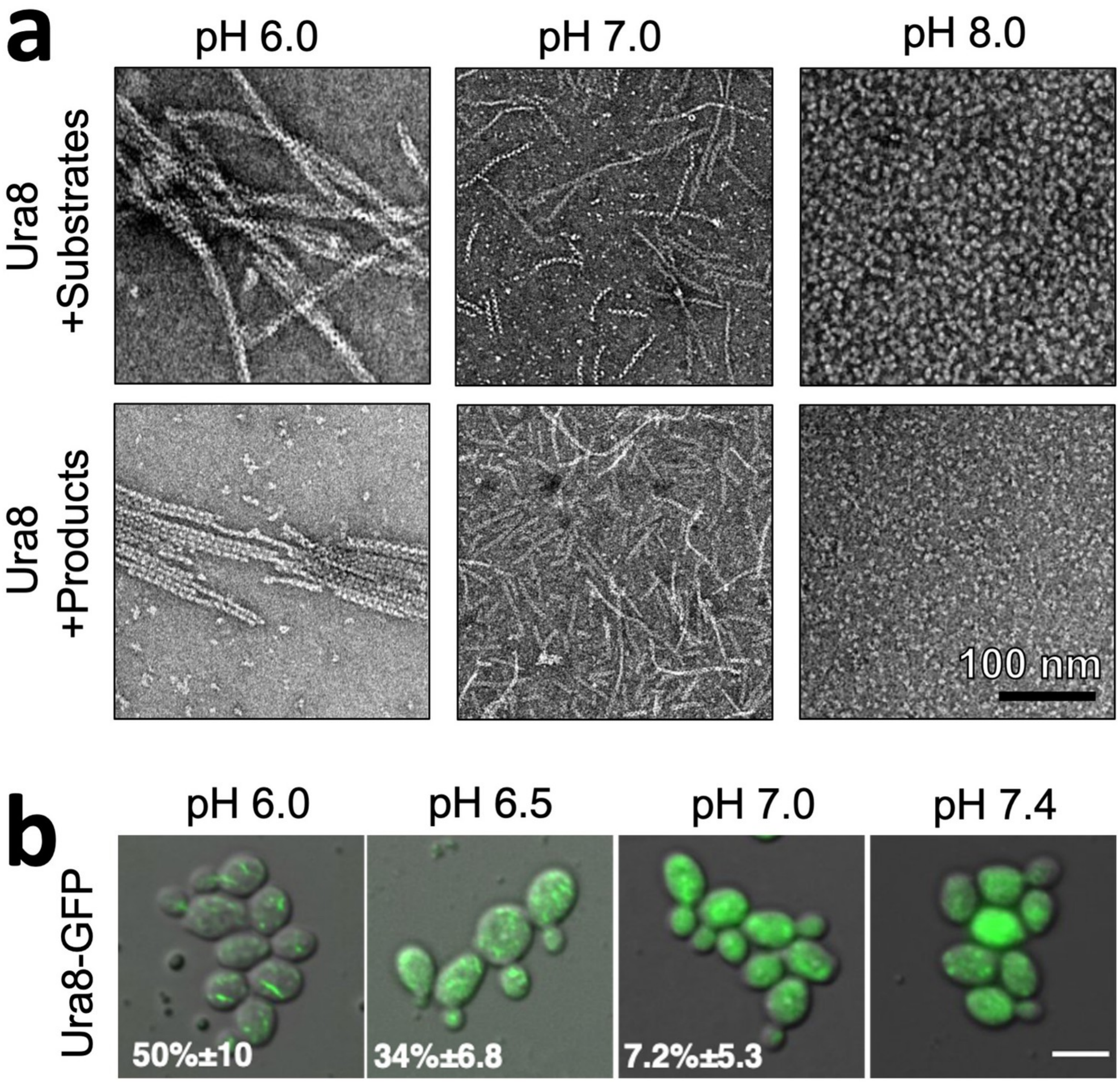

Figure 2.2: Ura8 assembly is driven by pH and substrates or products. (a) Negative stain EM of purified recombinant Ura8 assembled with substrates (2 mM UTP/2 mM ATP) or product (2 mM CTP). (b) Yeast expressing GFP-tagged Ura8 with membrane permeabilization using 2 mM DNP and supplemented with 2 % glucose. Scale bar is 5 µm.

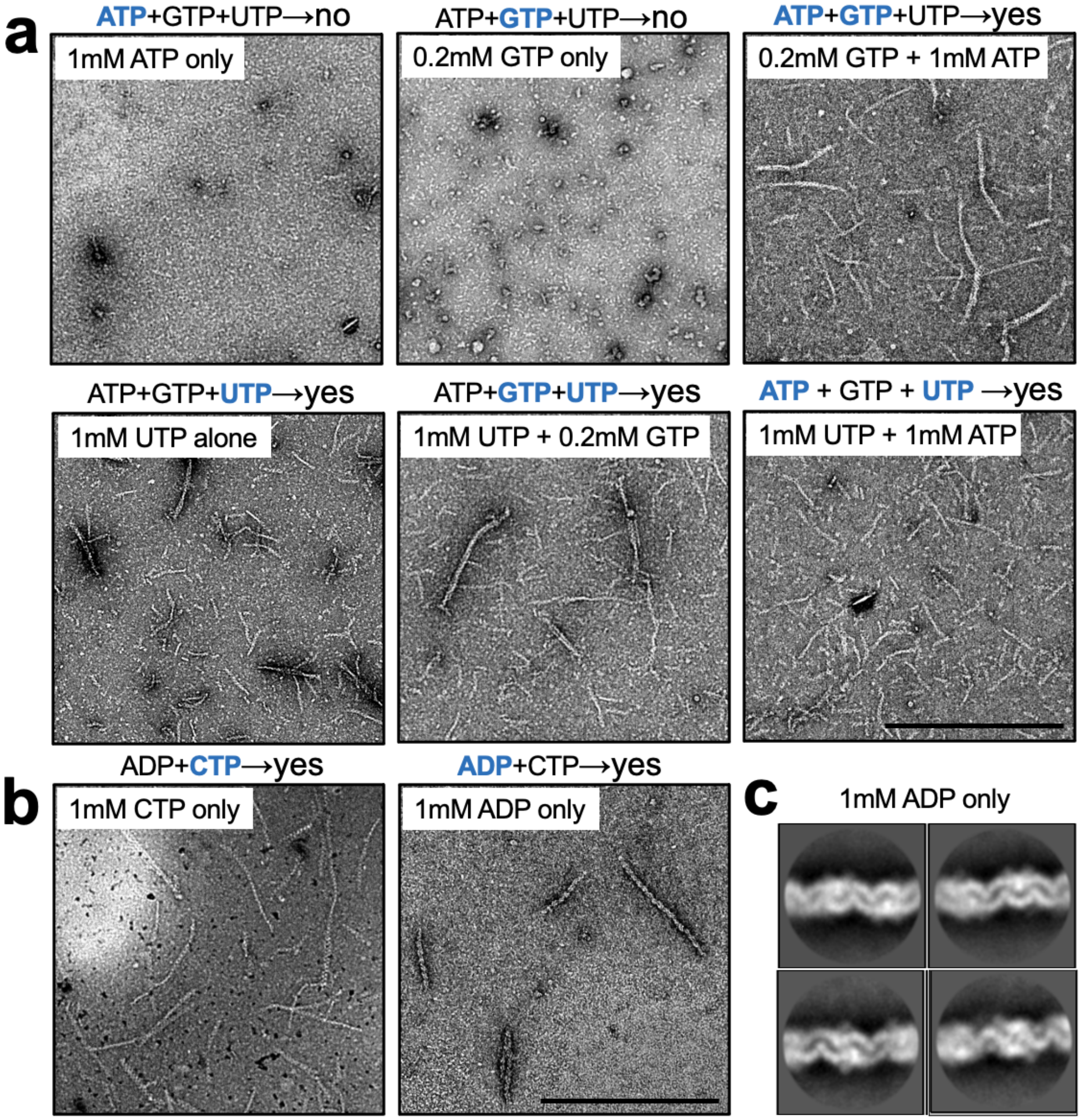

Figure 2.3: CTPS filament assembly by various nucleotides. (a) Negative stain EM of 1uM Ura7, 50mM NaCl, MES 50mM buffer pH 6.2 assembled at 30C for 15 minutes with various substrates alone or in combination. Yes/no denotes whether filaments were observed. When filament were observed, morphology was normal. Scale bar is 500nm. (b) Same as panel a, but assembled with products. Note that CTP+ADP appeared identical to CTP alone (not shown). Morphology for ADP-only filaments appeared unusual. (c) Representative 2D class average from negative stain EM of ADP-only filaments.

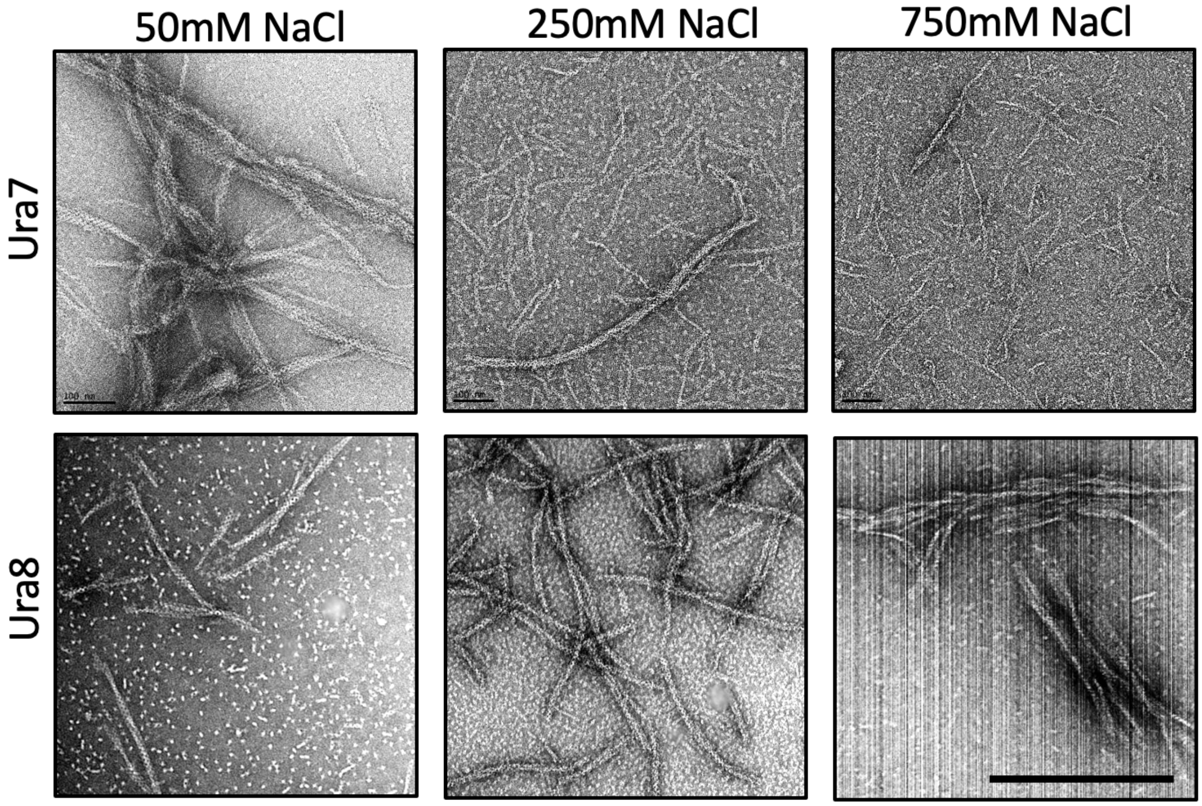

Figure 2.4: Salt-dependence of yeast CTP filament assemebly. 1mM CTPS assembled with products (1mM ADP/CTP, 5mM MgCl2) in 50mM MES pH 6.0. Scale bar is 200nm.

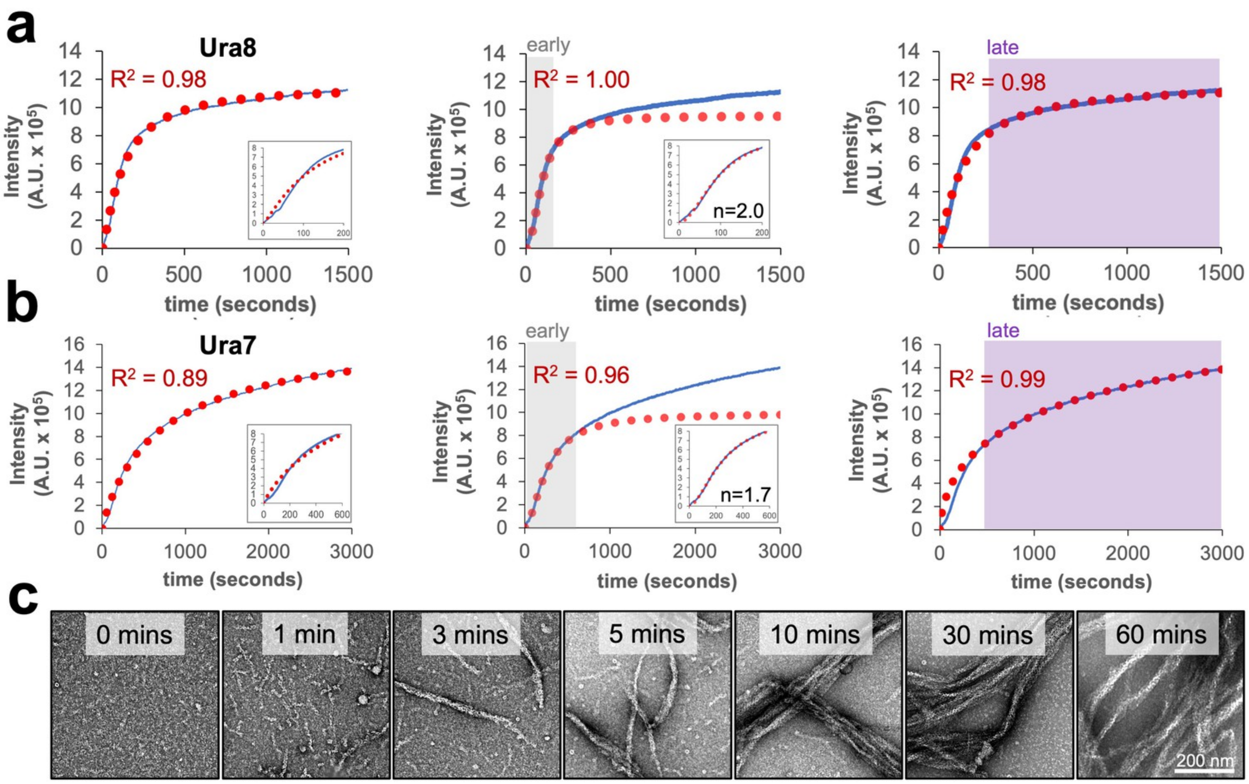

Figure 2.5: Right angle light scattering assembly kinetics for CTPS filaments. (a) Right angle light scattering (blue line) for product-driven Ura8 assembly at pH 6.0. A single four-parameter logistic regression (red dotted line) fit to the full data (left), early (middle; 0–300 s) or late (right; 300–1500 s) time-points. Insets show zoom in of early time points. R2 is the square of the Pearson product moment correlation coefficient, representing the quality of the fit. (b) Same as panel A but for Ura7. (c) Negative stain EM of Ura7 assembly from panel B.

2.2. Cryo EM Structures of yeast CTPS filaments

We next determined structures of individual CTPS filaments by cryo-EM. To enable structure determination, we assembled filaments at pH 6.5, where single filaments predominate over larger bundles. We solved filament structures of both Ura7 and Ura8 in substrate- (ATP and UTP) and product- (CTP) bound states. Ura8 yielded the highest resolution structures, at 2.8 Å (substrates) and 3.8 Å (products) (**Figure 3.1a, Table 1**). In the Ura8 structures, all ligands were clearly visible and bound as previously described for other CTPS homologs, including an imino-phosphate reaction intermediate recently observed in Drosophila CTPS, and the presence of two distinct CTP-binding sites per monomer recently reported in human and Drosophila CTPS (Endrizzi et al., 2004; Goto et al., 2004; Lynch et al., 2021, 2017; Lynch and Kollman, 2020; Zhou et al., 2021) (**Figure 3.2c**). Ura7 filaments reached lower resolutions, 7.3 Å (substrates) and 3.7 Å (products), but the overall structures were indistinguishable from Ura8 at these resolutions (**Figure 3.3, Table 2**). Because of their higher resolution which enabled building of atomic models, we focus subsequent structural interpretation on the Ura8 filaments.

Like other previously reported structures of human, *Drosophila*, and *E. coli* CTPS, the yeast enzyme assembles as stacked tetramers. However, it does so using a completely different interaction interface, which was the same in both substrate- and product-bound yeast structures (**Figure 3.1b**). Helix 356–370 in the glutaminase domain mediates interactions between tetramers, so that each protomer is involved in assembly contacts (**Figure 3.1b**). His360 interacts with D370 which would be stabilized by protonation of His360 at low pH, and likely explains the pH-sensitivity of the assembly interaction (**Figure 3.1b, Figure 3.4**). We see density consistent with two rotamer positions of H360 that may reflect partial protonation of the sidechain at pH 6.5. One rotamer that likely reflects the protonated state interacts with D370, and the other rotamer that likely reflects an unprotonated state forms a hydrogen bond to a backbone carbonyl across the interface (**Figure 3.4a–c**). Additional contacts include hydrogen bonding between an asparagine pair on the two-fold symmetry axis (Asn364), hydrogen bonding (Gln352) to a backbone carbonyl across the interface, hydrophobic interactions of a cluster of tryptophans (Trp363, Trp392), and a pair of salt bridges (Lys391, Glu395) (**Figure 3.1b, Figure 3.3**). Helix 356–370 also forms the assembly interface of animal CTPS filaments, but the yeast interface is shifted by two turns of the helix, resulting in completely different residue contacts (**Figure 3.1c**). This leads to a larger interaction interface in yeast CTPS filaments (706 $Å^2$ per monomer in product-bound filaments) than in the human homolog (492 $Å^2$ per monomer in product-bound filaments) (**Figure 3.5**). Sequence differences between human and yeast CTPS at residues 364, 391, and 395 may explain how the unique yeast interface arose, which shifted H360 into a position to mediate a pH-sensitive interaction.

The primary difference between the substrate- and product-bound filament structures is the conformation of individual CTPS protomers. Active and inactive conformations of CTPS are characterized by a ~ 7° rotation of the glutaminase domain relative to the amido-ligase domain, which opens an ammonia channel between the two active sites in a single protomer (Lynch and Kollman, 2020). The Ura8 product-bound filament is in the canonical inhibited conformation, but the substrate-bound structure is in a conformation intermediate between canonical active and inhibited states, in which the ammonia channel remains closed. This suggested to us that one function of yeast CTPS filaments is to constrain the enzyme in a low activity conformation. To test this hypothesis, we determined the structure of free Ura8 tetramers at pH 7.4 bound to substrates at 2.8 Å resolution. In this unassembled state, Ura8 adopts the canonical active conformation, very similar to hCTPS2, including opening of the ammonia channel and rearrangement at the tetramerization interface (**Figure 3.1d–h, Figure 3.6**).

The active state we observe in free tetramers is incompatible with filament assembly, because in this conformation filament interfaces cannot be occupied on both sides of the tetramer simultaneously (**Figure 3.7**). Indeed, the major source of heterogeneity in single Ura7-substrate filaments, which were flexible and short, are tetramers that only make one contact at each paired assembly interface. This leads to tetramers in the active, substrate-bound conformation tethered to each other through single glutaminase domain interactions (**Figure 3.7d**). Thus, filament assembly with symmetric contacts acts as a steric constraint to trap yeast CTPS in a low activity conformation, while tethering through a single glutaminase domain supports short, flexible filaments that accommodate a fully active conformation.

There was ambiguity in certain side chain density in the substrate channels of our cryo-EM maps, preventing us from obtaining a detailed molecular description of this region. We set out to crystallize Ura7 in the active conformation with the goal of improving atomic detail within the channel. To improve crystallization efforts and favor crystal lattice formation over filament assembly contacts, we mutated the filament contact H360 to alanine (**Figure 4.1a**). To further improve packing we removed a potentially problematic loop and the C-terminal region which was partly disordered in our cryo-EM structures. Crystals were grown in the presence of substrates except glutamine in order to lock CTPS in the active conformation. Surprisingly, Ura7 in our crystal structure was in the inactive conformation (**Figure 3.8**). Optimization of ligands did not improve results and we did not pursue this crystallization further.

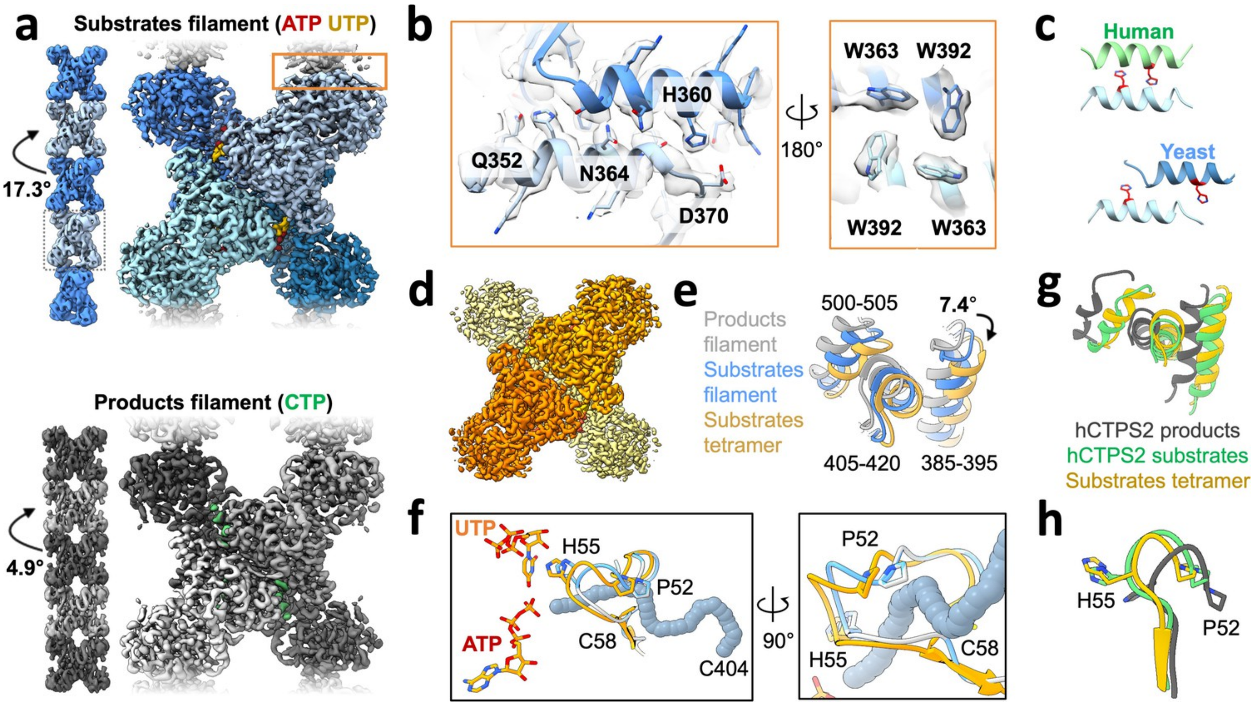

Figure 3.1: Yeast CTPS assembles distinct filaments which are not in the canonical active conformation. (a) Cryo-EM maps of Ura8 filaments assembled at pH 6.0 in the presence of substrates (top; UTP and ATP) or product (bottom; CTP). Left, filament map from imposing helical symmetry parameters on a reconstruction of a single protomer, and low-pass filtered to 15 Å. Dotted box delineates an individual tetramer. (b) Zoom-in of the filament assembly interface (orange box in panel A) with superimposed cryo-EM density. Key residues are indicated. Right panel is the back-side view of the interface. (c) Comparison of human and yeast interface, with H360 (H355 in humans) highlighted in red. (d) Cryo-EM map of substrate-bound (ATP,UTP) tetramer at pH 7.4. (e) Glutaminase domain rotation (residues indicated) of monomers aligned on the amido-ligase domain. (f) Substrate-channel (gray tube) beginning at catalytic C404 ending at ligands UTP/ATP. Color scheme same as panel E. (g) Ura8 substrate-bound tetramer glutaminase domain rotation relative to hCTPS2 substrate (6PK4) and product-bound (6PK7) filaments. (h) Loop movements near the active site which alleviates constriction in the substrate-channel. Color scheme same as panel G.

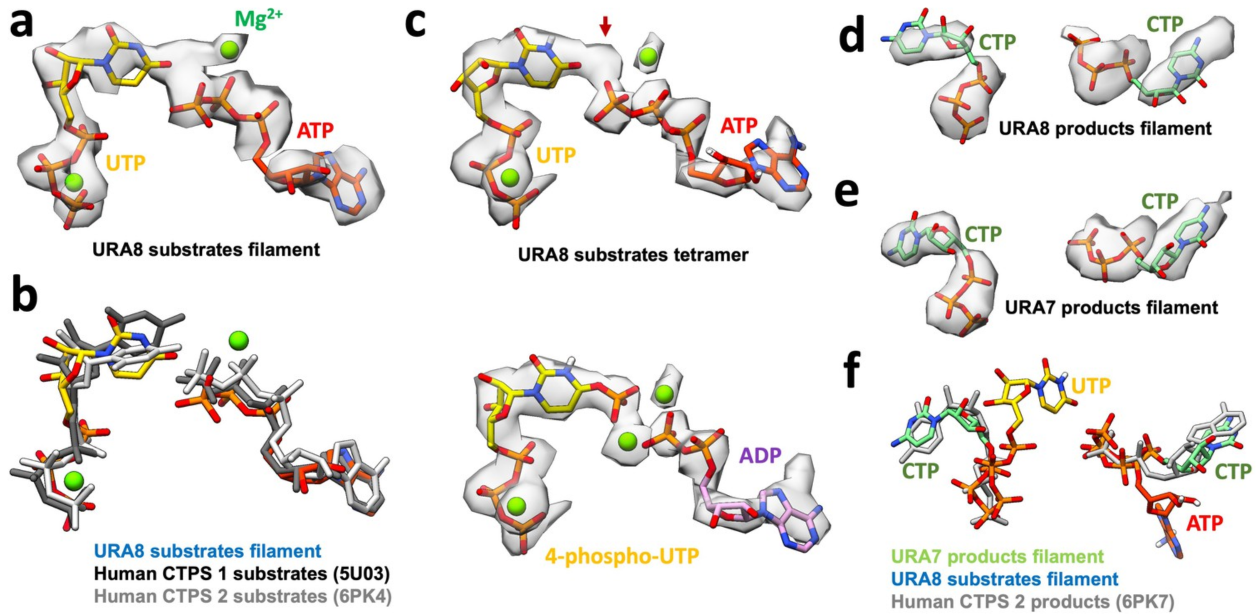

Figure 3.2: Nucleotides in yeast CTPS. (a) Ura8 bound to ATP/UTP in filament with corresponding map density. (b) Comparison of model from panel A to published human CTPS 1 and 2 bound to substrates. (c) Ura8 bound to ATP/UTP in tetramer with corresponding map density. Arrow shows extra unknown density. Bottom panel shows the same density modeled with hydrolyzed ATP, yielding a 4-phospho-UTP intermediate in the active site. (d)(–e) CTP-bound URA8 and URA7 in filaments with corresponding density. (f) Overlay of product-bound Ura7 from panel E with published product-bound human CTPS2. Substrate-bound Ura8 filament ATP and UTP are displayed to show relative positioning of products and substrates in the active site.

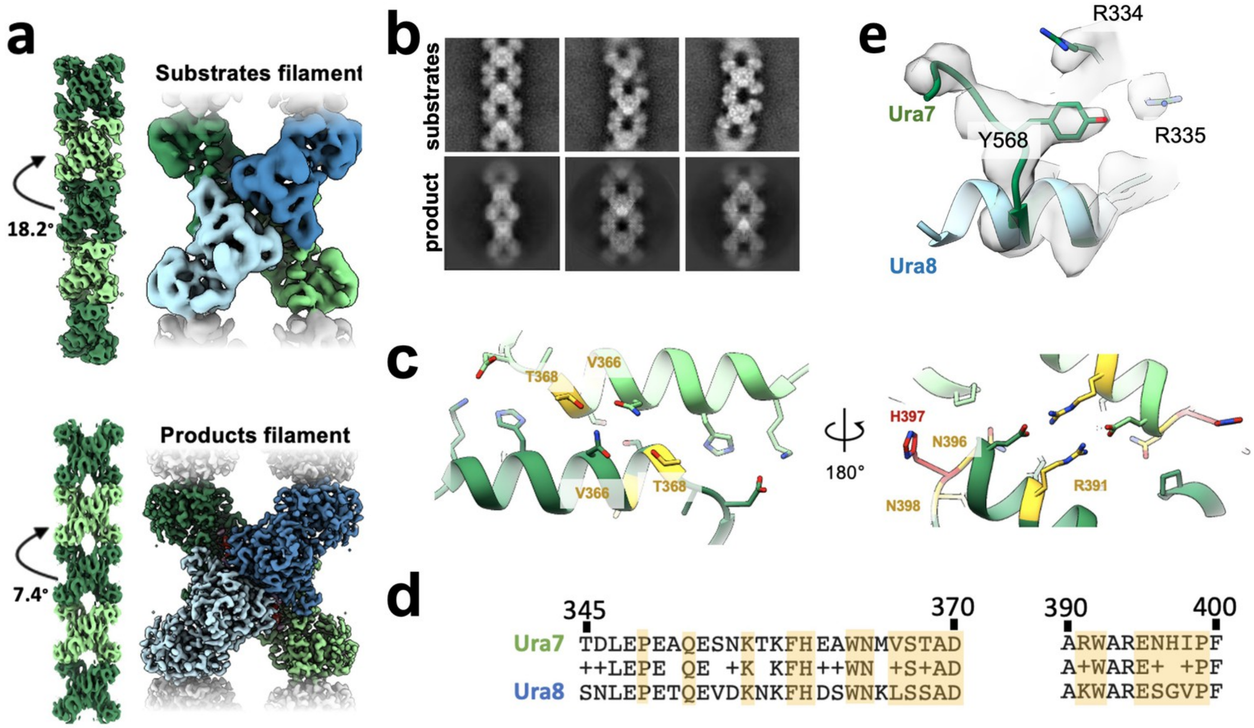

Figure 3.3: Ura7 filament architecture and assembly interface. (a) Cryo-EM reconstructions of Ura7 in substrate and product bound states. Left are maps generated from imposing helical symmetry parameters on a reconstruction of a single protomer. (b) Selected 2D class averages of substrate- or product-bound Ura7. (c) Ura7 filament interface. Residues painted similar (yellow) and different (red) from Ura8. In addition, Ura7 assembles with the W363/W392 hydrophobic core shown in Figure 3.1. (d) Sequence alignment of filament assembly interface for Ura7 (top) and Ura8 (bottom). Residues participating in interface assembly are highlighted in yellow.

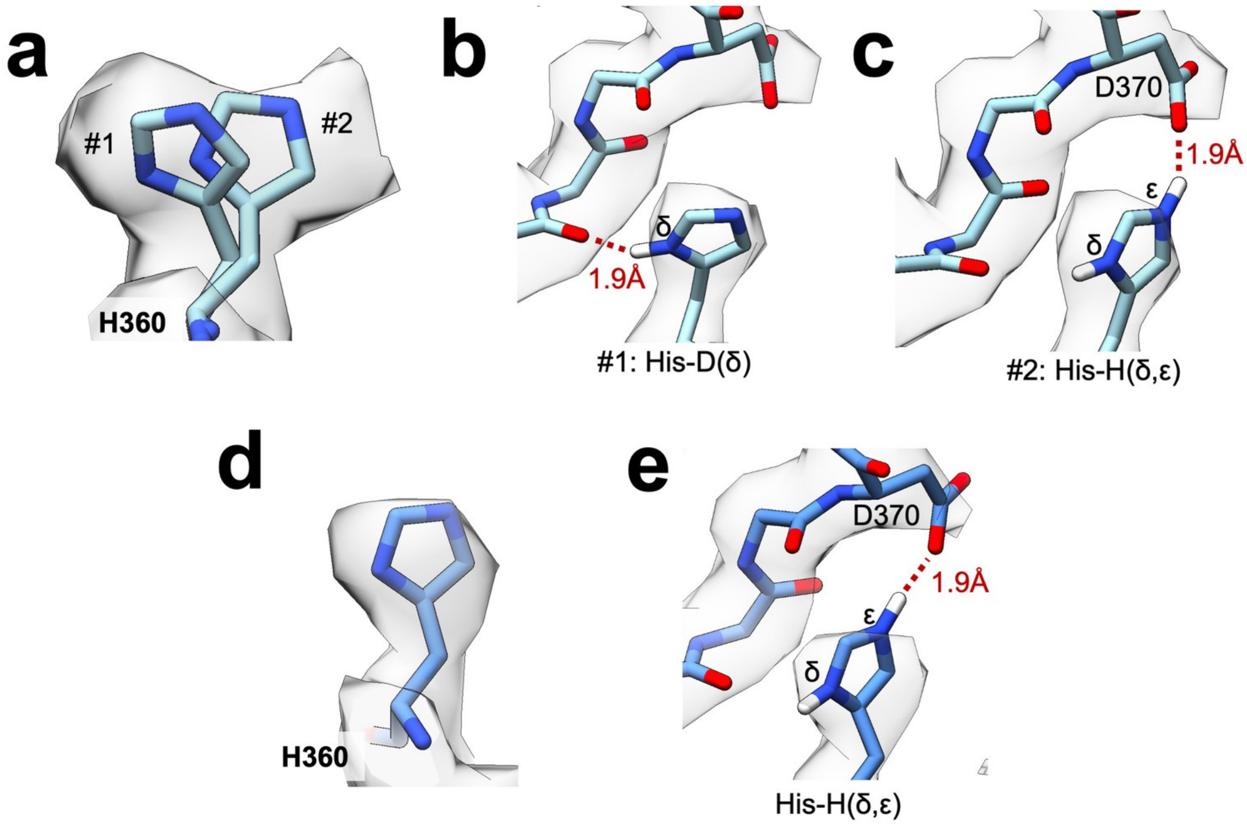

Figure 3.4: Protonation state at the filament assembly interface. (a) Substrate-bound Ura8 filament map density for H360 with two possible rotamers modeled. Note that this view is rotated slightly relative to panels b-c. (b) Single-protonation state (His-D) of H360 hydrogen of rotamer #1 from panel A bonding with a backbone carbonyl across the interface. (c) Double-protonation state (His-H) of rotamer #2 from panel A driven by low pH leads to an ionic interaction of epsilon hydrogen with D370. (d) Similar to panel A, for His360 from substrate-bound Ura8 bundle. (e) Double-protonation state of H360 making an ionic interaction with D370 in substrate-bound Ura8 bundle.

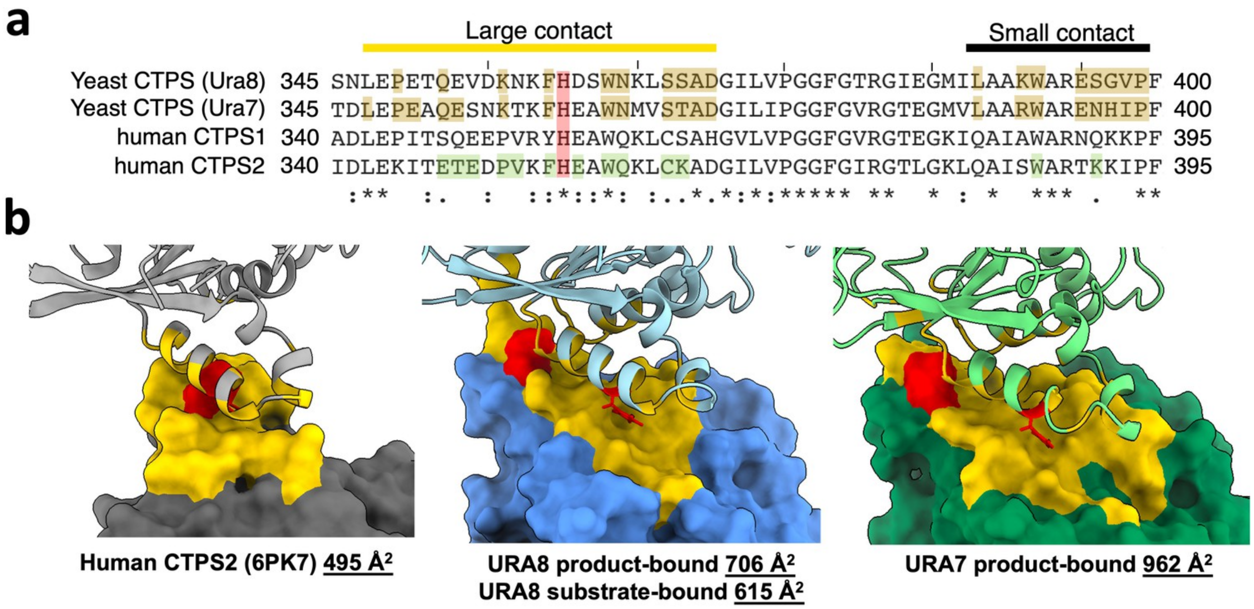

Figure 3.5: Comparison of buried surface area for yeast and human CTPS. (a) Sequence alignment of filament assembly interface for human and yeast isoforms. Residues highlighted in brown and green correspond to filament assembly contacts for yeast and human CTPS, respectively. Conserved histidine highlighted in red. (b) Calculated buried surface area for one monomer of human or yeast CTPS with interfacing residues painted yellow. H360 (H355 in humans) is colored in red.

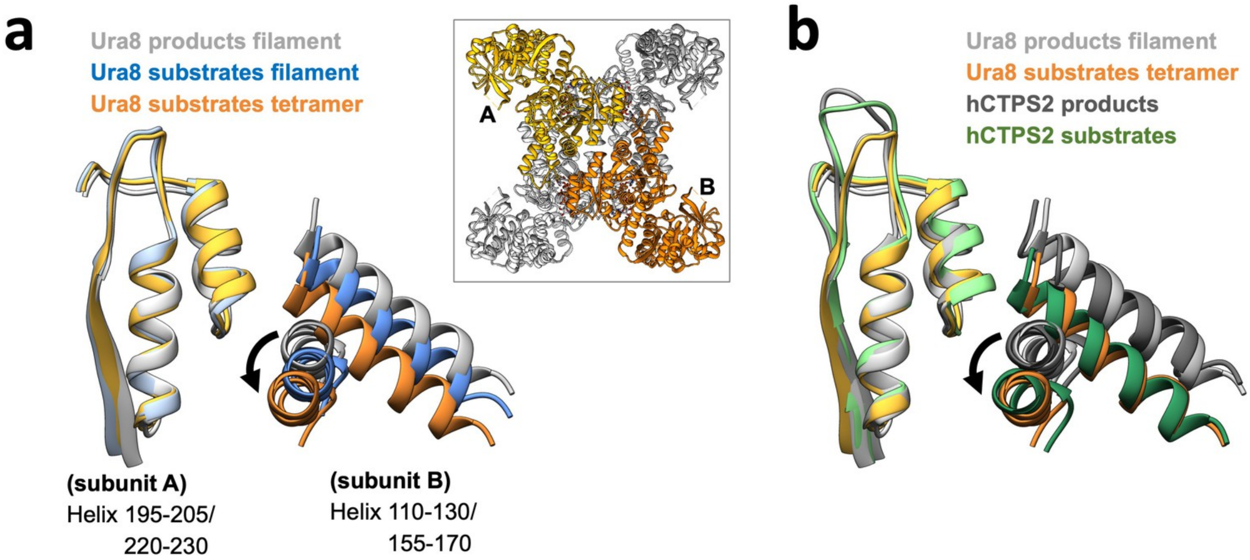

Figure 3.6: Amido-ligase domain movement at the tetramerization interface. (a) Helices at the tetramerization interface for a transverse pair of monomers (A and B in inset). Models aligned on subunit A helices (left) to show relative movement of subunit B. (b) Models of yeast CTPS (Ura8) helices from panel A shown relative to published human CTPS2 (6PK4 substrates; 6PK7 products).

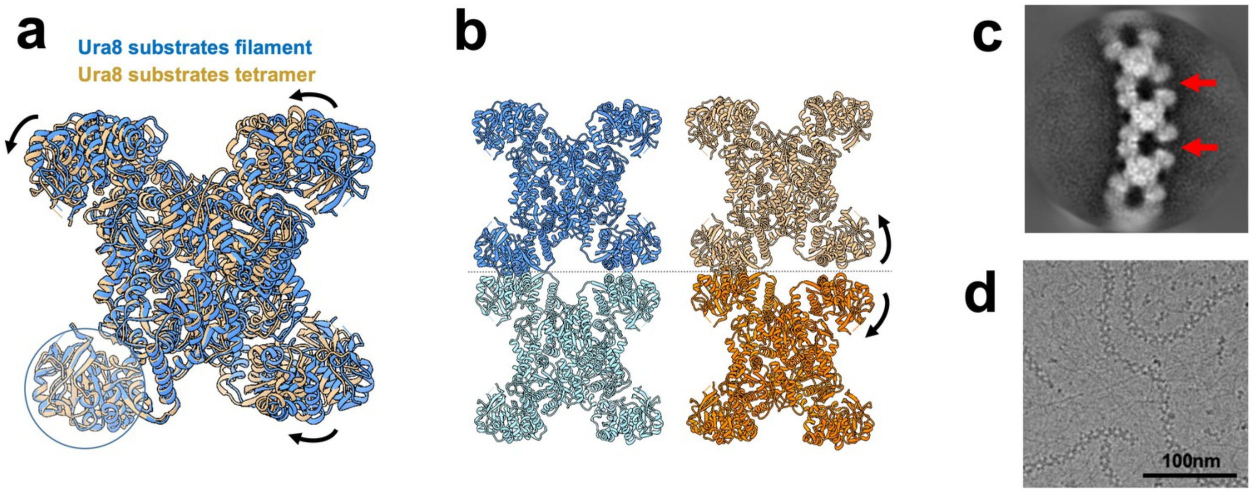

Figure 3.7: CTPS filaments are incompatible with the active state. (a) Tetramer models for substrate-bound Ura8 in a filament (low pH) or unassembled (high pH). Models aligned on the glutaminase domain for one monomer (circled) and the resulting movement is shown with arrows. (b) Substrate-bound Ura8 filament (blue, left) used for alignment of two substrate-bound tetramers (right) on the contacting glutaminase domains as done in panel A. When tetramers are aligned on the left glutaminase domain, the opposing (right) interface splays open, disrupting filament architecture. (c) Representative 2D class average of substrate-bound Ura7 showing breaking of filaments described in panel B. (d) Example cryo-EM micrograph of substrate-bound Ura7 at low pH.

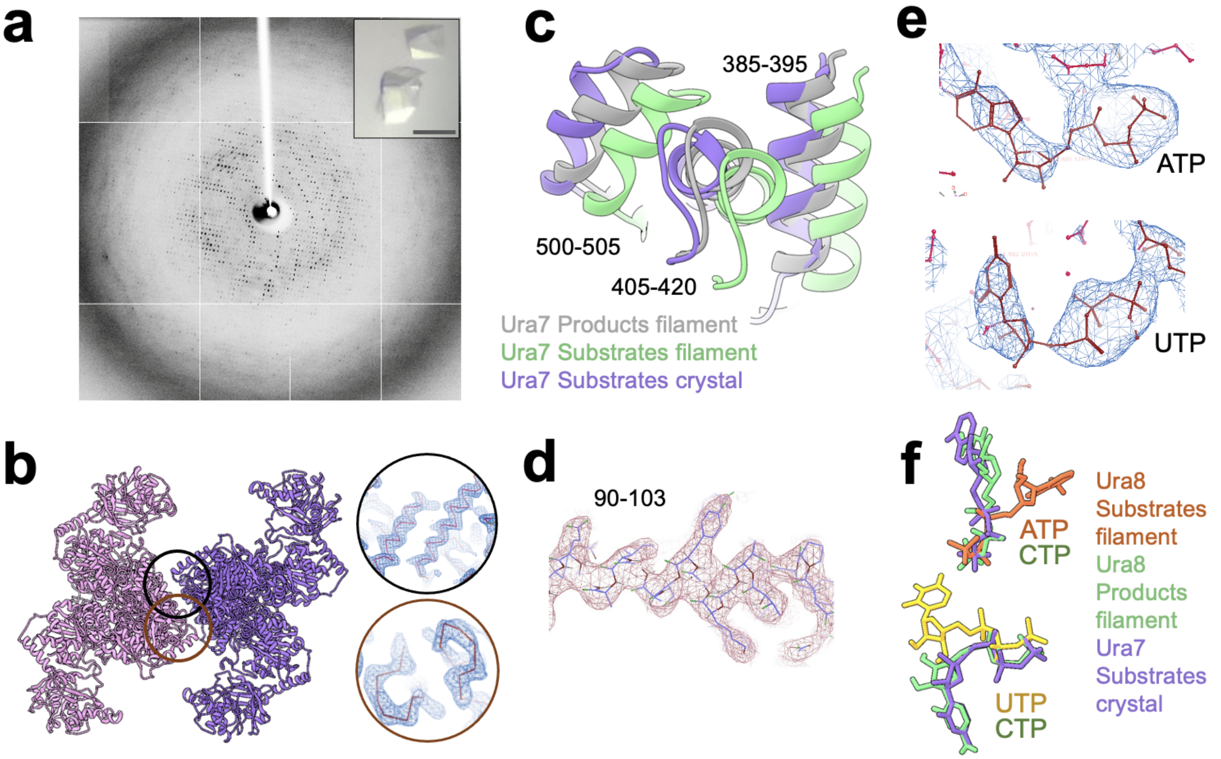

Figure 3.8: Substrate-bound Ura7 Crystal Structure. (a) X-ray diffraction of crystal shown in inset. Scale bar is 0.3mm. (b) crystal packing contacts for two tetramers. Zoom-in shows two main contacts for contacting pair of linker residues 278-288 (top circle) and a pair of contacting loop residues 130-140 (bottom circle). (c) glutaminase domain rotation of crystal structure relative to cryo-EM filament structures. (d) representative density from crystal structure. (d) density for nucleotides presumed to be ATP and UTP. (f) Relative orientations of nucleotides relative to cryo-EM structures. ATP and UTP are from Substrate-bound Ura8 filament. Crystal structure nucleotides are in purple, presumed to be ATP and UTP in their respective sites.

2.3. Yeast CTPS filaments reduce enzyme activity

To test whether CTPS filament assembly has a direct effect on enzyme activity, we generated mutations at H360 in the assembly interface of Ura7 that either disrupted or stabilized filaments. First, we generated H360A, which disrupts polymerization of the human enzymes, and which our structural analysis suggests is the pH sensor in assembly of the yeast enzyme (Lynch et al., 2017; Lynch and Kollman, 2020). Consistent with those prior results, Ura7-H360A did not assemble filaments with substrates or products at low or high pH (**Figure 4.1a**). To mimic protonation at H360, we mutated it to arginine, with the expectation that a constitutive positive charge might support polymerization at neutral pH. Indeed, we found that Ura7-H360R robustly assembles filaments at pH 7.4 which, like the wild-type protein, assemble only in the presence of substrate or product ligands (**Figure 4.1a, Figure 4.2**). Recombinant wild-type and both mutant proteins had similar purity and yield (**Figure 4.3a**). To confirm that H360R does not alter filament structure, we determined a 6.7 Å cryo-EM structure of substrate-bound Ura7, which is indistinguishable from wild-type at this resolution (**Figure 4.3b–f, Figure 8.6**). Thus, reversible assembly of H360R into wiltype-like filaments is pH-insensitive.

Decoupling polymerization from pH in engineered mutations provides tools to determine the functional consequences of polymerization on enzyme activity. Yeast CTPS activity has a strong intrinsic pH-dependence that peaks around pH 8.0 (Nadkarni et al., 1995; Yang et al., 1994), likely due to pH sensitivity of the active site cysteine in the glutaminase domain (Trotta et al., 1973). Consistent with this, Ura7 wild-type, H360A, and H360R all have low activity at pH 6.0. However, H360A had approximately threefold higher activity, indicating that unassembled CTPS maintains residual activity even at low pH (**Figure 4.1b**). Wild-type CTPS and mutants retain activity at pH 7.4, where we measured the substrate kinetics of all three. The KM values were similar for wild-type and both mutants, indicating no change in affinity for the substrate UTP. However, Vmax varied inversely with the degree of filament assembly (**Figure 4.1c, Table 4**). At pH 7.4 Ura7-H360A is completely tetrameric and had the highest activity, wild-type enzyme has a background of single filaments and had slightly lower activity, and Ura7-H360R had robust filament assembly and the lowest observed activity. This suggests that filament assembly in itself acts as an allosteric inhibitor of enzyme activity, with kcat reduced likely as a consequence of the constricted ammonia channel we observe in the filament structure.

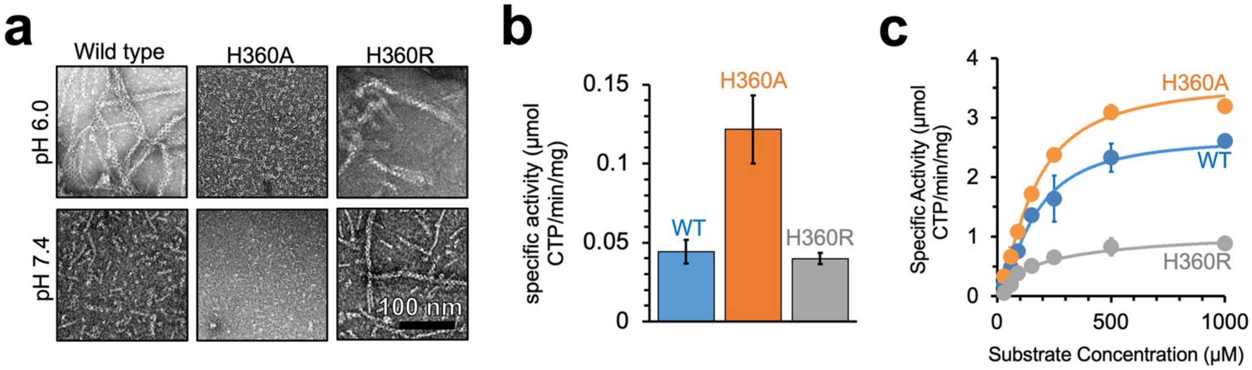

Figure 4.1: Yeast CTPS polymers reduce enzymatic activity. (a) Negative stain EM of purified wild type and mutant Ura7 with addition of 2 mM CTP. (b) Activity assay with saturating substrates of Ura7 and mutants at pH 6.0. (c) Substrate kinetics of wild type and mutant Ura7 at pH 7.4 with four parameter regression curve fits. Experiments done in triplicate, error bars are standard error of the mean (SEM).

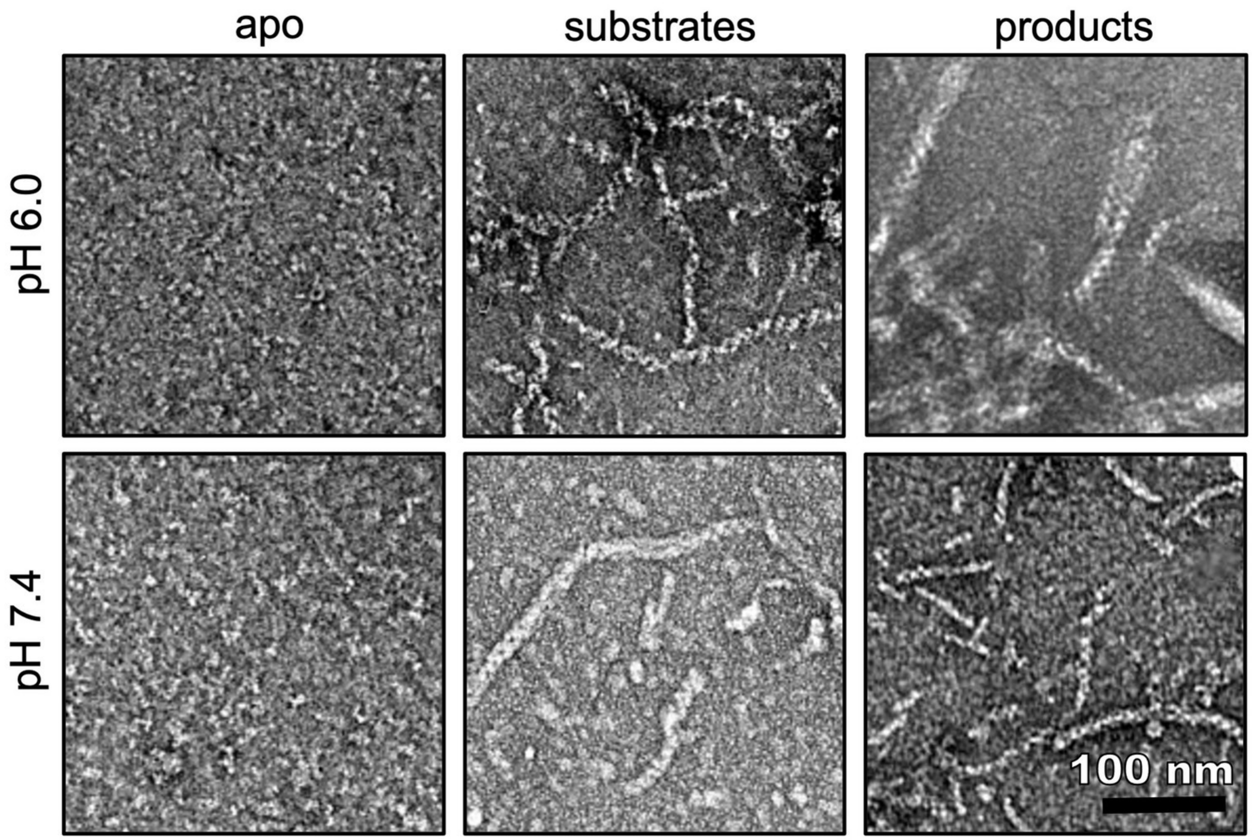

Figure 4.2: Ura7 H360R ligand-dependent assembly. Negative stain EM of Ura7 H360R assembly at low and high pH with addition of substrates (2 mM UTP/2 mM ATP) or product (2 mM CTP).

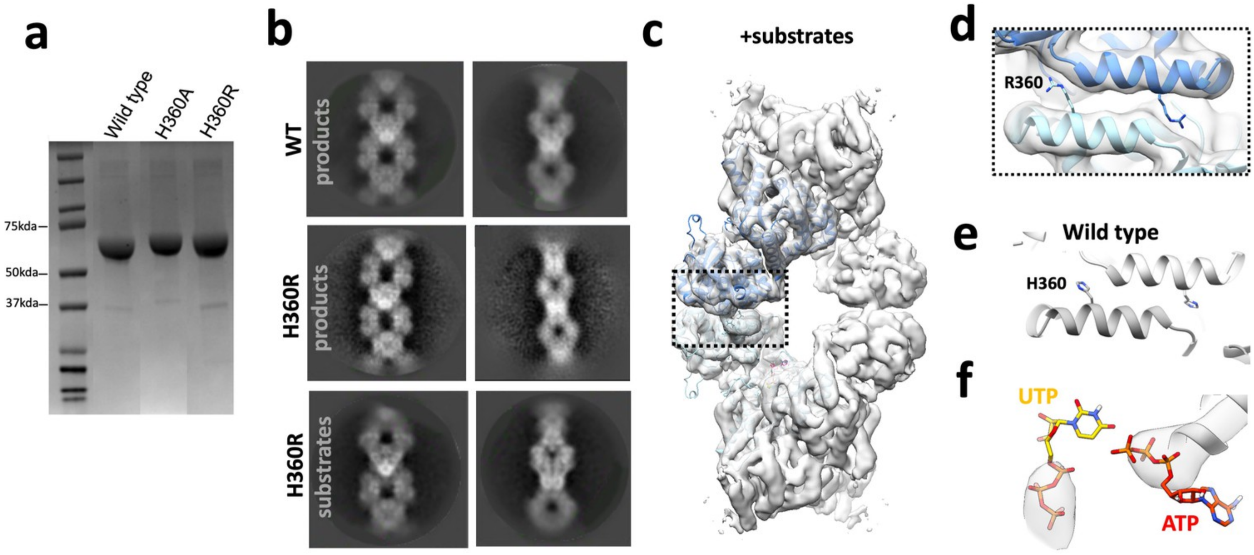

Figure 4.3: Ura7 H360R structural validation. (a) SDS-PAGE gel of wild type and mutants purified in tandem. (b) Representative 2D class averages of product-bound Ura7 wild type, and product or substrate-bound Ura7 H360R. (c) 3D reconstruction of substrate-bound Ura7 H360R with two monomers placed by rigid body fit of domains. (d) Zoom in from box in panel C of Ura7 H360R assembly interface with arginines modeled at residue 360. (e) Wild type Ura7 interface. (f) Nucleotide density from reconstruction in panel c.

2.4. CTPS assembly is critical for growth

To investigate the *in vivo* consequences of CTPS assembly, we generated yeast strains with filament assembly mutations at the endogenous locus, either with or without fluorescent protein tags, and tested both enzyme localization and cell growth (**Figure 5.1a**). We did not observe differences in growth between wild-type strains with and without fluorescent tags; nonetheless, the growth assays described below were all performed with untagged strains.

Based on our *in vitro* findings, we predicted that the pH-insensitive Ura7-H360R would constitutively assemble polymers in cells. But surprisingly, its localization was very similar to wild-type, diffuse during log phase growth and assembled into foci upon nutritional deprivation. However, Ura7-H360R-GFP assembly and disassembly kinetics are dysregulated (**Figure 5.1b–c, Figure 5.2**). Upon transition to starvation media, wild-type Ura7-GFP typically assembles foci over the course of 30 min, but Ura7-H360R-GFP assembles more rapidly, with virtually all cells having foci at 5 min. Even more striking, upon recovery from starvation, in which wild-type Ura7 disassembles in most cells after 30 min, at 1 hr we did not observe significant depolymerization of Ura7-H360R-GFP foci (**Figure 5.2**). The rapid assembly and slow disassembly of Ura7-H360R in cells are consistent with the *in vitro* pH-insensitive phenotype, but suggest that the starvation-triggered pH change is necessary but not sufficient to enable cellular Ura7 assembly. In addition to disrupted assembly kinetics, Ura7-H360R grew more slowly than wild-type, when plated either from log phase cultures or from starved cultures (**Figure 5.1d–e**), suggesting that disruption of normal Ura7 assembly and disassembly is generally detrimental to growth.

Consistent with our *in vitro* findings, cells expressing non-assembling Ura7-H360A-GFP or Ura8-H360A-GFP did not form foci, even under nutritional stress when the cytoplasm is acidified (**Figure 5.1a**). The non-assembly single mutants of Ura7 or Ura8 grew indistinguishably from wild type during log phase and upon recovery from starvation (**Figure 5.1d–e, Figure 5.3**). This suggested that polymerization of either CTPS isoform is sufficient to maintain normal growth. To test this, we generated the double mutant URA7-H360A/URA8-H360A, and found that it had a severe growth defect in log phase and upon starvation recovery (**Figure 5.1d–e**), indicating an important role for CTPS polymerization in proliferation. We wondered whether filaments might play a role in protecting CTPS from degradation, and that perhaps the growth defect in the double H360A mutants is due to loss of the enzyme during starvation (Petrovska et al., 2014). To test this, we starved Ura7-GFP, Ura7-H360A-GFP, and Ura7-H360R-GFP strains and measured the concentration of CTPS in total cell lysate. wild-type Ura7 levels are decreased during starvation, but there was no difference in protein levels between wild type and the mutants at 4 or 24 hr of starvation (**Figure 5.4**). This indicates that filament assembly does not play a significant role in protecting CTPS from degradation, and suggests that growth defects observed upon starvation recovery for URA7-H360A/URA8-H360A arise from other effects of defective polymerization.

It was surprising that strains with H360A or H360R mutations experienced slow growth relative to wild-type during log phase, when the mutant strains have the same diffuse localization seen in the wild-type strain. This may be consistent with the observation that wild-type enzymes have a low level of background assembly at neutral pH (**Figure 2.1c**), and indicates that small, transient assemblies may play a role in regulating activity during log phase growth.

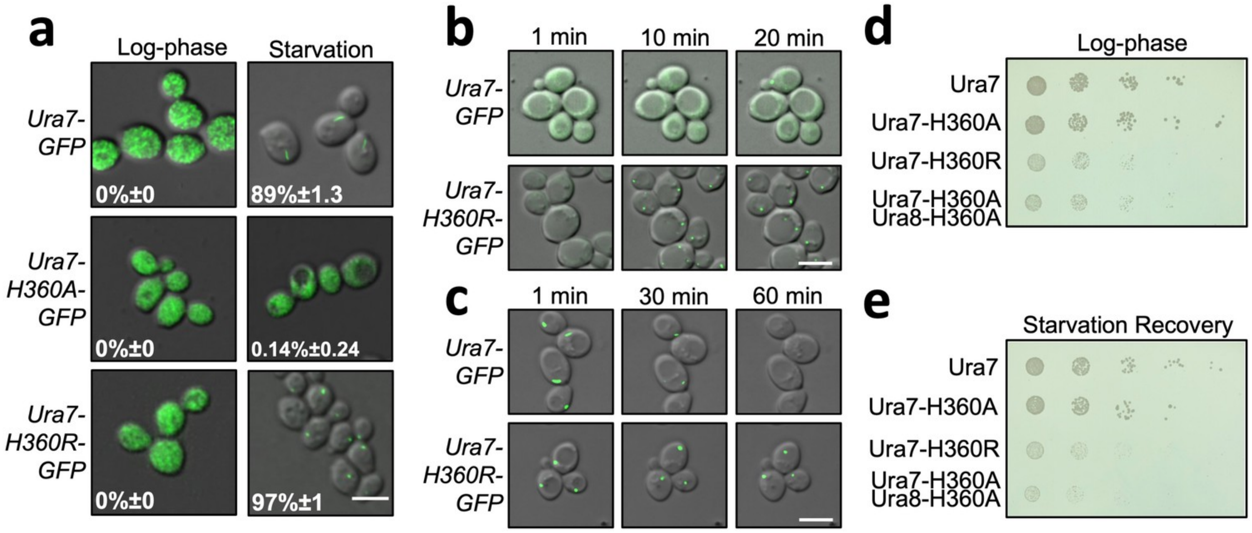

Figure 5.1: Dysregulated assembly of CTPS in yeast leads to slowed growth. (a) Yeast expressing GFP-tagged Ura7. Quantification is the percentage of cells showing foci. Scale bar is 5 µm. (b) Polymerization kinetics of GFP-tagged Ura7 in yeast upon transfer of cells to starvation media. (c) Same as B, for depolymerization kinetics upon re-addition of starved cells (4 hr) to nutrient-rich media. Scale bar is 5 µm. (d) Spot growth assay of yeast expressing wild type and mutant CTPS from liquid cultures grown in log phase. 1 in 10 dilutions increase from left to right. (e) Same as D, for yeast starved for 4 hr and allowed to recover on nutrient-rich solid media.

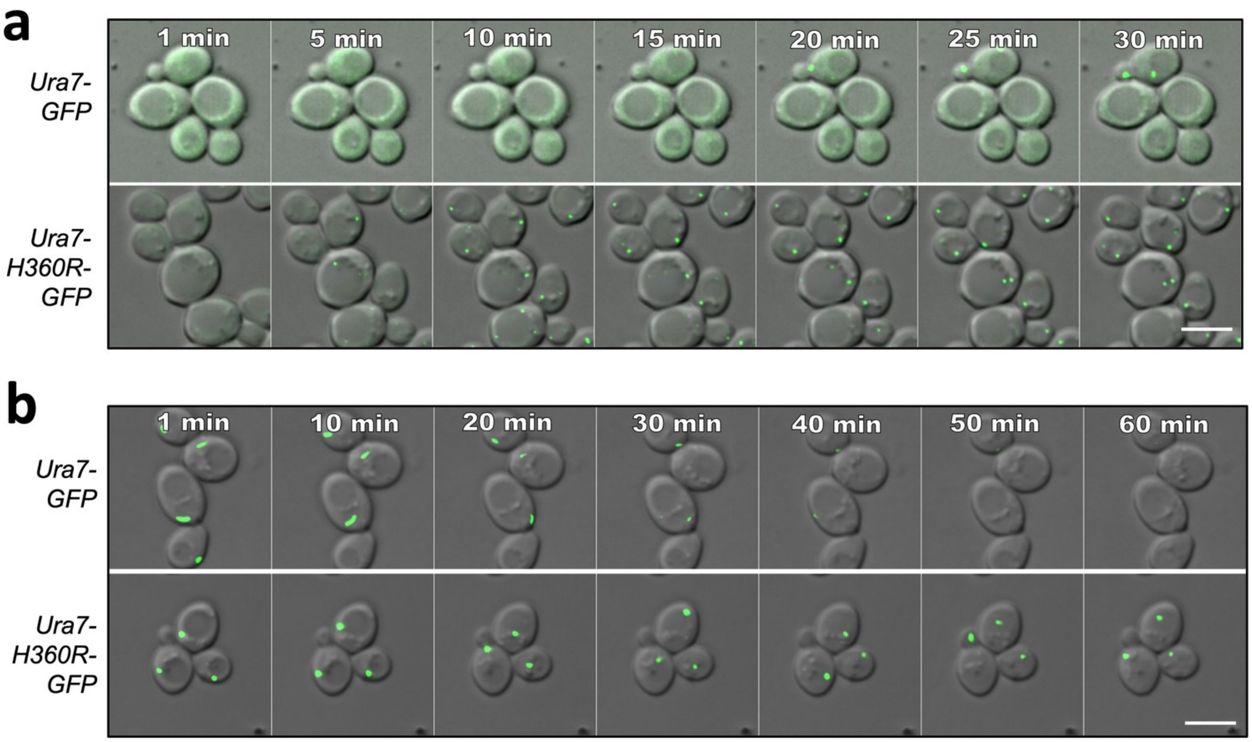

Figure 5.2: Ura7 assembly and disassembly kinetics. (a) Yeast expressing GFP-tagged Ura7 upon transfer from log-phase growth conditions to minimal starvation media (at time 0). Scale bar is 5 µm. (b) Yeast expressing GFP-tagged Ura7 after 4 hr starvation upon transfer to nutrient-rich media. Scale bar is 5 µm.

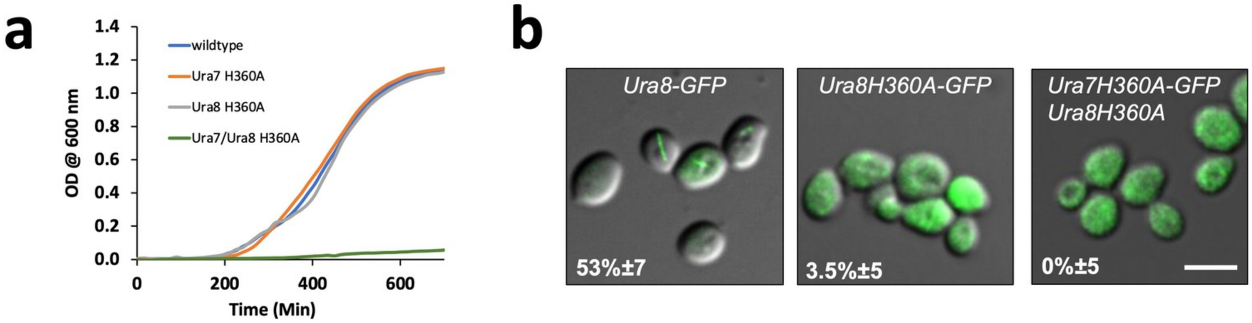

Figure 5.3: URA8 non-assembly mutant. (a) Liquid culture growth curve for wild type and mutant Ura7 and Ura8. (b) GFP-tagged Ura8 wild type and mutant after 4 hr of starvation. Scale bar is 5 µm.

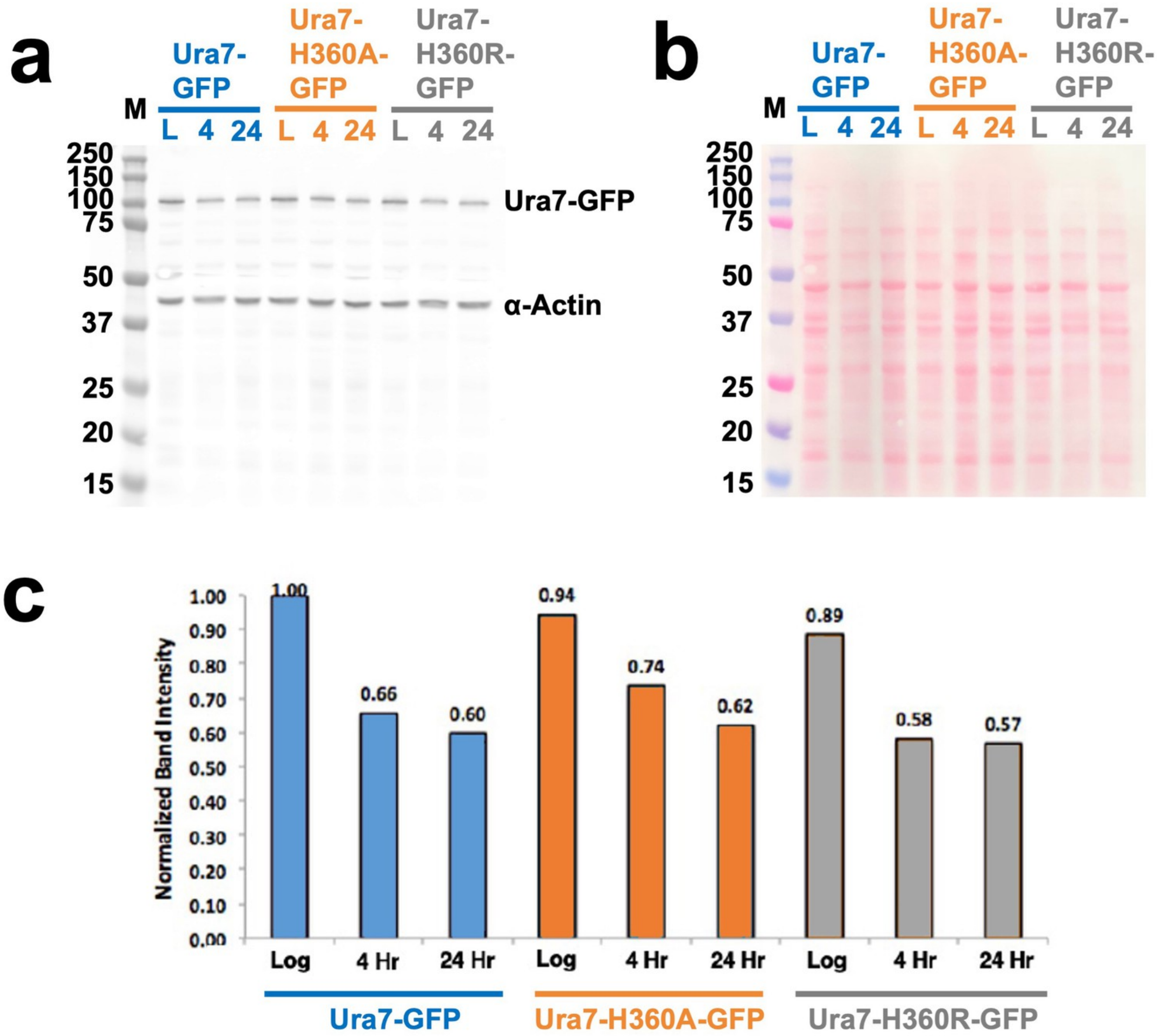

Figure 5.4: Ura7 quantification from yeast cell lysates. (a) GFP-Ura7 expressed in yeast and quantified by Western blot. Wells were normalized by OD600 of cells, and Ura7 levels were assessed by anti-GFP antibody with anti-actin control. Ura7 was assessed in log phase ("L"), and after 4 or 24 hr of starvation. Ladder, left, is in kilo-dalton. (b) Ponceau stain of western blot from panel a. (c) Quantification of band intensity from panel A, relative to the most intense band, are displayed above each bar.

2.5. Co-Assembly of yeast CTPS isoforms

Using our polymerization mutants of Ura7 and Ura8, both with fluorescent in vivo constructs and purified protein for in vitro analysis, we investigated the interplay between yeast isoforms. As has been reported previously, we observed very strong co-localization between GFP-tagged Ura7 and mCherry-tagged Ura8 in yeast upon nutrient deprivation (**Figure 6.1a**). However, we also unexpectedly observed that when we introduced non-polymerizing Ura7 into cells with fluorescently tagged wild-type URA8 there was a marked reduction in Ura8 foci (**Figure 6.1a**). Similarly, non-assembling Ura8 introduced into Ura7 wild type cells reduced foci of the latter (not shown). This suggested to us that Ura7 and Ura8 are capable of influencing polymers of one another.

To pursue this further, we assembled purified wild-type Ura7 *in vitro* while doping in increasing amounts of purified non-assembling Ura8, and the inverse experiment with swapping isofrms (**Figure 6.1b**). Total protein concentration was maintained constant. In both cases, increasing non-polymerizing mutant reduced the total number of polymers observed by negative stain (**Figure 6.1b**). While this may be due to such complications as differences in protein sticking to our EM grid, it is consistent with our *in vivo* findings and with the hypothesis of co-assembly. Lastly, by mapping sequence variations onto the surfaces of both isoforms it can be seen that the tetramerization interface is almost completely conserved between the two isoforms (**Figure 6.1c**). Taken together these findings raise the possibility that Ura7 and Ura8 co-assemble at the tetramer level both *in vitro* and *in vivo*. ((comment about Fig 6.1d)).

The possibility that yeast CTPS isoforms co-assemble at the tetramer level suggests a model where modulating expression between isoforms may add another level of fine-tuning CTPS activity. During log-phase growth, Ura7 likely exists in an equilibrium of unassembled tetramers and short filaments, which we have shown dampens activity (**Figure 4.1c**). Conversely, based on our *in vitro* results we expect Ura8 to be entirely unassembled during log-phase growth. Therefore through varying expression of isoforms, yeast may be able to fine tune the extent to which CTPS is polymerized and consequently to modulate it's activity (**Figure 6.1d**). Further, the reported differences in ligand responsiveness and optimal pH activity between isoforms (Nadkarni et al., 1995; Yang et al., 1994) can be adjusted. Varying expression between isoforms may therefore fine tune enzymatic turnover through combining isoforms.

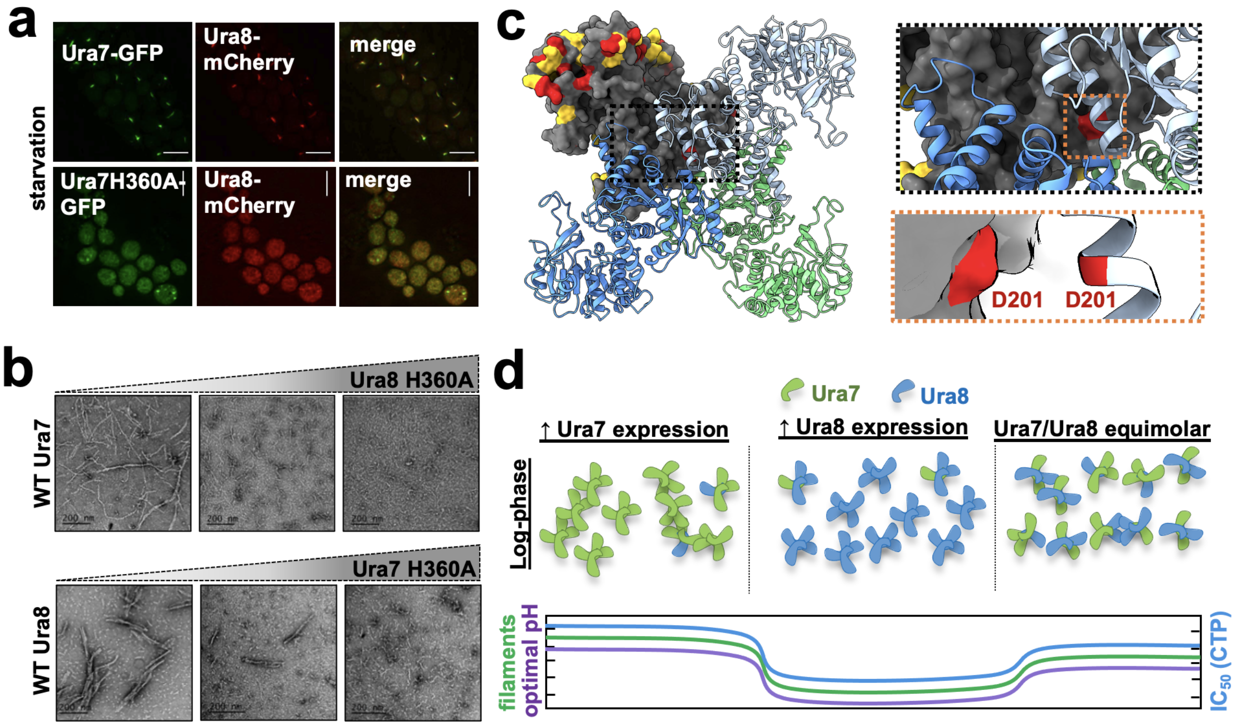

Figure 6.1: Co-assembly of yeast CTPS isoforms (a) *In vivo* imaging of yeast expressing fluorescent tagged CTPS isoforms during starvation. Top row is wild type protein. Bottom row is with non-polymerizing Ura7, which shows that wild type Ura8 is also disrupted in this strain. (b) Negative stain EM of purified wild-type CTPS mixed with increasing concentration of the non-polymerizing mutant of the other isoform. (c) Model of Ura8 with residue differences between isoforms mapped onto the surface (yellow = similar, red = different). The single different residue in the tetramerization domain is D201, shown in the inset on the right side. (d) Possible model for consequences resulting from isoform tetramer co-assembly. During log-phase growth, high Ura7 expression leads to short filaments and dampened activity. High Ura8 expression would lead to entirely unassembled protein, while equimolar expression would produce a mixture of short filaments and unassembled protein. Differences in optimal activity pH and IC_{50} for CTP have been reported between isoforms, which could be tuned according to expression levels of each isoform (bottom).

2.6. Yeast CTPS assembles large-scale ordered bundles

In wild-type cells at 30 min after nutrient deprivation, cells that had CTPS foci almost all had just a single structure (**Figure 2.1b**), consistent with prior reports of CTPS polymerization in yeast (Noree et al., 2010; Petrovska et al., 2014; Shen et al., 2016). However, during the live cell imaging experiments described above, in cells expressing wild-type Ura7-GFP we frequently observed the appearance of multiple small puncta at early time points that later coalesced into a single large structure (**Figure 7.1a**). This *in vivo* behavior is reminiscent of the rapid linear polymerization followed by lateral aggregation into larger bundles that we observed *in vitro* (**Figure 2.5**).

We determined structures of CTPS filament bundles formed at pH 6.0 to better understand the mechanisms of lateral assembly. Our initial question was whether the bundles were aggregating non-specifically, or whether there were defined assembly contacts. Reference-free two-dimensional averages of bundle segments from cryo-EM images of Ura7 and Ura8 were strikingly regular, suggesting ordered assembly contacts. This high degree of order allowed us to determine three-dimensional structures of both homologs in the presence of substrates or product using a single particle reconstruction approach by focused refinement of interacting pairs of filaments (**Figure 7.1b, Figure 7.2**). As we found for the single filament structures, Ura8 reconstructions went to higher resolution (3.3 Å for substrates and 3.7 Å for product) than Ura7 (6.6 Å substrate and 7.0 Å product). The individual filaments that pack laterally in the bundles closely resemble the corresponding single filament structures (**Figure 7.3, Table 2**). We observed two different bundle architectures. Ura7 formed very similar bundles in both ligand conditions, with adjacent filaments staggered relative to each other with a half-tetramer offset (**Figure 7.1c**). The Ura8 substrate-bound structure had the same architecture as both Ura7 bundles, but the product-bound Ura8 structure had very different interfaces between filaments, giving rise to filaments in register (**Figure 7.1d**).

To better understand the nature of lateral assembly contacts, we built atomic models into the two Ura8 bundle structures. Ligands were clearly visible, and bound as in the single filament structures, and the longitudinal assembly interfaces were the same as observed in the single filaments (**Figure 7.3**). Domain rotations and the state of the closed ammonia channel were nearly identical between filaments and bundles (**Figure 7.4**). Unlike single Ura8 filaments determined at an intermediate pH (6.5) and with two rotamers for His360, the bundle map appeared to fit a single rotamer which points to D370 (**Figure 3.4d–e**). Lateral associations between filaments result in tightly packed bundles. The buried surface area per tetramer at lateral interfaces, 2202 Å^2 (substrates-bound) or 1676 Å^2 (product-bound), is comparable to the 2460 Å^2 involved in longitudinal filament assembly contacts, suggesting that lateral association contributes to the overall stability of the assembly (**Figure 7.5, Table 5**). Yeast CTPS has a 7-residue insert (residues 273–279) in the linker region that mediates the bulk of the lateral interaction in both bundle types (**Figure 7.1e**). In the substrate-bound structure, Leu277 nestles into a hydrophobic pocket formed by Ile383/Ile387/Ile412/Phe429 (**Figure 7.1f, Figure 7.6a,b**). In the product-bound structure the linker inserts near the tetramerization interface and packs against Pro236 and Ile225 (**Figure 7.6c–d**). Although at lower resolution, the Ura7 structures appear to make the same lateral contacts as substrate-bound Ura8 (**Figure 7.2**). Similar filament bundles have not been reported for other species, despite extensive structural characterization of human, Drosophila, and E. coli CTPS filaments (Barry et al., 2014; Lynch et al., 2017; Lynch and Kollman, 2020; Zhou et al., 2021), suggesting that the unique yeast insert promotes lateral assemblies that are specific to yeast.

There are overall differences in the types of contacts mediating Ura7 versus Ura8 bundles. Ura7 bundle contacts are largely charged interactions, while Ura8 bundles appear to be held together with hydrophobic interactions (**Figure 7.9**). This is consistent with our observation that salt appears to drive apart Ura7 bundles but drives together Ura8 bundles (**Figure 2.4**). In an effort to generate non-bundling mutants, we mutated residues at the suspected lateral interaction sites (**Figure 7.9**). Ura7 mutations had no effect on filament assembly or association into bundles at pH 6.0. This suggests either our suspected lateral assembly residues were incorrect or that more mutations are required to break apart bundles. Conversely, Ura8 mutants assembled neither filaments nor bundles, perhaps a result of a lower tolerance of Ura8 contacts towards mutagenesis, for example if bundle interactions contribute towards holding together longitudinal filament contacts. There is a known Ura7 activity-activating phosphorylation site (S354) (Park et al., 2003) very nearby a the bundle contact. We therefore wondered whether phosphomimetic mutants at this site would impact bundling. We hypothesized that phosphorylation may repel and weaken bundle strands, increasing the likelihood of filament disassembly and resulting in increased activity. However, our phosphomimetic mutants showed no difference in capacity for bundling (**Figure 7.10**).

Given the proximity of the C-termini in lateral bundle contacts we wondered whether we could generate a non-bundling mutant by C-terminal truncation. Further, C-termini are involved in mediating filament assembly in human protein (Lynch and Kollman, 2020), leading us to wonder whether such a mutant might also prevent filament assembly. For C-terminal models for Ura7 and Ura8 extend to residue 572 and 571, respectively, due to weak density in our cryo-EM maps. Nonetheless, the positioning of C-termini differs between isoforms: Ura7 C-ter making close contacts with its monomer while Ura8 extends outward laterally in an alpha helix (**Figure 3.3e**). We generated C-terminal truncations for Ura7 (Δ560-576) and Ura8 (Δ562-578) and observed that Ura7 assembled as normal but Ura8 assembled neither filaments nor bundles at pH 6.0 with any ligand (**Figure 7.11**). This was surprising since neither C-termini appear close to the filament assembly interface, but the outward facing direction of the Ura8 C-ter residues may hint that they are more likely to be involved in lateral assembly or longitudinal filament contacts.

Although individual filament-to-filament lateral interactions within a given condition are all identical, there is variability of the assembly architecture at longer scales. The dihedral symmetry of the CTPS tetramer presents two potential lateral interfaces on each face of single filaments, but steric constraints limit occupancy to just a single lateral interaction per face. 3D classification of bundles yielded multiple structures with 3–5 associated filaments, with mixtures of cis or trans configurations of laterally associated filaments accounting for the variation (**Figure 9.8**). To envision potential larger bundle architectures, we extrapolated the lateral contacts by propagating assemblies *in silico* (**Figure 7.7**). In both cases, clashing dictates specific geometries which the bundles may take on (**Figure 7.8**). For the staggered bundle architecture, propagation of cis or trans interactions results in curved sheets. Propagation of trans interactions in the Ura8 product bound structure with filaments in register also results in a curved sheet, but propagation of cis interactions results in a closed tube with nine filaments. Mixed cis and trans interactions are also possible and observed in some of our 3-D classes, and give rise to increasingly complex structures.

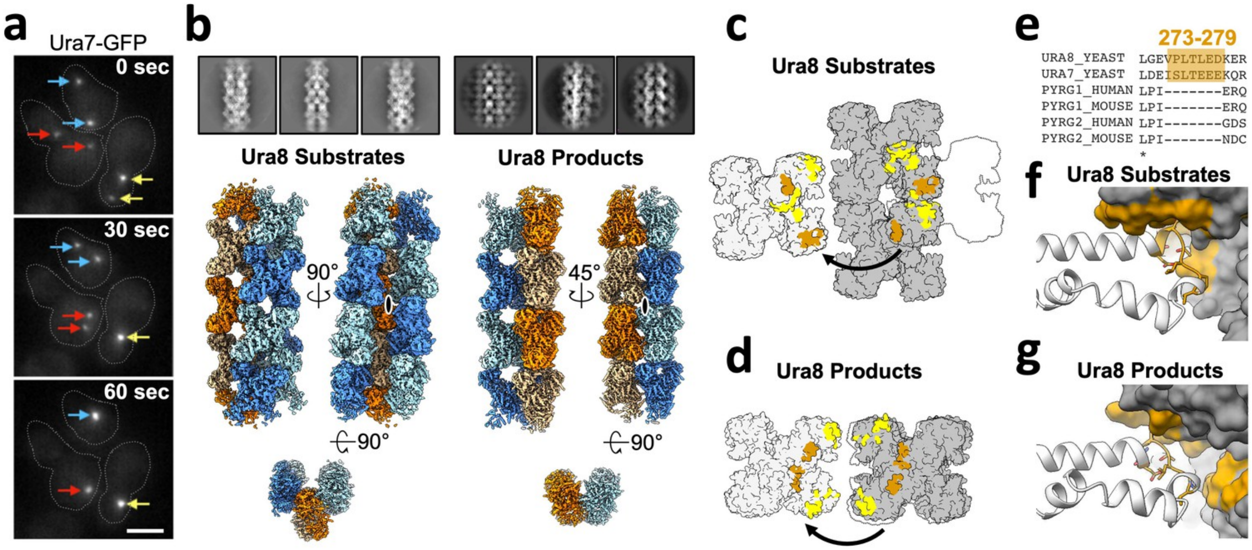

Figure 7.1: Yeast CTPS assembles highly ordered and distinct bundle architectures. (a) Live imaging in yeast expressing GFP-tagged Ura7. Same colored arrows indicate pairs of foci that join to larger foci at later time points. Time indicated is seconds after imaging began. Cell outlines drawn manually. Scale bar 5 µm. (b) Cryo-EM 2D averages and 3D reconstructions of Ura8 in the substrate (2 mM UTP/ATP) and product-bound (2 mM CTP) states. Individual strands colored in either orange or blue with protomers shaded differently. C2 symmetry axes are shown as ovals, with axis of rotation projecting toward the reader. (c) Lateral interactions in the substrate-bound Ura8 bundle. Full contacts are painted yellow for a single tetramer (gray on left), including redundant interactions. The yeast-specific linker insert and the interface with which it interacts are painted brown. (d) Same as C, for product-bound Ura8 bundle. (e) Sequence alignment of the CTPS linker region showing the yeast-specific insert at the specified yeast residues. (f) Zoom-in of the yeast linker insert of the substrate-bound bundles interacting with the adjacent strand. Numbering is the same as panel C. (g) Same as panel F, for product-bound bundle. Numbering is the same as panel D.

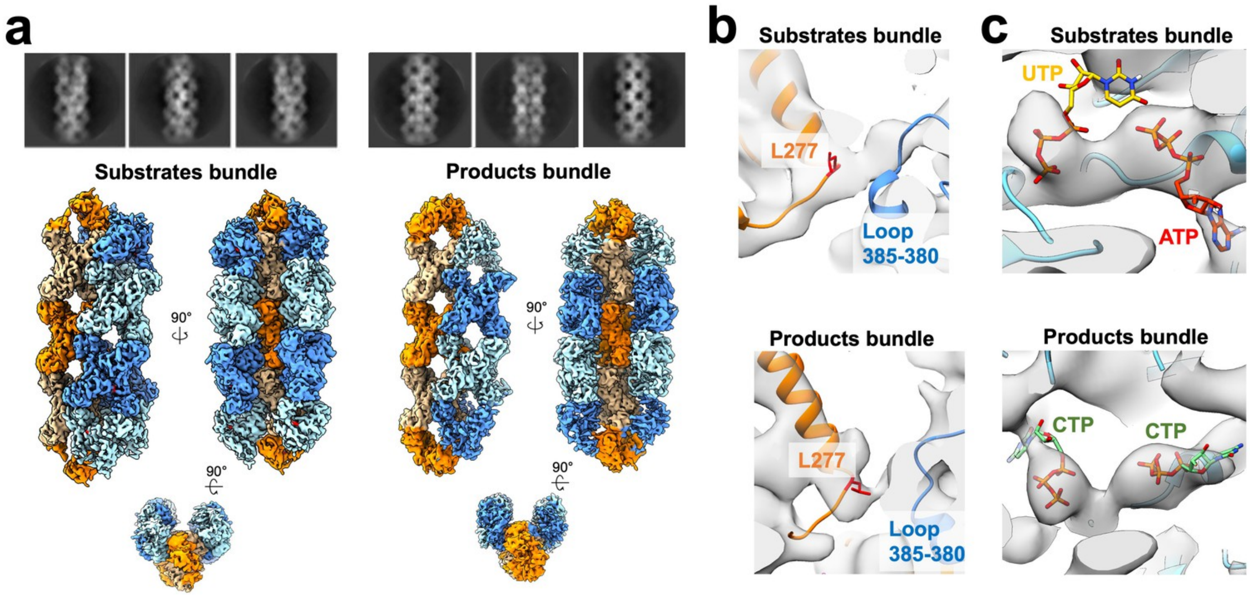

Figure 7.2: Ura7 bundle architecture. (a) Ura7 substrate- (2 mM UTP/2 mM ATP) and product- (2 mM CTP) bound cryo-EM 2D averages and 3D reconstructions. (b) Lateral contact mediated by yeast linker region (orange) with adjacent strand. Residue 277 is highlighted in red (see text). (c) Nucleotides in the active site with corresponding density.

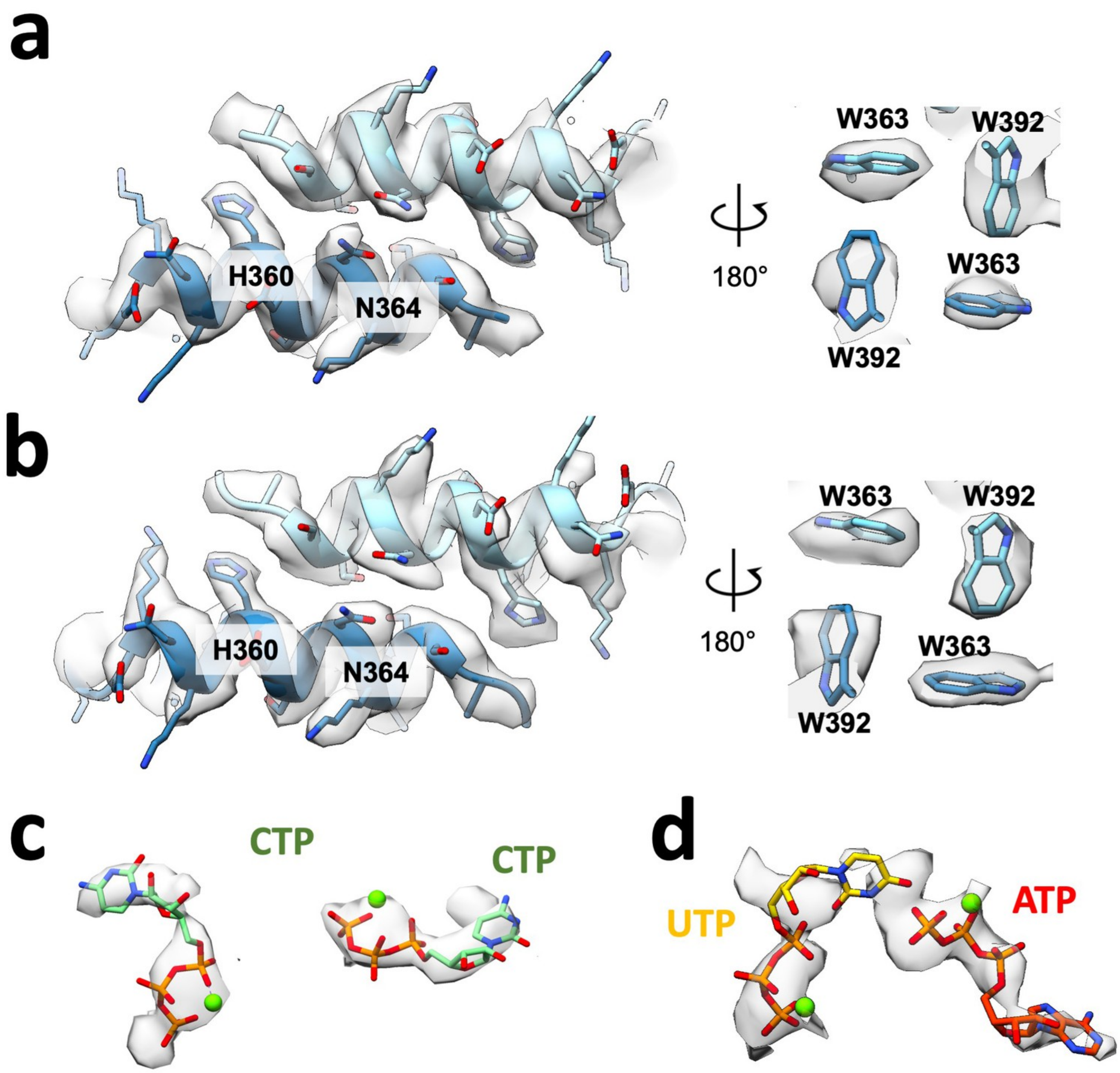

Figure 7.3: Filament assembly interface and nucleotides for Ura8 in bundles. (a) Assembly interface and corresponding density for an individual product-bound Ura8 strand while in a bundle. Key residues are indicated. (b) Assembly interface as in A, except for substrate-bound Ura8 bundle. (c–d) Nucleotides and corresponding density for substrate (c; 2 mM UTP/2 mM ATP) and product-bound (d; 2 mM CTP) bundle reconstructions.

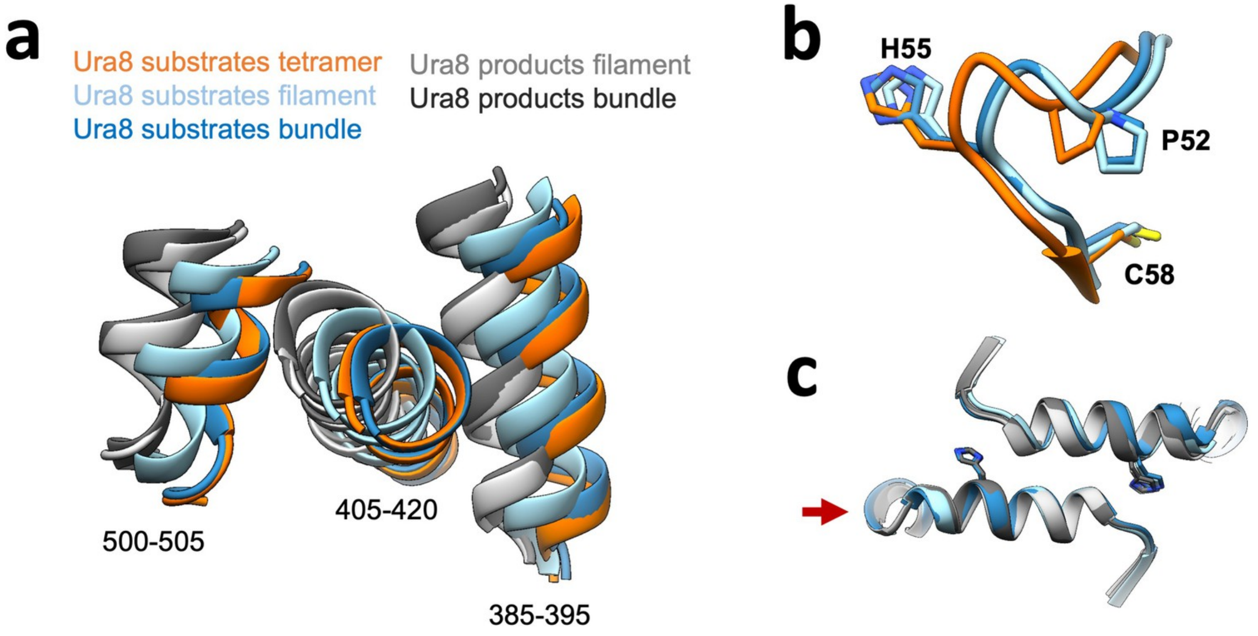

Figure 7.4: Comparison of filaments from individual filaments versus strands within bundles. (a) Glutaminase domain rotation of helices shown in Figure 4.1 (numbered here). (b) Ammonia channel key residues for closure for substrate-bound Ura8 bundle relative to tetramer and filament state. (c) Filament assembly interface for Ura8 either in bundles or individual filaments. Red arrow shows which side of the interface models were aligned on.

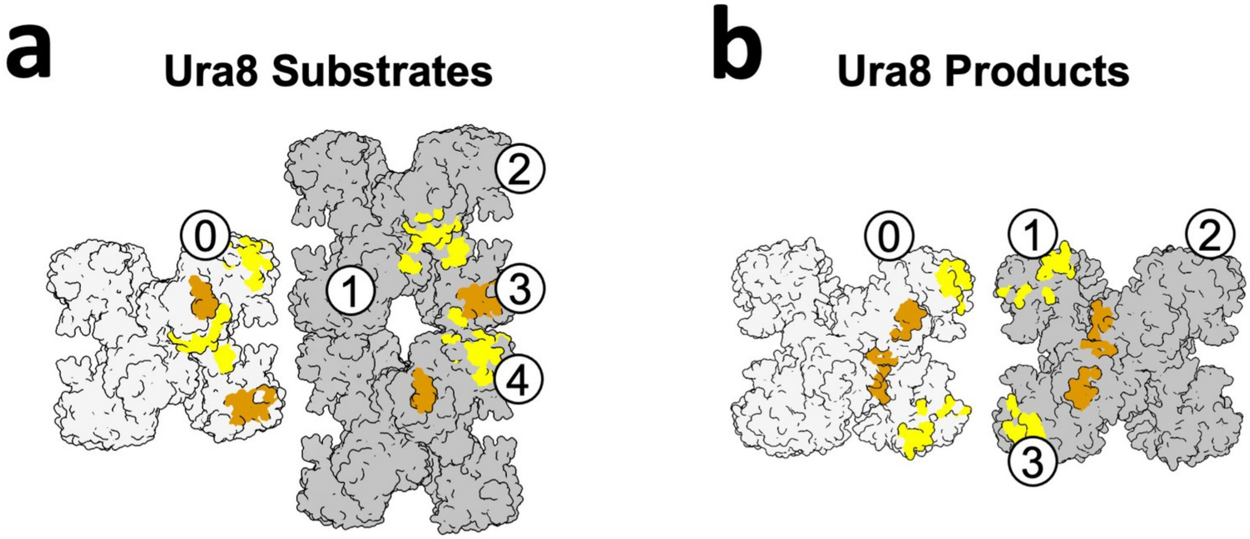

Figure 7.5: Numbering of monomers for assigning lateral contacts. (a) Substrate-bound Ura8 bundles showing two strands (light and dark gray) and the lateral contacts they make. Painted orange are contacts made by the yeast linker, and yellow are all others. Numbering scheme is for Table 4, which shows all contacts made for a single monomer (‘0’) to monomers on the adjacent strand (‘1–4’). (b) Same as A, for product-bound Ura8 bundles.

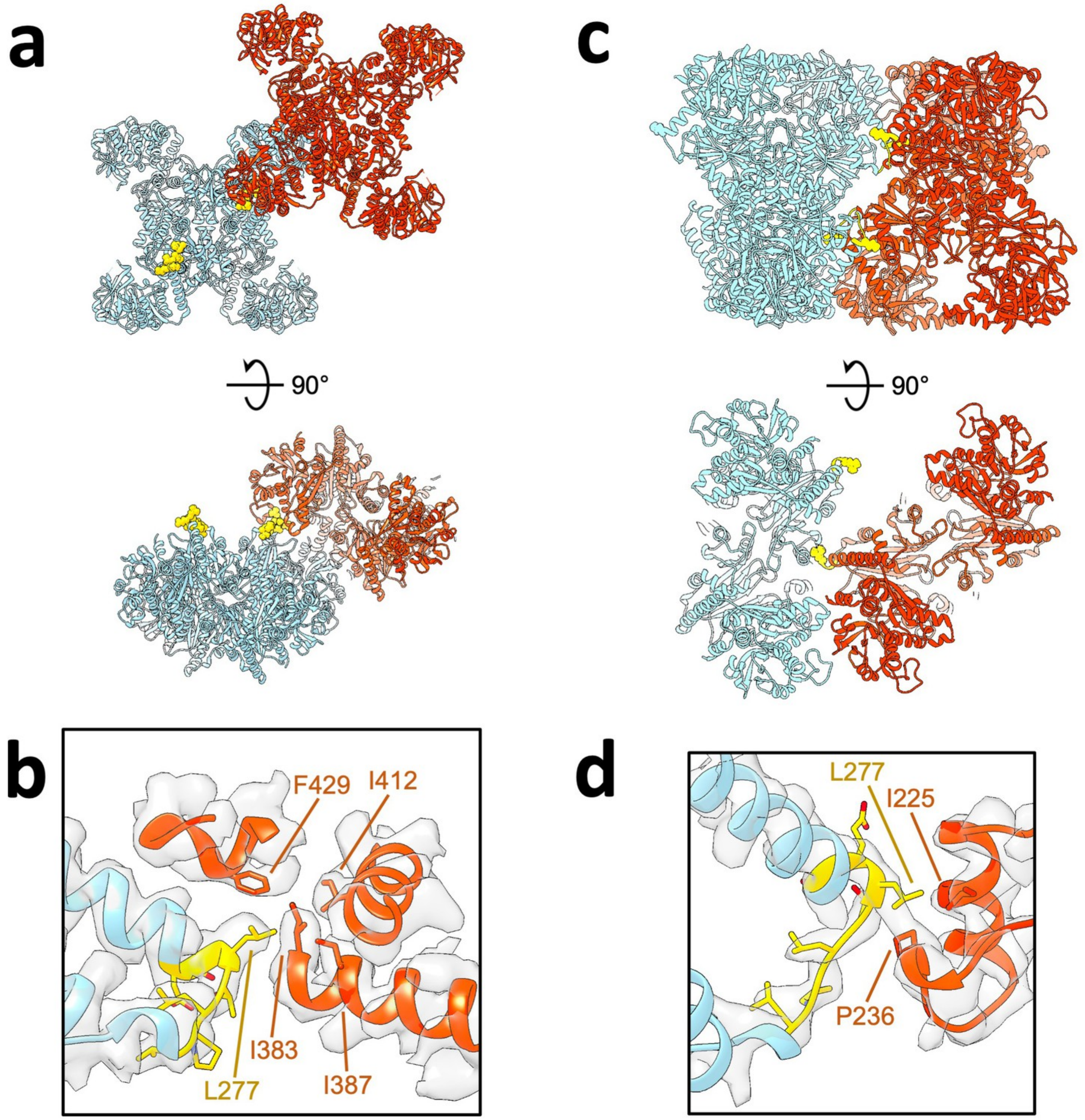

Figure 7.6: Yeast linker involvement in lateral bundle contacts. (a) Substrate-bound Ura8 bundle, shown are a pair of tetramers interacting laterally. Colored in yellow is the yeast linker insert (residues 273–279). (b) Zoom in of yeast linker insert contact with corresponding cryo-EM density. Yeast Insert residues putative contacts on the opposing strand are displayed. (c–d) Same as a-b but for a pair of tetramers in the product-bound Ura8 bundle.

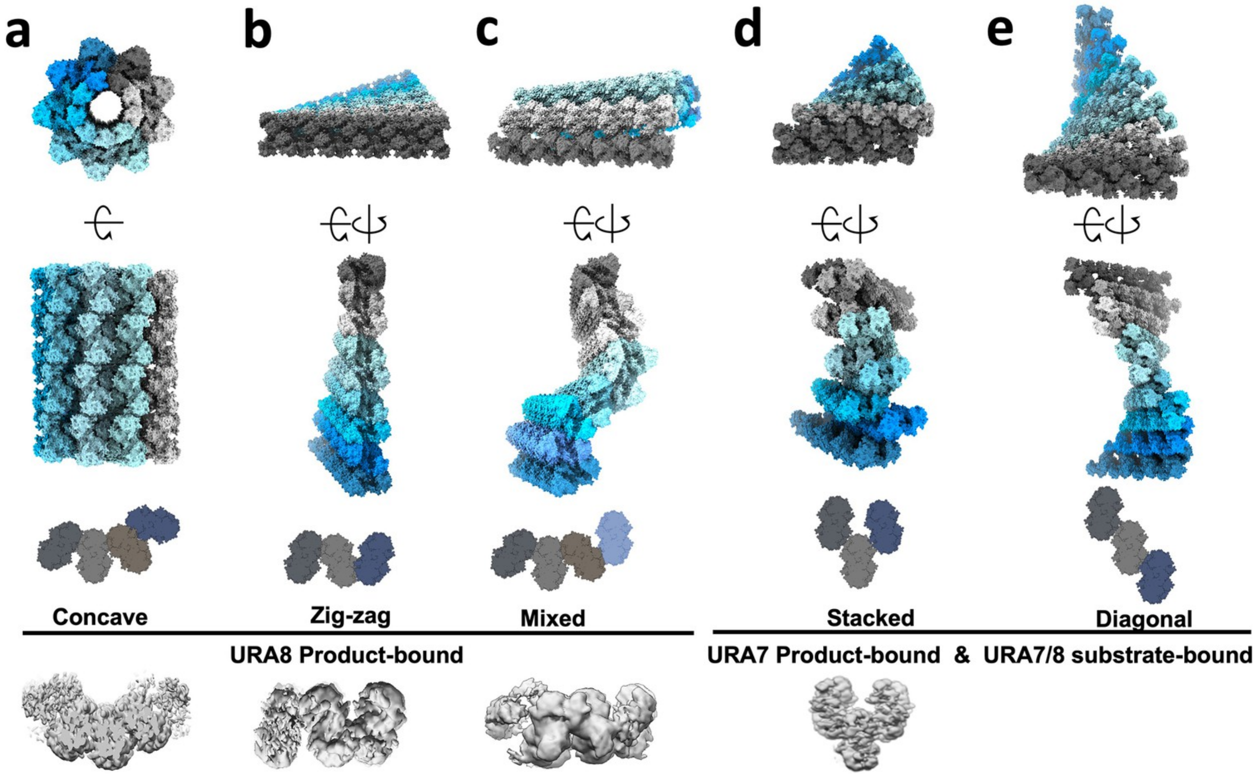

Figure 7.7: Possible higher order arrangements of yeast CTPS bundles. Models of possible bundle configurations generated in silico by propagating contacts. Bottom shows end-on views of 3D classification maps done in C1 which were used as templates to generate the propagated models above. (a–c) Configurations for product-bound Ura8 which has strands in register. (d)(–e) Configurations for staggered strand architecture adopted by Ura8 substrate-bound and Ura7 in both ligand states. No 3D map was obtained for a diagonal configuration but our modeling predicts that it should be possible without clashing.

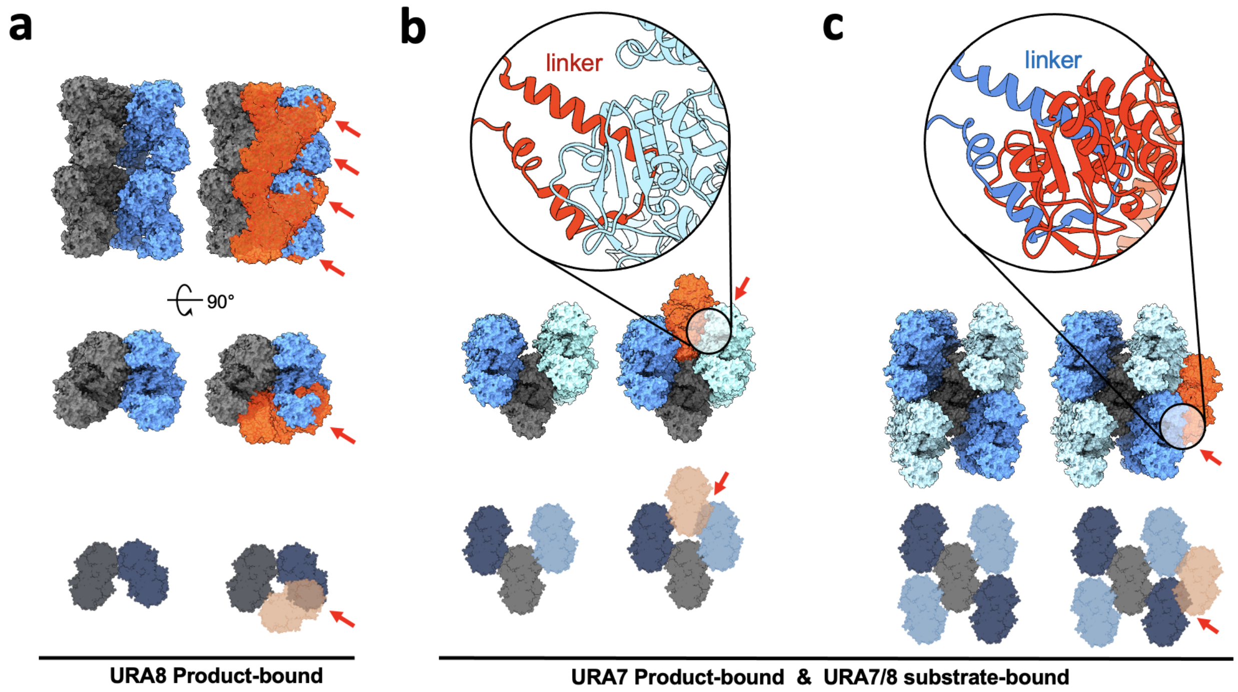

Figure 7.8: Clashing of bundle strands directs specific bundle architecture. (a) Ura8 product-bound bundle can only assemble with one adjacent strand on each face (blue and black). Attempted modeling of another strand (orange) creates strong clashing regions, indicating that such a bundle arrangement is improbable. (b) Bundles with strands staggered can accommodate alternating filaments in a zig-zag pattern, but modeling of a strand wedging between strands (orange) shows that clashing would occur, indicating such an arrangement is improbable. (c) Bundles with staggered strands can assemble with as many as two strands on each face for a total of 5 strands in a bundle. However, this geometry cannot be propagated due to a clash which occurs when neighbor strand is modeled in (orange).

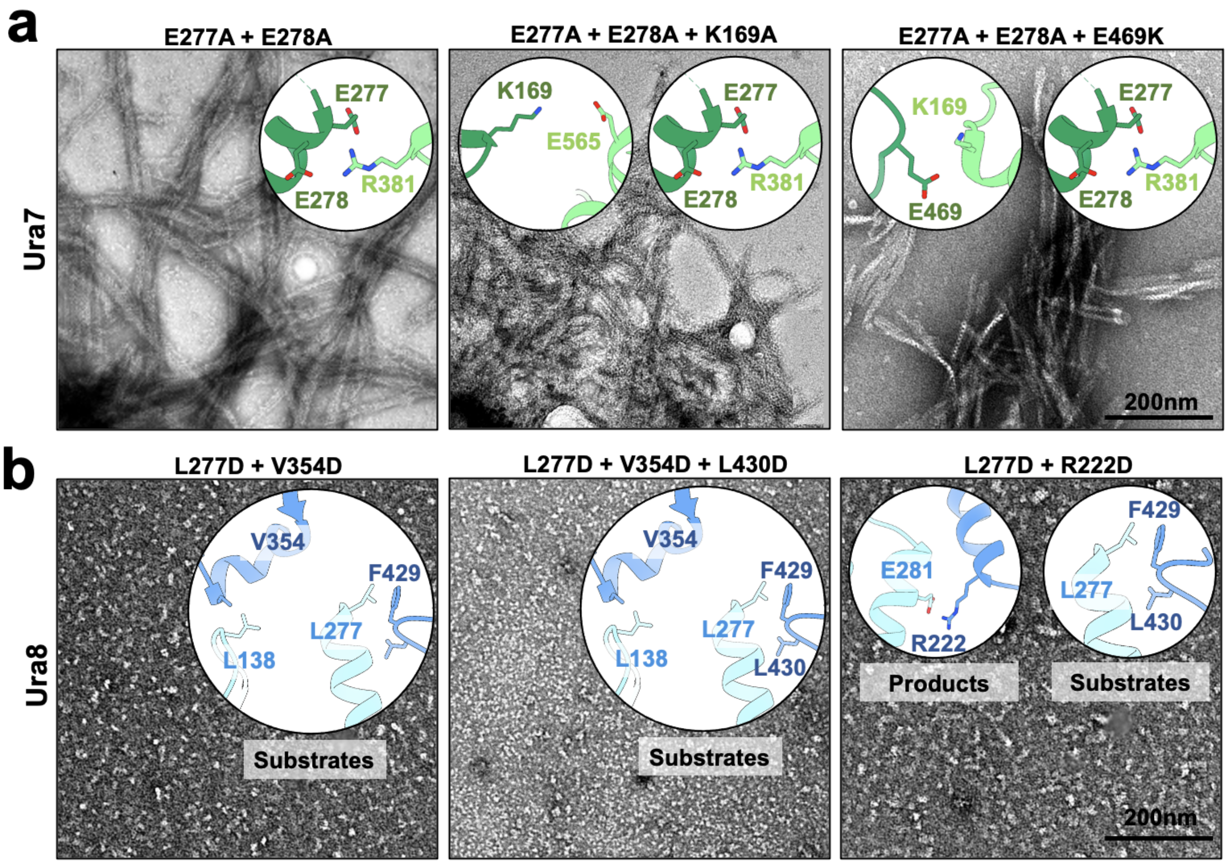

Figure 7.9: Non-bundling mutagenesis attempts. (a) Negative stain EM of purified Ura7 mutant protein which still assembles filaments and bundles. Insets show rationale for predicted contacts of lateral interactions (lateral strands shaded in different greens). (b) Same as panel a, but for Ura8 mutants. All mutants did not assemble filaments as assessed by negative stain EM. Lateral strands are shaded in different blue. Substrates/Products refers to whether the displayed contacts are for their respective type of bundle, i.e. staggered or in-register, respectively.

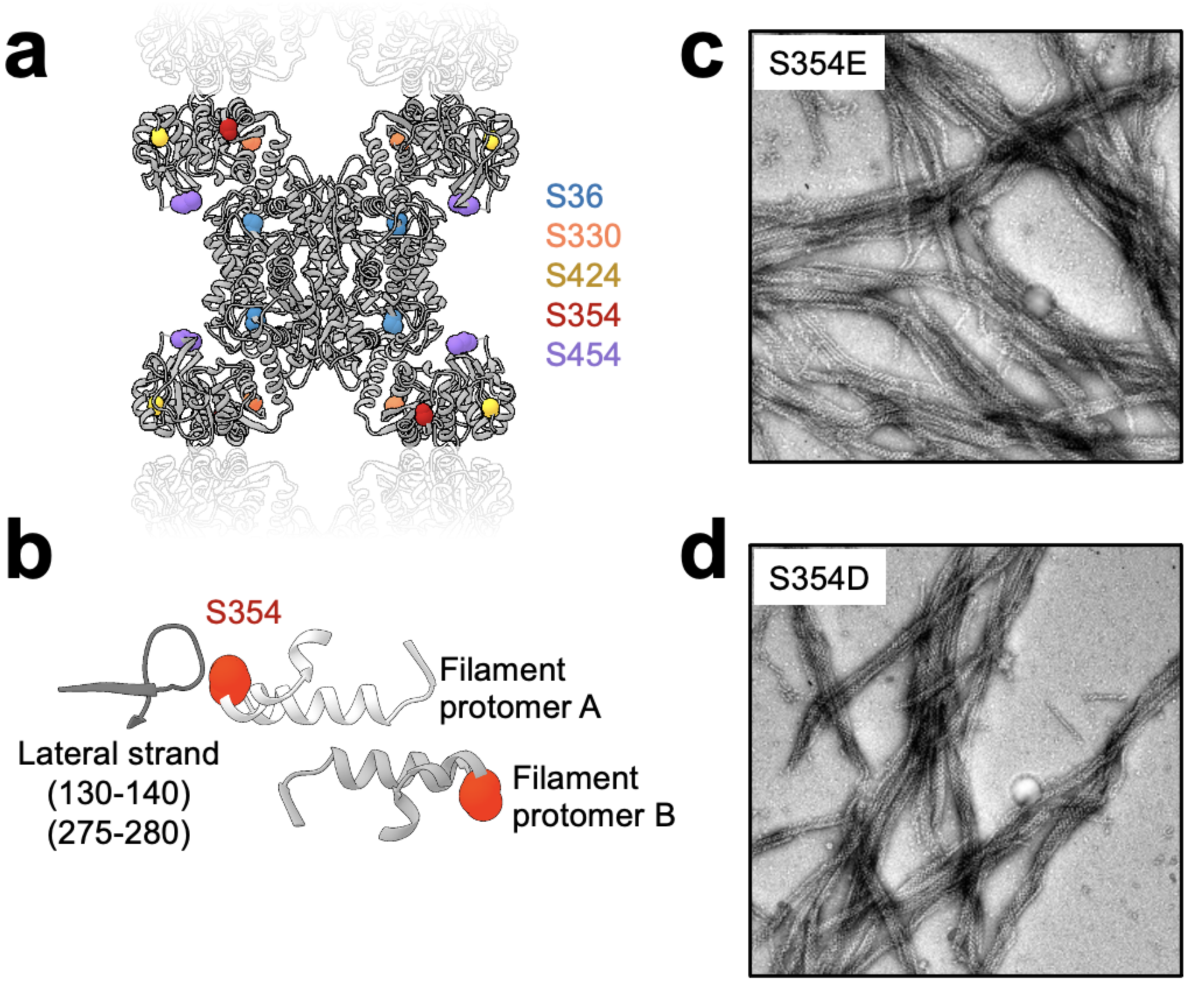

Figure 7.10: Phosphomimetic Ura7 Mutants. (a) Previously published phosphorylation sites (Choi et al., 2003; Park et al., 2003) mapped onto our Ura7 model. (b) filament assembly interface (white and light gray) showing placement of the activity-activating phosphorylation site S354. This site is also in close proximity to a lateral Ura7 bundle contact (dark gray, with possible interacting loops indicated below). (c-d) Negative stain EM of purified Ura7 phoshomitettic mutants which formed filaments and bundles similar to wild type protein at pH 6.0 with ligand.

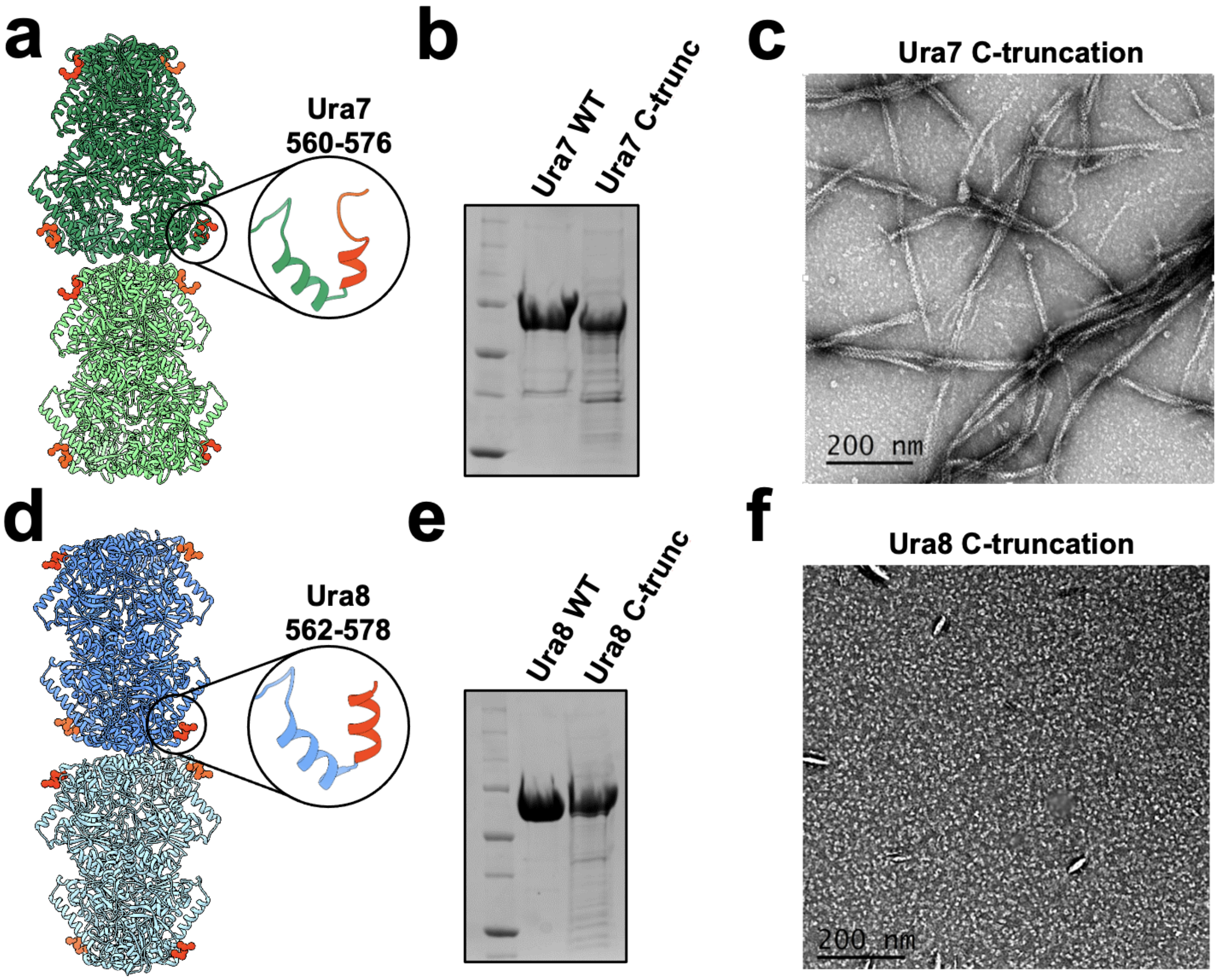

Figure 7.11: C-terminal truncations of yeast CTPS (a) Ura7 model built from cryo-EM filament map with C-ter residues highlighted in red. Only residues which could be built into density are displayed, however full C-terminus truncation residues are indicated above the inset. (b) SDS-PAGE gel showing purified wild type and mutant proteins. (c) Negative stain EM of purified mutant with addition of products at pH 6.0. (d-f) same as a-c but for Ura8 C-terminus truncation mutant.

Chapter 3: Discussion and Future Directions

3.1. Discussion and Future Directions

Maintenance of balanced nucleotide pools is essential for all organisms, and CTPS plays a critical, conserved role in directly balancing pyrimidine levels. The polymerization of CTPS into cellular filamentous polymers occurs in bacteria, archaea, and in eukaryotes (Carcamo et al., 2011; Ingerson-Mahar et al., 2010; Liu, 2010; Noree et al., 2010; Zhou et al., 2021). Bacterial and animal CTPS filaments assemble with completely different interfaces and functional consequences for enzyme regulation, inhibiting activity in the bacterial enzymes and increasing activity or enhancing cooperative regulation in the animal enzymes (Barry et al., 2014; Lynch et al., 2017; Lynch and Kollman, 2020). We have shown that budding yeast CTPS assembles filaments with yet another, distinct assembly interface that maintains the enzyme in a low activity state. The diversity of CTPS filament structure and function raises the question of whether this reflects modification of an ancestral filament structure, or whether CTPS polymerization has evolved independently multiple times. There is certainly precedent for extreme divergence in the quaternary structure of filamentous polymers, a striking example being the family of actin homologs in bacteria which have maintained polymeric forms but vary in assembly contact surfaces, strand number, polarity, and handedness that give rise to functional variation (Egelman, 2003; Ozyamak et al., 2013). Independently evolved filaments, on the other hand, would be consistent with the observation that proteins with dihedral symmetry (like the CTPS tetramer) can be induced to polymerize with a very small number of mutations on their high symmetry surfaces (Garcia-Seisdedos et al., 2017). A sequence alignment of *S. cerevisiae* and *S. pombe* reveals that many of the filament assembly contacts are conserved between the two organisms, suggesting similar filaments may exist in that organism (Fig). It is intriguing that fluorescent CTPS foci have been observed to S. pombe under nutrient-rich conditions then disperse when in stationary phase, a trend opposite to *S. cerevisiae* (Zhang and Liu, 2019). Polymers may therefore promote activity in this case. Given the regulatory importance of CTPS in nucleotide homeostasis, polymerization may have evolved as a relatively straightforward way to introduce a new layer of allosteric regulation to meet different demands in different lineages. Future studies of CTPS from more diverse species will likely provide greater insight into the evolution of its polymerization.

Whatever its evolutionary origins, the yeast CTPS filament has acquired features that make its assembly responsive to cytoplasmic changes in nutrient availability and growth conditions. Upon starvation-induced cytoplasmic acidification, CTPS assembly is dramatically increased in cells (Noree et al., 2019; Petrovska et al., 2014; Shen et al., 2016). We have shown here that yeast CTPS polymerization is a self-assembly mechanism that does not require other cellular factors, and that the pH-sensitivity of CTPS polymers is intrinsic to the enzyme itself (**Figure 2.1c**). The unique yeast CTPS assembly interface positions a titratable histidine residue, H360, to interact with an acidic residue, D370, an interaction that is likely strengthened at lower pH by H360 protonation (**Figure 3.4**). In the filament, CTPS is held in a conformation that closes off an internal ammonia channel that likely reduces activity (**Figure 3.1f and h**). Mutations at the assembly interface that either block assembly (H360A) or eliminate the pH sensitivity (H360R) showed that assembly is correlated with reduced activity, both at neutral pH where the wild-type enzyme forms short single polymers, and at low pH where the wild-type enzyme forms large laterally assembled bundles that are threefold less active than the non-assembling mutant (**Figure 4.1b**).

Lateral association of filaments into larger bundles has been observed in cells in various species by electron tomography, and suggested from fluorescence imaging (Carcamo et al., 2011; Ingerson-Mahar et al., 2010; Noree et al., 2019). Previous *in vitro* studies, however, showed purified CTPS forms primarily single filaments, and did not report extensive bundling, suggesting that the bundles observed in those cells may be induced by crowding (Barry et al., 2014; Lynch et al., 2017; Lynch and Kollman, 2020; Zhou et al., 2021). Yeast, on the other hand, has a strong propensity to assemble laterally that is intrinsic to the purified protein, driven by a yeast-specific insert in the linker domain that mediates well-ordered lateral contacts. Ura7 bundles in either ligand state are very similar, and at our resolution appear to maintain the same lateral contacts but with a slightly different helical twist. Regardless of nucleotide pools, bundles could therefore remain assembled to fulfill their role in the starvation response. Conversely, Ura8 forms bundles with radically different architectures dependent on whether substrates or products are bound; it remains unclear what the functional consequence is of having two distinct bundle architectures. Both types of bundles are able to accommodate lateral addition of strands in various ways, and this heterogeneity suggests that the specific architecture may be of less importance than simply maintaining protomers in a polymer.

The CTPS reaction mechanism is intrinsically sensitive to pH, with reduced activity at lower pH (Nadkarni et al., 1995; Yang et al., 1994). What then is the utility of having a redundant allosteric mechanism for inhibition by filament assembly at low pH? One possibility may be that the low residual activity of tetrameric CTPS at low pH is sufficient to imbalance nucleotide pools over prolonged starvation. Another explanation may lie in the kinetics of reactivation. Upon reintroduction of glucose the cytoplasm returns to neutral pH over about 2 min (Orij et al., 2009), but CTPS filaments disassemble over about 30 min or longer (**Figure 5.1c, Figure 5.2**), which may enable a more controlled ramping up of enzyme activity upon re-entering growth. In both our non-assembling and pH-insensitive mutants this process of controlled disassembly is disrupted, resulting in severe growth defects.

Our *in vitro* results correlating pH, filament assembly, and activity levels suggest a model for cellular function for CTPS filaments. Under growth conditions near neutral pH CTPS filaments modulate activity through an equilibrium of unassembled tetramers and dynamic short filaments that would be responsive to transient changes in substrate and product pools, as has been proposed for CTPS filaments of other species (Barry et al., 2014; Lynch et al., 2017). Sensitivity of CTPS polymers to the balance of substrates and products modulates transient spikes in UTP or CTP concentrations by driving assembly of inactive filaments or disassembly into active tetramers and loosely tethered flexible filaments (**Figure 8.2a**). Upon starvation, however, acidification acts as a signal to strongly drive assembly and inactivate the entire pool of CTPS in preparation for entering quiescence. Continued acidification drives filament growth as enzymatic activity ramps down, and eventually association of filaments into bundles (**Figure 8.2b center**) and lateral interactions maintain filaments in an assembled, low activity state. Upon nutrient re-addition and rapid re-alkalinization of cytoplasm, the size of bundles leads to a lag in depolymerization and a gradual ramp up of activity toward log-phase growth (**Figure 8.2b right**).

Disruption of polymerization-based allosteric regulation of CTPS likely results in disruption of nucleotide homeostasis, with potential consequences for processes that depend on nucleotide pools like ribosome biosynthesis, DNA replication, and phospholipid biosynthesis (Chang and Carman, 2008; Fairbanks et al., 1995). We predict that non-assembling mutants would overproduce CTP and deplete the substrate UTP, while pH-insensitive mutants would decrease CTP production, with cascading consequences for connected metabolic pathways. Further, disruption of CTPS increases genomic instability (Whelan et al., 1993), and specifically disrupting Ura7 in yeast is strongly mutagenic, particularly during the stress response (Schmidt et al., 2017). Our characterization of these mutants lays the groundwork for future studies to examine the role of CTPS assembly in maintaining global metabolite levels and flux in pyrimidine biosynthesis.

The assembly defective mutants had localization patterns in cells that were consistent with their *in vitro* phenotype (**Figure 5.1a**). Ura7-H360A-GFP did not form large-scale cellular assemblies under any growth conditions, confirming that the filament interface we observe in cryo-EM structures is important for assembly *in vivo*. Ura7-H360R-GFP, on the other hand, did not assemble large structures during log phase growth, as we would have predicted based on our observation of *in vitro* assembly at neutral pH (**Figure 5.1a**). One explanation may be that cytoplasmic concentrations of ligands, which are necessary for filament assembly in this mutant, are limiting under these normal growth conditions (**Figure 4.3**). Alternatively, in the cellular context some factor in addition to pH may prevent assembly during log phase growth, and once this block is lifted upon nutrient deprivation the Ura7-H360R-GFP polymer rapidly assembles even before the cytoplasm has acidified. Such a licensing mechanism might prevent small oscillations in nutrient availability from triggering massive CTPS assembly by transient pH changes, but only allow assembly under more pronounced stress. One candidate for such a licensing event could be phosphorylation or dephosphorylation of CTPS. Several functionally important phosphorylation sites have been identified in yeast CTPS (Choi et al., 2003; Park et al., 2003, 1999), one of which is near a bundle assembly contact (S354 in Ura7). However, there was a striking difference in *in vivo* assembly kinetics of Ura7-H360R-GFP which, unlike the wild-type enzyme, assembled much more rapidly than the approximately 30–60 min it takes for cytoplasmic acidification upon nutrient deprivation (Orij et al., 2009) (**Figure 5.1b, Figure 7.2**).

Our findings do not rule out other functions for CTPS filaments beyond a role in allosteric enzyme regulation. In particular, one possibility is that filament formation by multiple yeast enzymes during starvation changes physical properties of the cytoplasm to a more protective solid-like state (Petrovska et al., 2014). CTPS filaments likely do contribute to bulk cytoplasmic changes, but our observation that the disruption of only this filament is sufficient to drastically disrupt normal growth suggests that CTPS polymers play a more specific role in managing nutrient stress. CTPS filaments may also serve other functions in scaffolding or signaling; Ura7 co-localizes with other metabolic filaments in yeast (Noree et al., 2019, 2010), raising the possibility that filaments provide a mechanism for direct physical interaction of enzymes for coordinated regulation of different pathways. Alternatively, bundles may serve as a signaling mechanism of nutrient deprivation for interacting partner proteins. Previous studies have identified eif2 translation initiation factor interaction with CTPS filaments in Drosophila, which may have direct consequences on growth through organizing protein expression (Zhang et al., 2021). Future studies looking at the co-assembly state of these enzymes in the context of CTPS assembly mutants will be informative for determining whether CTPS bundles play an additional role in the stress response.

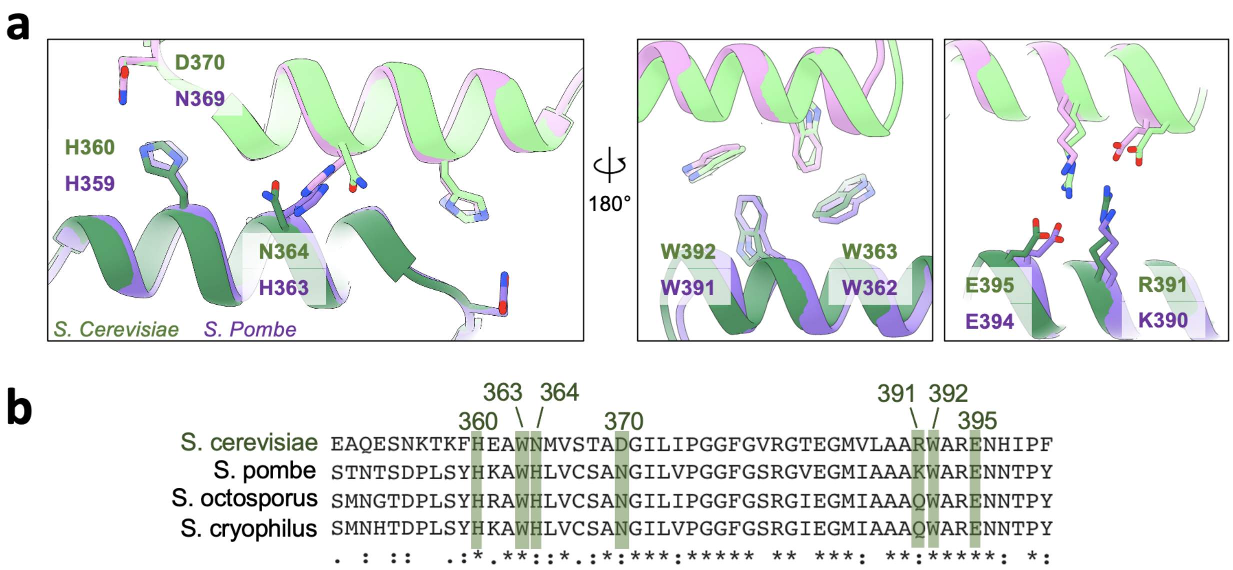

Figure 8.1: CTPS in *Saccharomyces pombe* (a) Alphafold 2 predicted structure of CTPS in *S. pombe* reveals a predicted filament assembly interface similar to *S. cerevisiae*. (b) Sequence alignment of important filament assembly interface for various species of yeast, with key assembly residues highlighted.

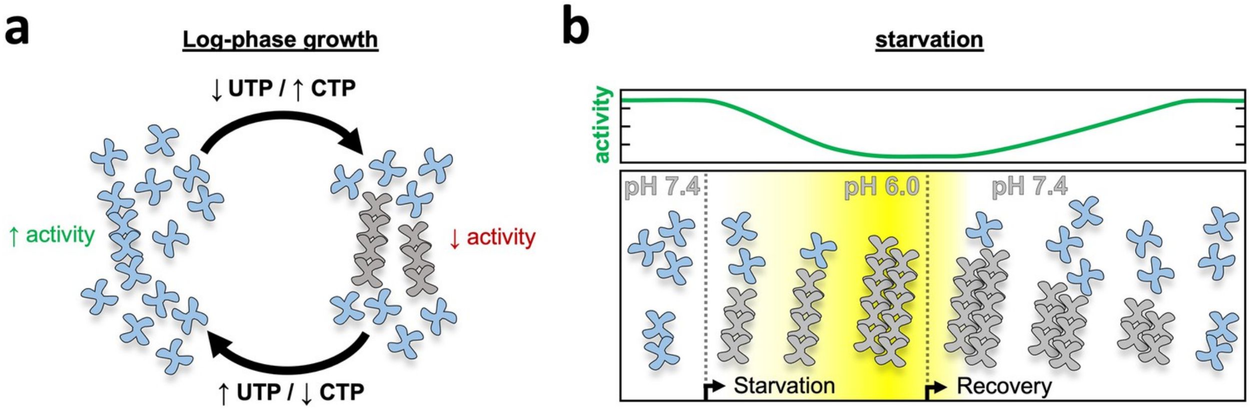

Figure 8.2: Model of yeast CTPS filament function. (a) Log-phase growth in yeast the majority of CTPS is in the unassembled active conformation, with a subset of enzyme polymerized to maintain nucleotide pool balance. If UTP levels are high, filaments are in the strained substrate-bound conformation which breaks assembly contacts, allowing the enzyme to remain active and process substrate while polymerized. When CTP levels are high, filaments assemble rigid product-bound filaments which inactivates the enzyme until equilibrium is reached and CTPS return to the substrate-bound filament state. (b) During log growth there is an equilibrium of CTPS tetramers and filaments (left). Starvation induces a slow cytoplasmic acidification which, in conjunction with a licensing event, leads to CTPS filament and bundle growth. Bundles maintain a low activity state by stabilizing filaments through lateral assembly. As yeast recover from starvation the cytoplasm is rapidly alkalinized, but bundles persist as they slowly disassemble and gradually ramp up activity toward log phase growth.

Chapter 4: Methods

4.1. Purification of recombinant CTPS and mutagenesis

URA7 and URA8 wild type genes with ribosomal binding site were cloned into pet28b-6His (Addgene, Massachusetts; Kan resistance, C-terminal 6 X his tags) at XhoI and XbaI sites. Mutants were generated by designing semi-overlapping primers following quickchange guidelines which incorporated the mutation (Liu and Naismith, 2008). Plasmids were transformed into E. coli BL21 (DE3) RIL cells for expression. Cultures were grown in Luria broth (LB) at 37 °C until reaching OD600 of 0.8, then temperature reduced to 18°C for induction with 1 mM IPTG overnight. The next morning, cultures were pelleted and either stored at –80°C or protein purification carried out immediately. All subsequent steps were carried out on ice or in a 4°C cold room. Pellets from 2 L of culture were resuspended in 40 mL ice cold lysis buffer (50 mM HEPES, 1 M NaCl, 20 mM Imidizole, 10 % glycerol, 1 mM PMSF, pH 7.8) and lysed with an Emulsiflex-05 homogenizer (Avestin, Ottawa, Canada) for approximately 5 min at 15,000 PSI. Lysate was then cleared by centrifugation at 33,764 g for 30 min at 4 °C in a Thermo Scientific Fiberlite F14−14 × 50 cy rotor. Clarified lysate was loaded onto a 5 ml HisTrap FF Crude column (GE, Massachusetts) on an ÄKTA start chromatography system (GE) pre-equilibrated with lysis buffer. Unbound material was washed away with 15 column volumes of lysis buffer before an isocratic elution with five column volumes of elution buffer (50 mM HEPES, 1 M NaCl, 250 mM Imidizole, 30 % glycerol, pH 7.8). Peak fractions were combined and concentrated approximately 3-fold using a 30 kDa cut-off Amicon centrifugal filter unit (Millipore, Massachusetts). Approximately 5 mL of concentrated protein was subjected to size-exclusion chromatography using the Äkta Pure system and a Superdex 200 increase 10/300 gl pre-equilibrated with running buffer (50 mM HEPES, 1 M NaCl, 10 % glycerol, pH 7.8). Peak fractions were collected and glycerol added to a final concentration of 30 % before again concentrating using a 30 kDa cut-off Amicon centrifugal filter unit. Protein at ~2 mg/ml was flash frozen in liquid nitrogen and stored at –80 °C. Recombinant human CTPS2 was purified as described in Lynch et al., 2020.

4.2. CTPS activity assays

To reduce variation between wild type and mutants (Ura7 WT, H360A and H360R), all three were purified in tandem and flash frozen. Aliquots were thawed, desalted into glycerol-free buffer (50 mM TrisHCl pH 7.4, 200 mM NaCl, 10 mM MgCl2), and concentrations measured at A280. Reactions were set up in 96 well clear plastic flat bottom corning plates (Corning, New York) with a 100 µl final reaction volume. For low pH kinetics, 2 µM protein was incubated with activity buffer (50 mM MES pH 6.0, 200 mM NaCl, 10 mM MgCl2, 10 mM BME) and nucleotide (2 mM ATP, 2 mM UTP, 0.2 mM GTP) for 15 min at 30 °C. Reaction was initiated by addition of 10 mM glutamine and absorbance measured at 291 nm in a plate reader (Varioskan lux) set at 30 °C. Early activity traces were noisy, likely due to bundled CTPS, so slope was measured between 350 and 500 s where rate of activity stabilized. A linear regression was fit to determine slope, which was used to determine CTP concentration. Replicates were performed in triplicate and averaged. Substrate kinetics were run under less optimal conditions in order to capture rates at lowest substrate concentrations. Ura7 at a final concentration of 1.5 µM was added to reaction buffer (50 mM TrisHCl 7.4, 200 mM NaCl, 10 mM MgCl2) and nucleotides (1 mM ATP, 20 µM GTP, with a range of 20µM to 1000 µM UTP). Mixture was incubated at room temperature for 5 min then inserted into a plate reader set to 22 °C and allowed to equilibrate for an additional 5–8 min, while taking readings at 291 nm until readouts were stable. The plate was briefly ejected from the reader to manually initiate the reaction by addition of glutamine (1 mM final concentration, prepared in 20 mM TrisHCl pH 7.0). CTP production was measured at 291 nm for 5 min, capturing the early linear phase of the curve. Assays were performed in triplicate then averaged, and kinetics data were fit by four parameter logistic regression y = min + ((min-max)/(1+((max/S50)n))), solving for maximum rate, minimum rate, S50, and hill number using the solver plugin in Microsoft Excel 16.51.

4.3. Right angle light scattering

Frozen CTPS was thawed and desalted into a glycerol-free buffer (200 mM NaCl, 20 mM HEPES 7.8). Sample was set up in a total volume of 120 µl for assembly at a final protein concentration of 2 µM with 1 mM CTP. Assembly buffer was 50 mM MES 6.0 or 50 mM TrisHCl 7.0–7.4, 500 mM NaCl, and 10 mM MgCl2. Protein was added to the buffer in a quartz cuvette and inserted into a Horiba Fluorolog three fluorometer (Horiba, Kyoto, Japan) set to 30 °C and allowed to incubate until signal stabilized (approximately 3–5 min). Assembly was initiated by addition of nucleotide then readings began immediately, usually with a 5-second lag between addition and commencing readings. A total of 350 nm excitation wavelength was used and emission spectra from 350 nm were collected with 0.65 nm slit width for both. Raw data was normalized by subtracting baseline signal from initial incubation step. Sample was run in triplicate for each condition, then averaged and plotted with standard deviation in microsoft excel 16.51. Curves in Figure 2.5 were fit using the four parameter logistic regression y = min + ((min-max)/(1+(max/S50)n)) solving for maximum rate, minimum rate, hill number, and S50. R2 values were determined using the built-in Pearson function tool in Microsoft Excel 16.51.

4.4 Negative stain electron microscopy

CTPS was assembled in reaction buffer (50 mM TrisHCl or MES, 100 mM NaCl, 10 mM MgCl2) at 30 °C for 15 min prior to applying 5 µl of sample to glow-discharged carbon-coated grids and incubated for 1 min at room temperature. Grids were washed 3 x in H2O followed by 3 x in 0.7 % uranyl formate with blotting in between all steps to remove excess liquid. Imaging was done on an FEI Morgagni electron microscope operating at an accelerating voltage of 100 kV. Datasets for hCTPS2 were collected on a Tecnai G2 Spirit (FEI) operating at 120 kV. Images were acquired at ×67,000 magnification (pixel size 1.6 Å/px) on a Ultrascan 4000 4k × 4k CCD camera (Gatan). Contrast transfer function (CTF) was estimated using CTFFIND4 (Rohou and

Grigorieff, 2015), Cryosparc v2.1 (Punjani et al., 2017) was used for automatic blob picking and 2D classification.

4.5. Cryo-electron microscopy sample preparation and data acquisition

Frozen URA7/URA8 was desalted into minimal buffer (5 mM MES 5.9, 50 mM NaCl) prior to assembly at 8 µM with either substrates (2 µM UTP, 2 µM ATP) or product (2 µM CTP). Reaction buffer contained 400 mM NaCl, 5 mM MgCl2, 3 mM DTT, and 50 mM MES either at pH 6.0 (predominantly bundles) or pH 6.5 (predominantly single filaments). Protein was assembled for 15 minutes at 30 °C then 3 µl of the reaction material was double blotted (Snijder et al., 2017) onto glow-discharged C-FLAT 2/2 holey-carbon grids (Protochips), allowing a 1 min room temperature incubation between sample depositions. Grids were subsequently blotted for 4.5 s using a Vitrobot MarkIV (ThermoFisher Scientific) with chamber conditions set to 100 % humidity and at 4 °C. For Ura7 H360R sample was assembled at 5 µM final concentration in 50 mM NaCl, 50 mM HEPES 7.5, and 10 mM MgCl2 then 3 µl deposited onto lacey carbon grids which had thin carbon floated on top. Data were acquired using an FEI Titan Krios transmission electron microscope operating at 300kV and equipped with a Bioquantum GIF energy filter (Gatan) set to zero-loss mode with a slit width of 20 eV. Movies were collected on a K2 Summit Direct Detector camera (Gatan) in super-resolution mode at a magnification of 130 K (pixel size 0.525 Å/px). Automatic data acquisition was done using the Leginon Software Package (Suloway et al., 2005) with a defocus range specified in Table 1. Movies were acquired containing 50 frames having an exposure rate of 8.9 e-/Å^2/s and a total dose of 89e-/Å^2. For product-bound URA8, which exhibited a severe preferred orientation, we collected data with a stage tilt of both 20 and 40 degrees and combined the data for processing.

4.6. Cryo-EM data processing

Assembly conditions for filaments also contained some bundles, and vice versa, therefore these datasets were combined early on and bundles/filaments were separated through 2D classification and processed independently afterwards. See supplemental methods for further details. Briefly, images were manually curated to remove poor quality acquisitions such as bad ice or large regions of carbon. Dose-weighting and image alignment of all 50 frames was carried out using MotionCor2 (Zheng et al., 2017) with binning by a factor of 2 (final pixel size 1.05 Å/px). Initial CTF parameters were estimated using GCTF (Zhang, 2016). Particle picking for bundles was done using the crYOLO (Wagner et al., 2019) helical pickier tool trained on both filaments and bundles and using a box size covering one tetramer, followed by manual picking to further improve the quality of the particle picks. I thank Thorsten Wagner, the author of crYOLO for troubleshooting this process with me. Helical picking was chosen for the ease at the particle picking step, despite not processing any of the data with helical refinement. For tilted data, we used the local GCTF per particle CTF estimation tool to improve per particle defocus values. To classify bundles from filaments, particles were extracted with a large box size (512 pixels). Particle stacks were exported to either cisTEM (Grant et al., 2018) or Cryosparc (Punjani et al.,

2017) for iterative 2D reference-free classification. Starting models for all maps were always obtained ab initio, and for bundle data the process was repeated in cisTEM and later cryosparc as independent validation. All four bundle starting models were obtained in this way, and no symmetry was imposed. 3D classification of bundles in C1 yielded subsets differing in their arrangement of strands. Classes sharing a common core assembly pattern were combined for further processing. In all cases, the highest resolution bundle maps were obtained by C2 refinement of a masked central segment after performing signal subtraction of density outside this region. Early processing without imposing symmetry suggested overall twofold symmetry in both bundle types. Therefore, we used a mask for focused alignment on three-strands (staggered bundle; Ura7 product- and substrate-bound & Ura8 substrate-bound) or two strands (in-register bundle; Ura8 product-bound) as these contained all the relevant contacts. FSC were calculated using Relion (Scheres, 2012) post-process or from the Phenix density modification (Terwilliger et al., 2020) output. Directional FSC was calculated using an online FSC calculator (https://3dfsc.salk.edu/).

4.7. Atomic model building and refinement

Initial models for Ura7 and Ura8 were obtained by threading their sequences onto the hCTPS1 substrate-bound structure from Lynch et al., 2017. Where inserts existed models were built in manually using Coot (Emsley and Cowtan, 2004). Models for individual monomers were rigid body fit using Chimera (Pettersen et al., 2004) by domain (0–280 amido-ligase domain; 281–300 linker; 301–570 glutaminase domain) then backbone and side-chain positions refined with ISOLDE (Croll, 2018). C-termini were built manually in coot using the best available Ura7 map (product-bound) and Ura8 map (substrate-bound). ATP was modeled using ISOLDE, and UTP/CTP using Coot after all ISOLDE refinements. Ligands for product-bound Ura8 were rigid body fit in coot. The density corresponding to Ura8 residues 417–457 was found to be weaker and have relatively lower resolution than the rest of the structure. To build this loop the RosettaES (Frenz et al., 2017) loop modeling protocol in Rosetta (Alford et al., 2017) was used with a beamwidth of 256. The top scoring result of the RosettaES protocol was selected and its geometries were refined with ISOLDE. Residues 444–455 were later removed due to poor angles and unsupported map density. After building the monomer, it was replicated at all symmetry equivalent positions to create the full tetramer, and a single monomer at the assembly interface. Residues at the tetramerization interface and assembly interface were relaxed using a full simulation in ISOLDE. Side chains and backbone angles were adjusted for a single monomer, which was again replicated to all four symmetry equivalent sites to generate the final tetramer model with identical subunits. Models were built into the high resolution product-bound Ura7 map, which was rigid body fit by domains (residues 0–273,276-299,302-C-ter) into lower resolution Ura7 product-bound bundle map based on local map quality. Junctions between domains were deleted (residues 274–275,300-301). For substrate-bound Ura7 filament, the Ura7-product-bound filament model was rigid body fit by domain and junctions deleted (domains 0–280,281-300,301-Cter; deleted 280–284 and 300–302). Clashes for this

Ura7-substrate-bound model were removed using ISOLDE. Substrate-bound Ura7 bundle was built from a rigid body fit of the substrate-bound Ura7 filament model as described above. Ura8 bundle model building began with models from their corresponding ligand-state filament, rigid body fit by domain, then refined in ISOLDE. This monomer was duplicated at all relevant contact sites and overall relaxed in ISOLDE to refine positions at tetramerization interface, filament assembly interface, and lateral bundle contacts simultaneously. The monomer was then replicated at all symmetry sites and because not each monomer experiences the same lateral contacts, it was docked into different spots and an ISOLDE simulation was run with only the residues at the lateral interface with restraints on everything else. The final monomer was duplicated into all sites to fill the map density and ligands docked in and refined using coot. Model statistics were assessed using molprobity online server (http://molprobity.biochem.duke.edu/) and the RCSB PDB Submission validation report. Buried surface area for lateral bundle contacts and filament interface were calculated using PDBePISA tool (https://www.ebi.ac.uk/msd-srv/prot_int/cgi-bin/piserver) with default parameters.

4.8. Substrate tunnel analysis

Caver 3.0.3 plugin (Chovancova et al., 2012) was used for Pymol 2.4.1 (Schrödinger, LLC, 2020) with default parameters. We set catalytic Cys404 as the start point for tunnel search of an individual monomer. Probe radius was set at 0.7 Å and the tunnel from Cys404 to the UTP base was identified. Inspection of radii along the length of the tunnel revealed that radii near the P52/C58/H55 constriction point in the Ura8 substrate-bound tetramer was between 1.2 Å and 1.9 Å, consistent with relieved ammonia channel constriction (Lynch and Kollman, 2020).

4.9. X-ray Crystallography

Ura7 was mutated to improve crystallization: loop deletion (residues 445-453), non-assembly (H360A), and C-terminal truncation (560-576). Ura7 protein was purified with an additional step of anion exchange chromatography using MonoQ column (GE) to improve purity. Protein was concentrated and drops set at 6mg/ml with nucleotides added (5mM MgCl2, 5mM UTP, 5mM ATP). Fallen whiskers from our cat Murphy were used to seed crystals, and for that we thank her dearly. Crystallization mother liquor was 100mM MOPS/HEPES-NA @ pH 7.3, 7% PEG8000, 14% ethylene glycol, 50mM "carboxylic acids mixture" (molecular dimensions), 2mM DTT. We note that the carboxylic acids mixture was not necessary to produce high quality crystals. Diffraction data were solved using molecular replacement with product-bound human CTPS1 model. First, a solution was searched using a tetramer of the amidoligase domains, then the glutaminase domain was searched. When we identified one glutaminase domain position we placed in copies at symmetry around the tetramer positions. Data was refined as rigid bodies with non-crystallographic restraints. Density modification was done due to the high solvent content (65%), which improved Rfree. Linker was built by hand and density modification repeated. Remaining regions of glutaminase domain were built by hand, nucleotides built, then refined a last time.

4.10. Yeast strain construction and media

Yeast were maintained in standard YPD (Lab Express) or synthetic media containing 2 % D-Glucose (Fisher). Background strains were W303 {leu2-3,112 trp1-1 can1-100 ura3-1 ade2-1 his3-11,15}. Deletion and mutation strains were made by a PCR approach as described previously (Wendland, 2003), and C-terminal tagging of yeast were made as described previously (Sheff and Thorn, 2004). List of yeast strains used can be found in Table 6.

4.11. Handling of yeast cells

To induce polymers, yeast were grown in YPD until mid-late log phase, washed in 1 X PBS and resuspended in starvation media- 0.1 M Phosphate-citrate buffer (pH 5,6,7) and grown shaking at 30 °C for 3–4 hrs. To manipulate intracellular pH in the presence of 2 % Glucose, 2 mM of 2,4-Dinitrophenol (Sigma) was added to the media as described previously (Petrovska et al., 2014).

4.12. Yeast growth assays

Liquid growth curves were made by diluting mid-late log phase and/or starved yeast cells to OD600 0.05 in YPD or SD +0.5 % Glucose and growth was monitored on a Varioskan Lux plate reader at 600 nm, shaking at 30 °C for 16 hr. Solid growth assays were done by making five 5-fold serial dilutions of mid-late log phase or staved yeast cells and plated on YPD or SD +0.25 % Glucose plates +2 % Agar and grown at 30 degrees for 48 hr.

4.13. Fluorescence microscopy

Fixed and live fluorescence microscopy was done at ×100 objective magnification on a DeltaVision Elite microscope (GE) equipped with DIC optics, using a 60 × 1.42 NA objective, and a sCMOS 5.4 PCle air-cooled camera (PCO-TECH). Deconvolution was performed with SoftWorx (API, Issaquah, WA) and images were analyzed using Fiji, ImageJ. Figures were assembled using Adobe Photoshop. Representative images shown of experiments done on three independent replicates. Fluorophores used were GFP and mCherry.

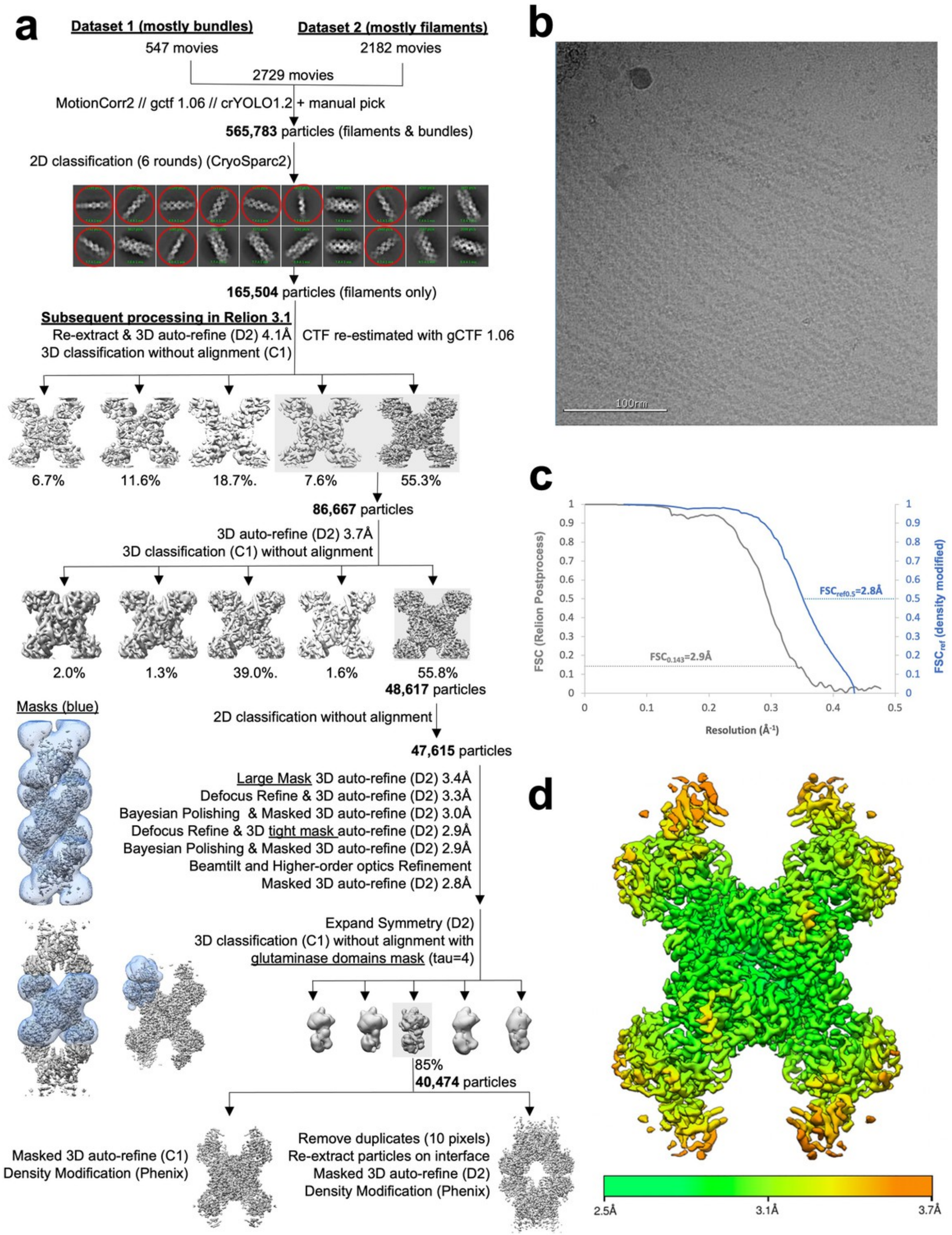

Figure 9.1: Image processing of substrate-bound Ura8 filaments. (a) Flowchart overview of the data processing strategy. (b) Example micrograph from the dataset. (c) FSC curve from Relion postprocess and Phenix density modification. (d) Local resolution estimation.

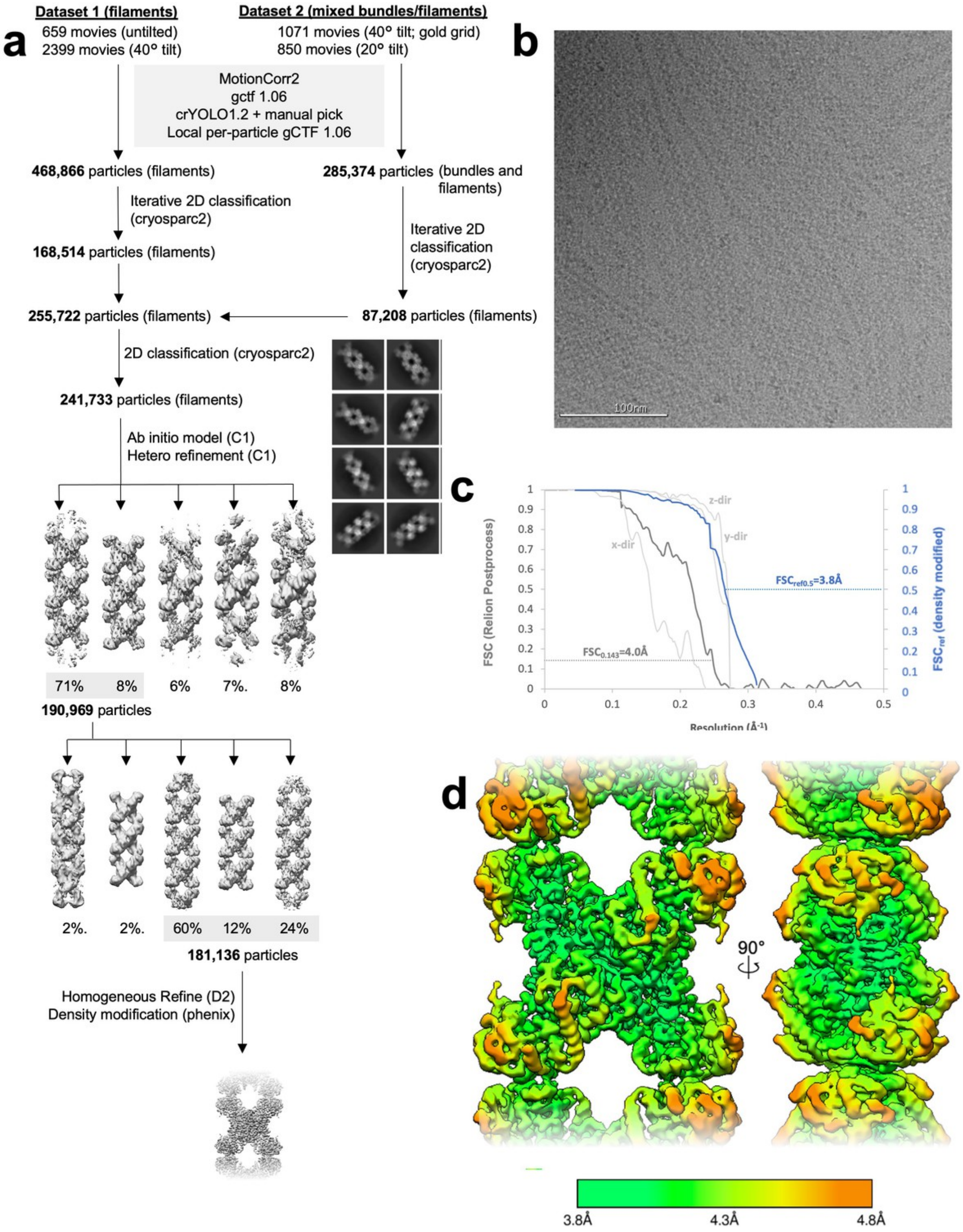

Figure 9.2: Image processing of product-bound Ura8 filaments. (a) Flowchart overview of the data processing strategy. (b) Example micrograph from the dataset. (c) FSC curve from Relion postprocess and Phenix density modification. Light gray is 3D FSC for X/Y/Z directions. (d) Local resolution estimation.

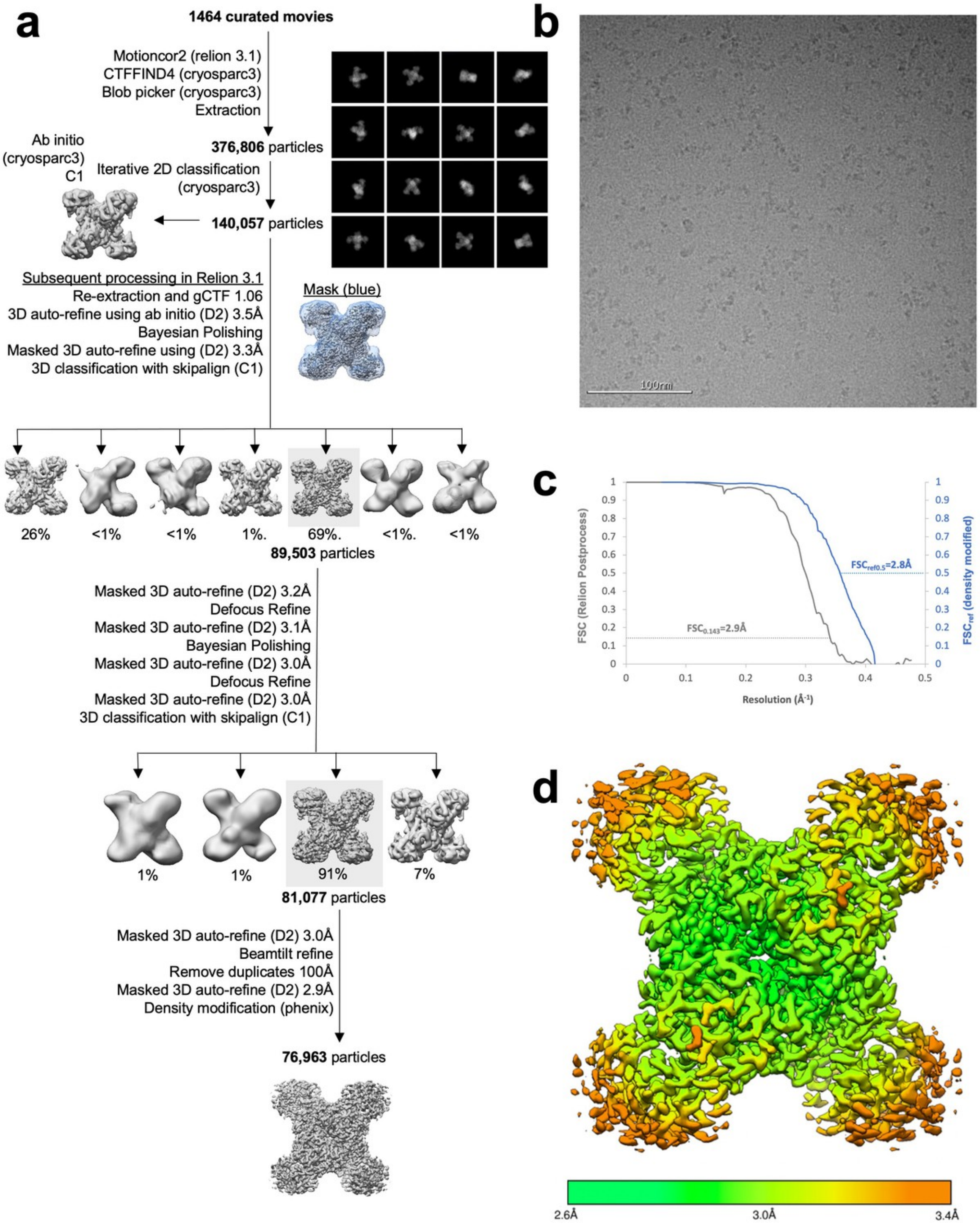

Figure 9.3: Image processing of substrate-bound Ura8 tetramers. (a) Flowchart overview of the data processing strategy. (b) Example micrograph from the dataset. (c) FSC curve from Relion postprocess and Phenix density modification. (d) Local resolution estimation.

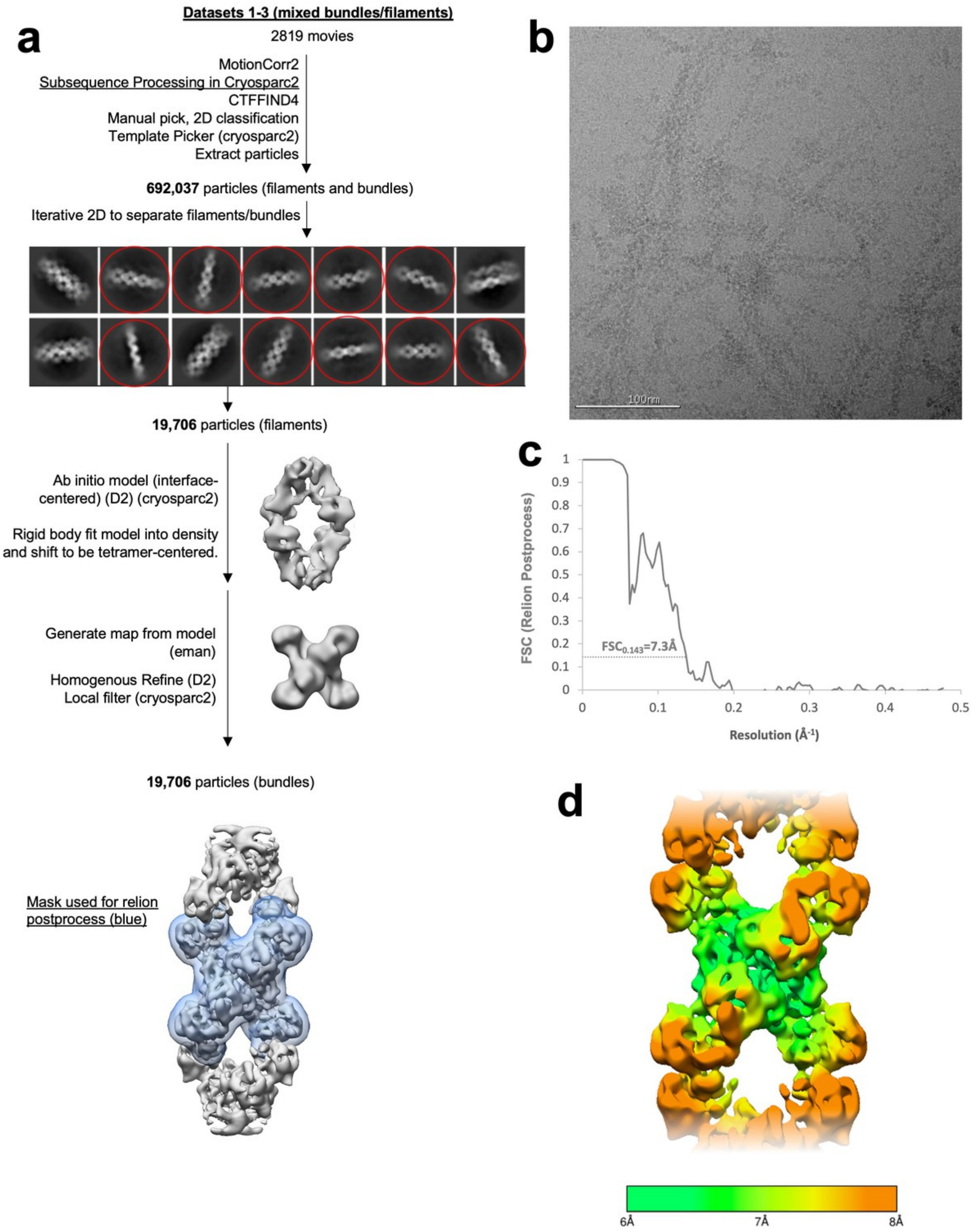

Figure 9.4: Image processing of substrate-bound Ura7 filaments. (a) Flowchart overview of the data processing strategy. (b) Example micrograph from the dataset. (c) FSC curve from Relion postprocess. (d) Local resolution estimation.

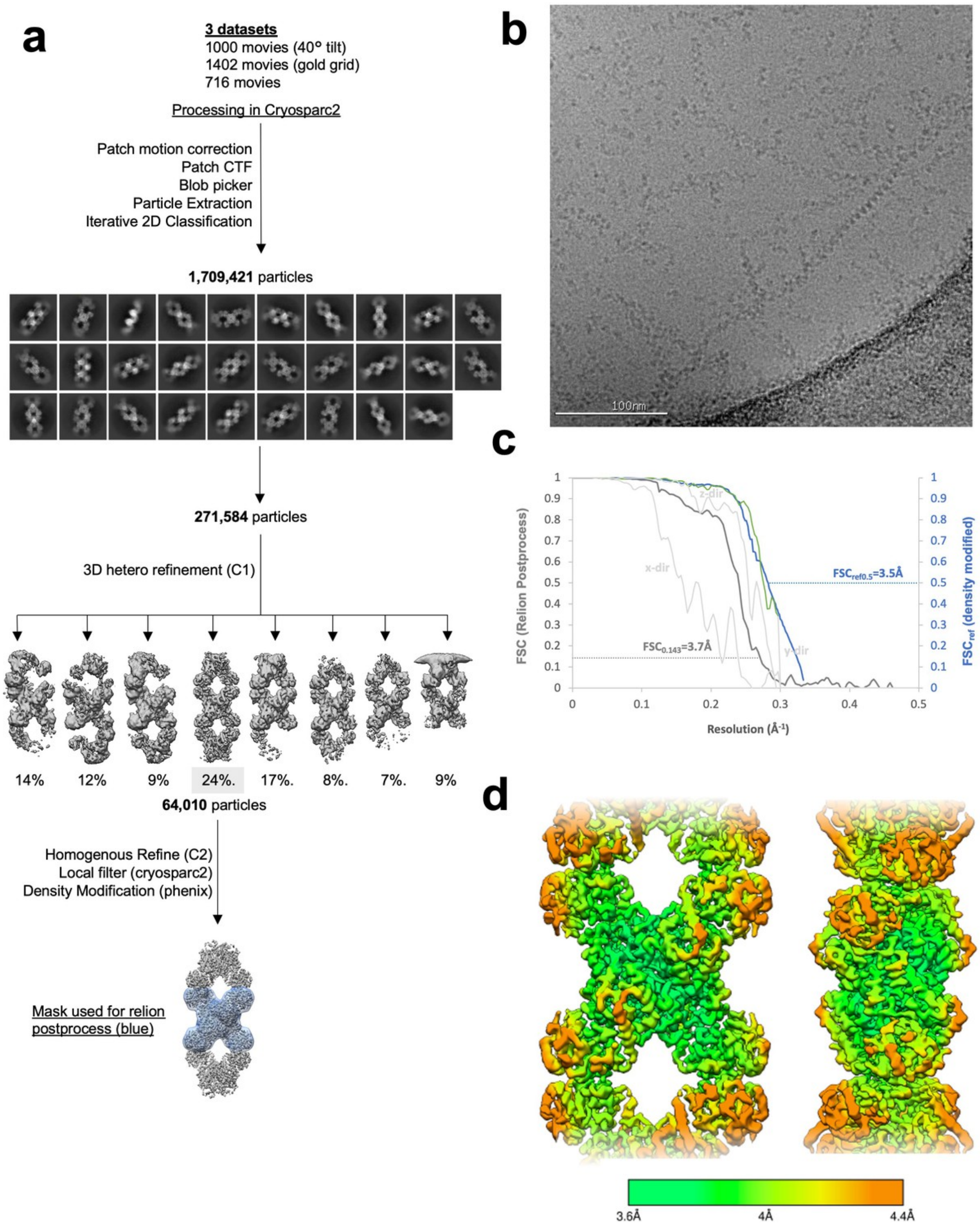

Figure 9.5: Image processing of product-bound Ura7 filaments. (a) Flowchart overview of the data processing strategy. (b) Example micrograph from the dataset. (c) FSC curve from Relion postprocess and Phenix density modification. Light gray is 3D FSC for X/Y/Z directions. (d) Local resolution estimation.

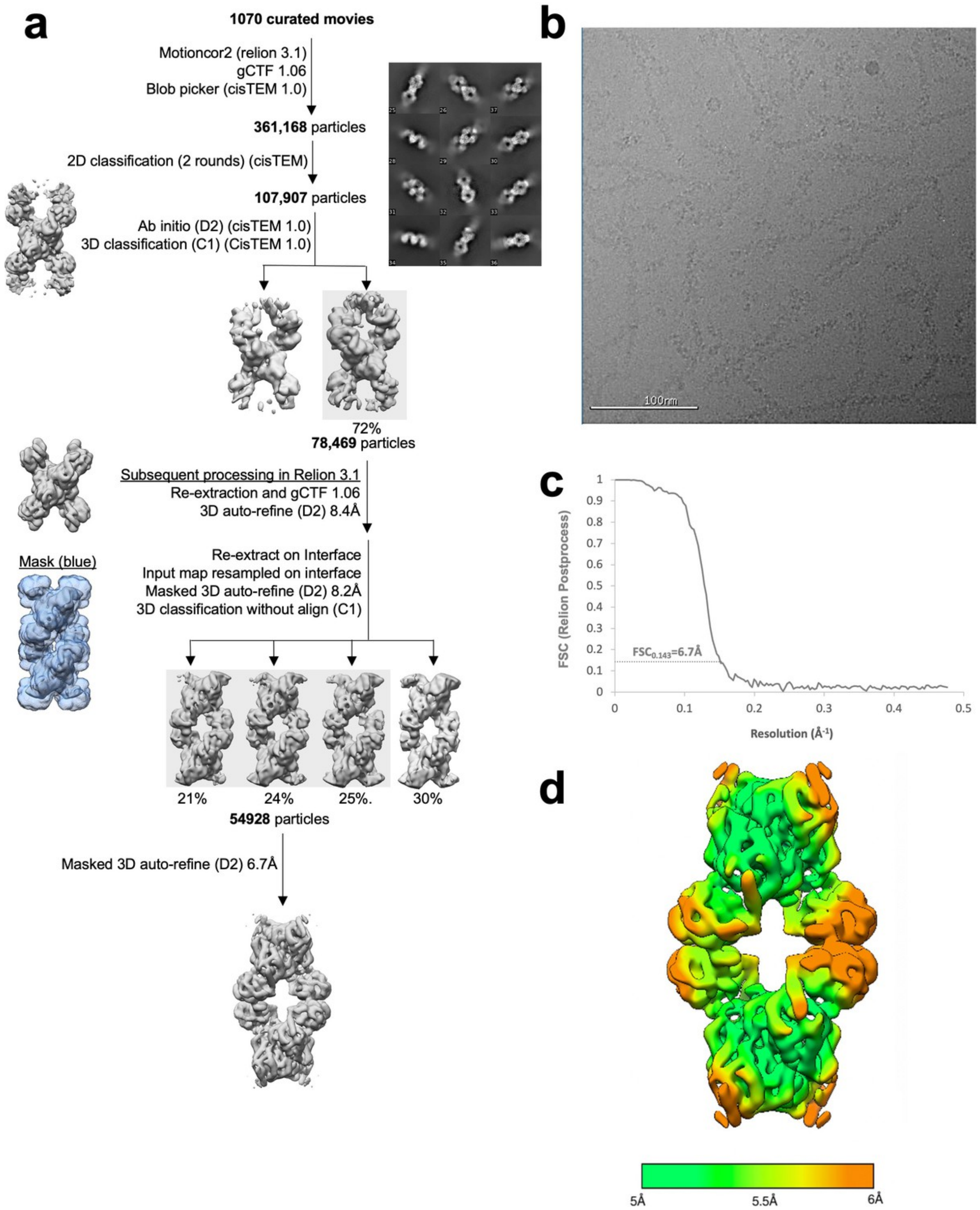

Figure 9.6: Image processing of substrate-bound Ura7-H360R at pH 7.5. (a) Flowchart overview of the data processing strategy. (b) Example micrograph from the dataset on continuous carbon. (c) FSC curve from Relion postprocess. (d) Local resolution estimation.

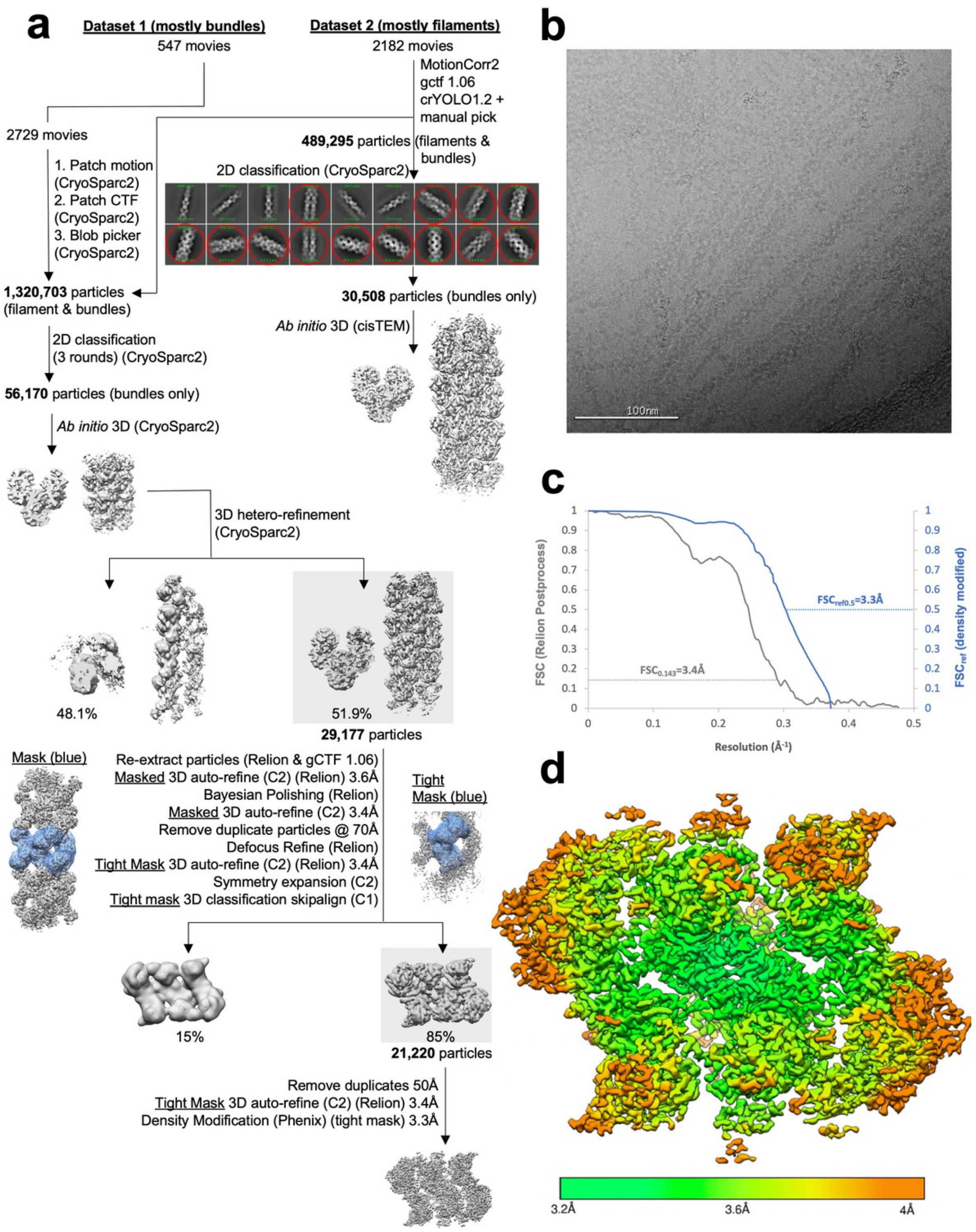

Figure 9.7: Image processing of substrate-bound Ura8 bundles. (a) Flowchart overview of the data processing strategy. (b) Example micrograph from the dataset. (c) FSC curve from Relion postprocess and Phenix density modification. (d) Local resolution estimation.

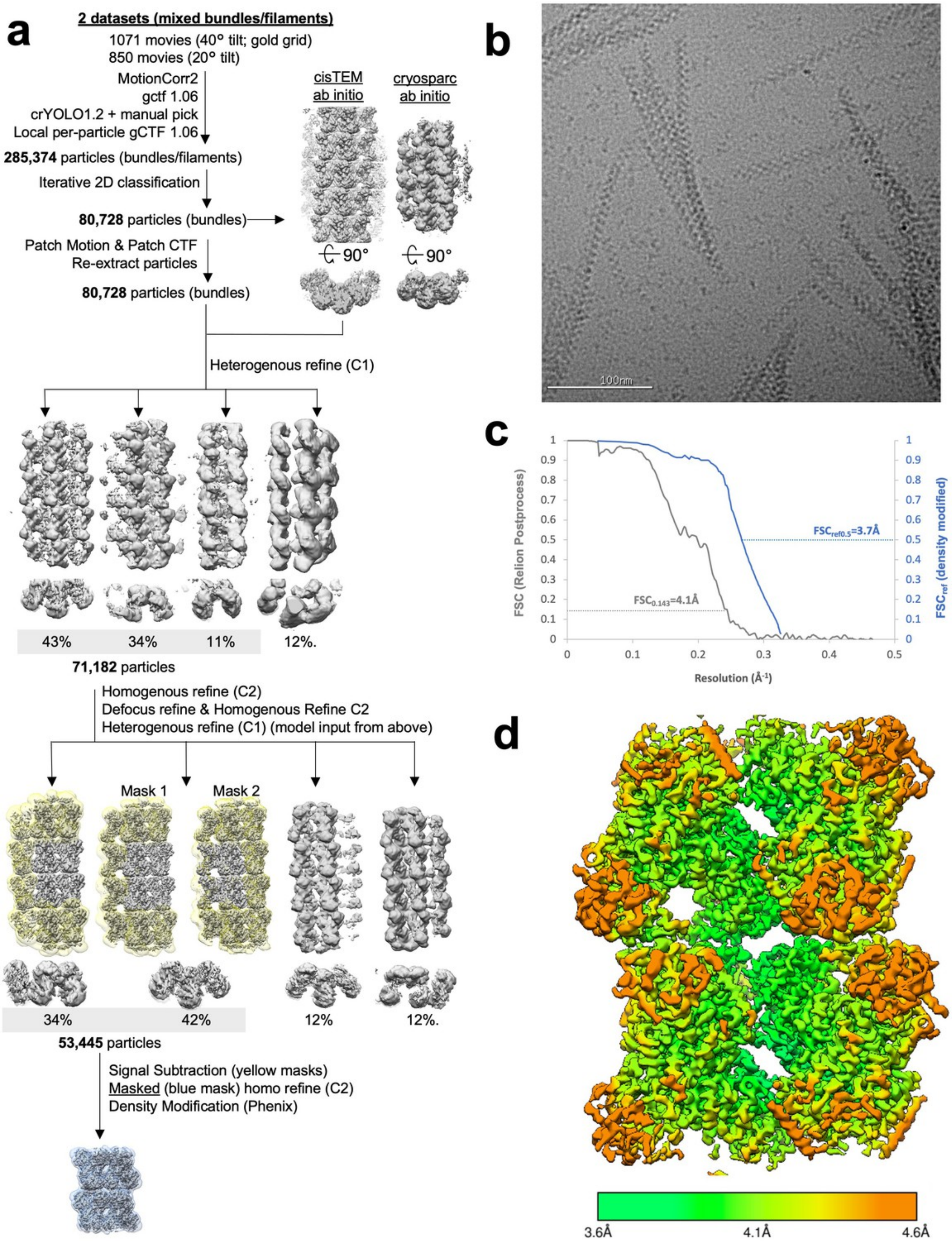

Figure 9.8: Image processing of product-bound Ura8 bundles. (a) Flowchart overview of the data processing strategy. (b) Example micrograph from the dataset. (c) FSC curve from Relion postprocess and Phenix density modification. (d) Local resolution estimation.

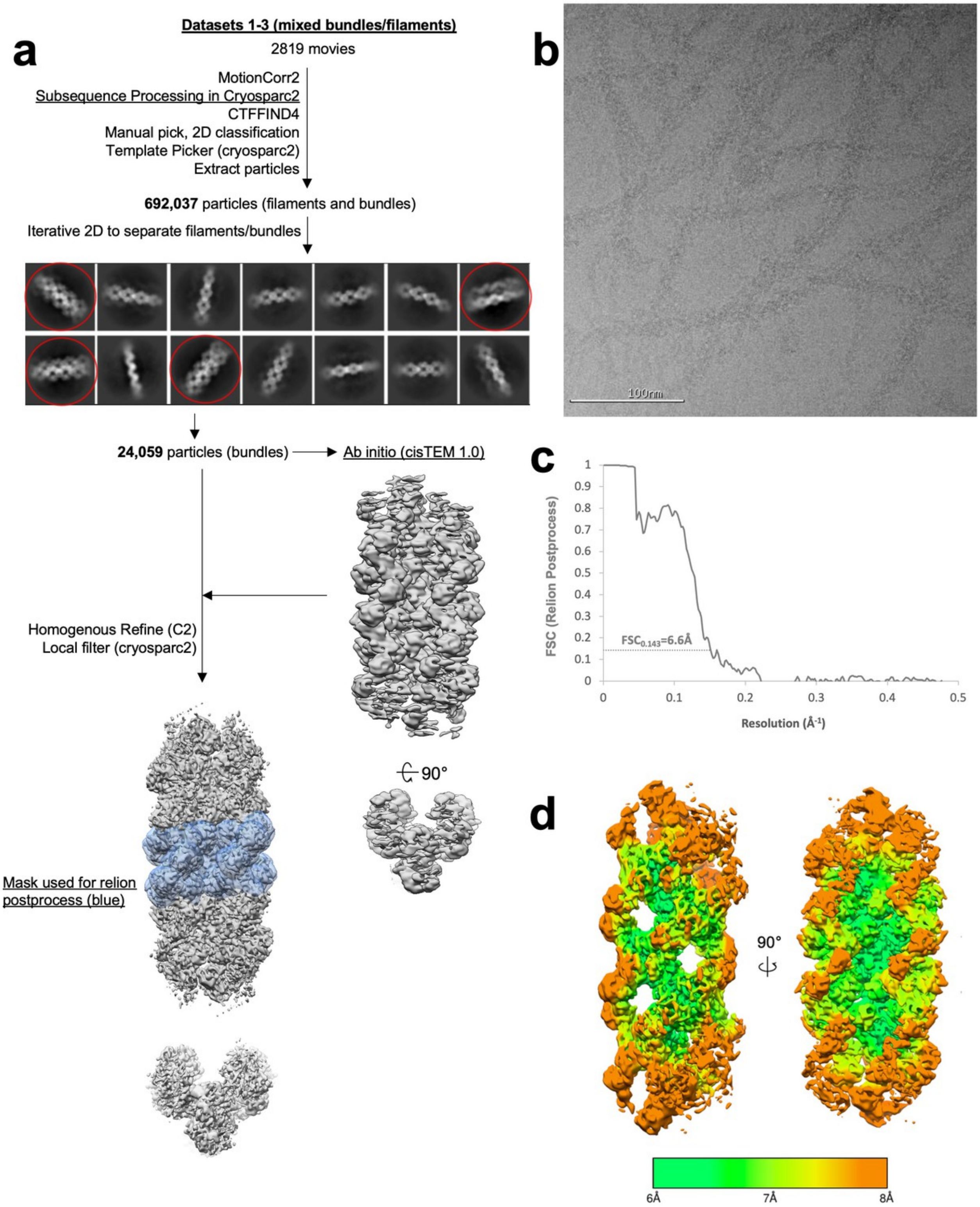

Figure 9.9: Image processing of substrate-bound Ura7 bundles. (a) Flowchart overview of the data processing strategy. (b) Example micrograph from the dataset. (c) FSC curve from Relion postprocess. (d) Local resolution estimation.

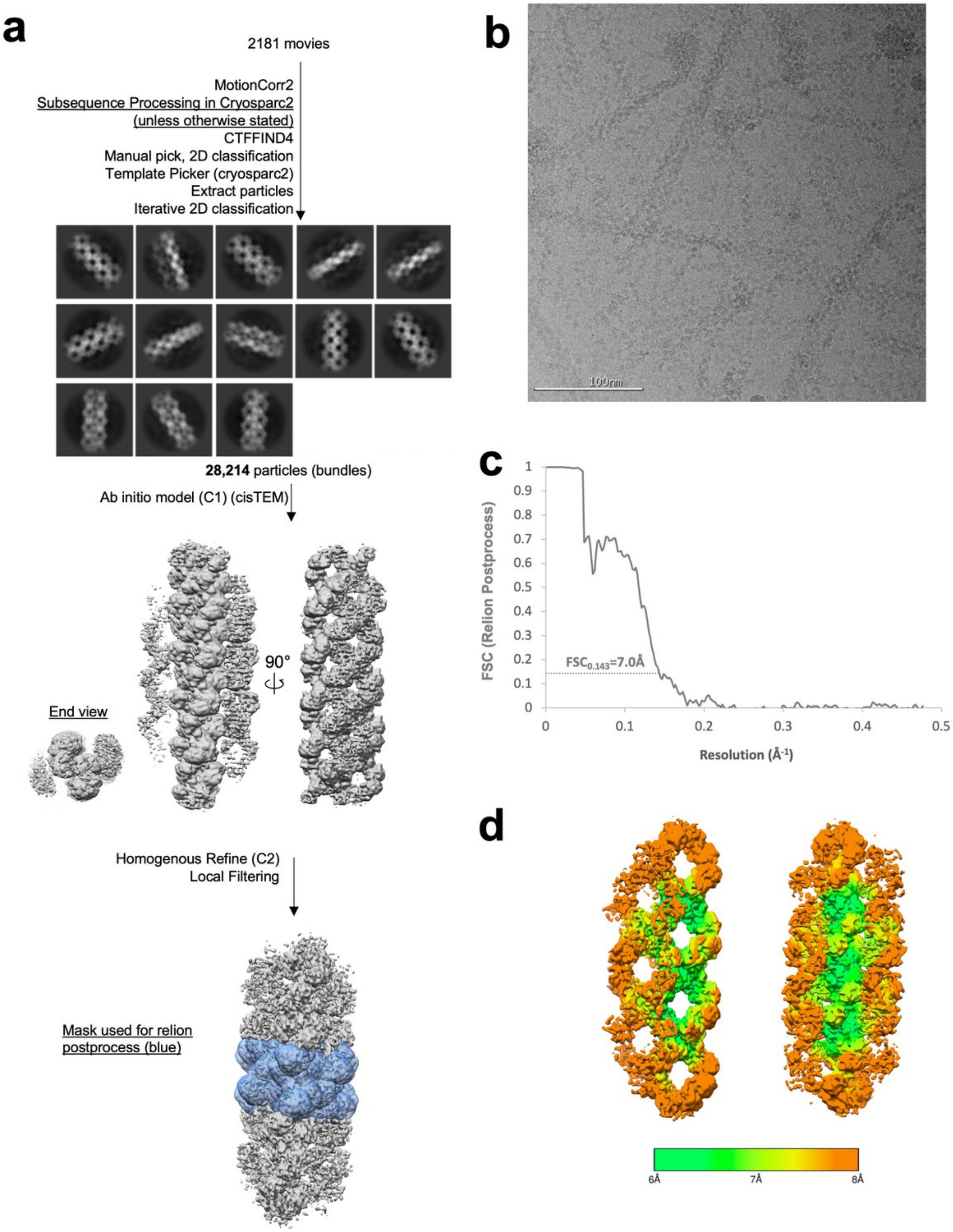

Figure 9.10: Image processing of product-bound Ura7 bundles. (a) Flowchart overview of the data processing strategy. (b) Example micrograph from the dataset. (c) FSC curve from Relion postprocess. (d) Local resolution estimation.

Table 1. Cryo-EM Data Collection and Refinement Statistics

	Ura8 substrates filament	**Ura8 Substrates Bundle**	**Ura8 substrates tetramer**	**Ura8 products filament**	**Ura8 products bundle**	**Ura7 substrates filament**	**Ura7 substrates bundle**	**Ura7 products filament**	**Ura7 products bundle**	**Ura7 H360R substrates filament**
Number of micrographs	2729	2729	1464	4979	1921	2819	2819	3118	2181	1070
Nominal magnification	130,000X									
Voltage	300 kV									
Electron Fluence	90e^-/Å^2									
Pixel size	1.05Å									
Defocus range	-0.4 to -1.9µm	-0.4 to -1.9µm	-1.2 to -5.5µm	-0.4 to -9.0µm	-0.4 to -7.0µm	-0.8 to -2.2µm	-0.8 to -2.2µm	-0.4 to -7.0µm	-1.0 to -2.2µm	-0.9 to -3.5µm

EMDB ID	EMD-24512	EMD-24581	EMD-24497	EMD-24516	EMD-24579	EMD-24566	EMD-24575	EMD-24560	EMD-24576	EMD-24578
PDB code	7RL0	7RNR	7RKH	7RL5	7RNL	7RMF	7RMK	7RMC	7RMO	7RMV
Map resolution 0.143 FSC	2.9Å	3.4Å	2.9Å	4.0Å	4.1Å	7.3Å	6.6Å	3.7Å	7.0Å	6.7Å
Density Modified Resolution 0.5Ref	2.8Å	3.3Å	2.8Å	3.8Å	3.7Å	n/a	n/a	3.5Å	n/a	n/a
Symmetry Imposed	D2	C2	D2	D2	C2	D2	C2	D2	C2	D2
Number of particles	40,474	21,220	76,963	181,136	53,445	19,706	24,059	64,010	28,214	54,928

Map Sharpening B Factor	-32Å^2	-33Å^2	-74Å^2	-142Å^2	-67Å^2	-235Å^2	-140Å^2	-51Å^2	-186Å^2	-40Å^2
Model composition										
ligands	ATP/UTP	ATP/UTP	ATP/UTP	CTP	CTP	ATP/UTP	ATP/UTP	CTP	CTP	ATP/UTP
R.M.S. deviations										
Bond lengths (Å)	0.64	0.63	0.63	0.66	0.7	0.69	0.69	0.62	0.63	0.71
Bond angles (°)	1.09	1.04	1.04	1.09	1.13	1.06	1.06	1.03	1.03	1.07
Validation										
Molprobity Score	0.98	1.35	1.09	1.59	1.66	1.56	2.06	1.40	1.73	2.30
Clash Score	0.94	4.74	0.9	3.2	3.48	2.31	10.33	1.51	4.62	15.84

Poor Rotamers (%)	1.21	0.61	1.64	2.05	1.43	1.88	1.88	1.65	1.66	2.09
Ramachandran Plot										
Favored (%)	97	98	97	96	94	95	95	95	95	95
Allowed (%)	2	2	3	3	6	4	4	5	4	5
Outliers (%)	0	0	0	0	0	0	0	0	0	0

Table 2. CTPS Polymer Architecture Characteristics

	Ura8 prods filament	Ura8 subs filament	Ura8 subs tetramer	Ura8 prods bundle	Ura8 subs bundle	Ura7 prods filament	Ura7 Subs filament	Ura7 prods bundle	Ura7 subs bundle
Domain rotation relative to product-bound filament	n/a	4°	7.4°	1.7°	6.9°	n/a	7.7°	1.4°	6.2°
Filament twist	5°	17.1°	n/a	3.9°	15.9°	7.4°	18.2°	7.3°	17.3°
Filament rise	102.6Å	102.3Å	n/a	103Å	101.8Å	102.7Å	103.4Å	102.8Å	104.5Å

Table 3. X-ray diffraction data

Resolution	3.5 (3.50-3.55)
Mean I/σ (I)	8.86 (1.54)
Completeness	99.9 (100)
Rmerge (%)	34.3 (200.7)
Rmeas	35.5 (207.7)
Multiplicity	14.8 (15.2)
Total Reflections	1234712 (9737)
Unique Reflections	83426 (640)
Unit Cell	140Å x 185Å x 256Å
Space Group	P212121
Rwork	0.28
Rfree	0.32

*values in parentheses are highest resolution shells.

Table 4. Kinetic activity parameters for yeast CTPS and mutants.

	Wild type	**H360A**	**H360R**
Max	2.68 ± 0.05	3.60 ± 0.08	1.18 ± 0.05
Min	0.00 ± 0.00	0.00 ± 0.00	0.00 ± 0.00
S50	161.07 ± 14.24	160.03 ± 5.67	229.72 ± 9.26
Hill	1.53 ± 0.15	1.45 ± 0.03	0.80 ± 0.15

* Error represents standard error of the mean (SEM)

Table 5. CTPS Bundle Buried Surface Area and Putative Contact Residues.

Ura8 Product-bound Bundle Contacts						
BSA	**domains**	**Monomer 0**	**Monomer 1**	**Monomer 2**	**Monomer 3**	**Monomer 4**
93Å^2	Glu-Glu	465,468,515	381, 384, 429,430,432,433			
173Å^2	Glu-Glu	471,472,476,477†,480-483	348,350†,352,353†			
113Å^2	Glu-Glu	566,567*,570,571	354-356,358			
240Å^2	Link-AL	275,276,277*,278,280†,281†		222†,225,226*,230,236,237†		
48Å^2	Link-AL	272,274			168,169,171,172	

Ura8 Substrate-bound Bundle Contacts						
471Å^2	Link-Glu	275,276,277*,278-282,284,285,288			348,350,380-383,384*,387,412,416,423,425,426,429,430,432,433,435	
98Å^2	AL-Glu	136-139			353,354	
185Å^2	Glu-AL	471,472,477,481,506,507,526,527		168-172,174,272,274		
152Å^2	Glu-AL	563,567,570,571 †		100 †, 105-107,109,119,123,126,127,130		
88Å^2	Glu-AL	465,468,471,476,483,484	233,236-238,263			

151Å^2	AL-Glu	168-172,174				469,471,472,477
167Å^2	AL-Glu	100,105-107, 123†,126*, 130†				561,563,564†,567† ,571

* predicted hydrogen bond

† predicted salt bridge

Table 6. Yeast Strains Used

Number	**Background**	**Genotype**
yJMK001	W303	URA7-GFP::KanMx
yJMK002	W303	URA7H360A
yJMK003	W303	URA7H360A-GFP::KanMx
yJMK004	W303	URA7H360R
yJMK005	W303	URA7H360R-GFP::KanMx
yJMK006	W303	URA8-GFP::KanMx
yJMK007	W303	URA8-mCherry::KanMx
yJMK008	W303	URA8H360A
yJMK009	W303	URA8H360A-GFP::KanMx

References

Alford RF, Leaver-Fay A, Jeliazkov JR, O'Meara MJ, DiMaio FP, Park H, Shapovalov MV, Renfrew PD, Mulligan VK, Kappel K, Labonte JW, Pacella MS, Bonneau R, Bradley P, Dunbrack RL, Das R, Baker D, Kuhlman B, Kortemme T, Gray JJ. 2017. The Rosetta All-Atom Energy Function for Macromolecular Modeling and Design. *J Chem Theory Comput* **13**:3031–3048. doi:10.1021/acs.jctc.7b00125

Allison AC, Eugui EM. 1993. Inhibitors of de novo purine and pyrimidine synthesis as immunosuppressive drugs. *Transplant Proc* **25**:8–18.

Andreadis C, Hulme L, Wensley K, Liu J-L. 2019. The TOR pathway modulates cytoophidium formation in Schizosaccharomyces pombe. *Journal of Biological Chemistry* **294**:14686–14703. doi:10.1074/jbc.RA119.009913

Azzam G, Liu J-L. 2013. Only One Isoform of Drosophila melanogaster CTP Synthase Forms the Cytoophidium. *PLoS Genet* **9**:e1003256. doi:10.1371/journal.pgen.1003256

Barry RM, Bitbol A-F, Lorestani A, Charles EJ, Habrian CH, Hansen JM, Li H-J, Baldwin EP, Wingreen NS, Kollman JM, Gitai Z. 2014. Large-scale filament formation inhibits the activity of CTP synthetase. *eLife* **3**:e03638. doi:10.7554/eLife.03638

Berg AA van den, Lenthe H van, Kipp JBA, Korte D de, Kuilenburg ABP van, Gennip AH van. 1995. Cytidine triphosphate (ctp) synthetase activity during cell cycle progression in normal and malignant t-lymphocytic cells. *European Journal of Cancer* **31**:108–112. doi:10.1016/0959-8049(94)00442-8

Binda C, Bossi RT, Wakatsuki S, Arzt S, Coda A, Curti B, Vanoni MA, Mattevi A. 2000. Cross-Talk and Ammonia Channeling between Active Centers in the Unexpected Domain Arrangement of Glutamate Synthase. *Structure* **8**:1299–1308. doi:10.1016/S0969-2126(00)00540-2

Boehlein SK, Rosa-Rodriguez JG, Schuster SM, Richards NGJ. 1997. Catalytic Activity of the N-Terminal Domain of *Escherichia coli* Asparagine Synthetase B Can Be Reengineered by Single-Point Mutation. *J Am Chem Soc* **119**:5785–5791. doi:10.1021/ja9613668

Botstein D, Chervitz SA, Cherry JM. 1997. Yeast as a Model Organism. *Science* **277**:1259–1260.

Broach JR. 1991. RAS genes in Saccharomyces cerevisiae: signal transduction in search of a pathway. *Trends in Genetics* **7**:28–33. doi:10.1016/0168-9525(91)90018-L

Brockman RW, Shaddix SC, Williams M, Nelson JA, Rose LM, Schabel Jr. FM. 1975. The Mechanism of Action of 3-Deazauridine in Tumor Cells Sensitive and Resistant to Arabinosylcytosine*. *Annals of the New York Academy of Sciences* **255**:501–521. doi:10.1111/j.1749-6632.1975.tb29254.x

Buchanan JM. 1973. The AmidotransferasesAdvances in Enzymology and Related Areas of Molecular Biology. John Wiley & Sons, Ltd. pp. 91–183. doi:10.1002/9780470122846.ch2

Carcamo WC, Satoh M, Kasahara H, Terada N, Hamazaki T, Chan JYF, Yao B, Tamayo S, Covini G, von Mühlen CA, Chan EKL. 2011. Induction of Cytoplasmic Rods and Rings Structures by Inhibition of the CTP and GTP Synthetic Pathway in Mammalian Cells. *PLoS ONE* **6**:e29690. doi:10.1371/journal.pone.0029690

Chang C-C, Jeng Y-M, Peng M, Keppeke GD, Sung L-Y, Liu J-L. 2017. CTP synthase forms the cytoophidium in human hepatocellular carcinoma. *Experimental Cell Research* **361**:292–299. doi:10.1016/j.yexcr.2017.10.030

Chang C-C, Keppeke GD, Sung L-Y, Liu J-L. 2018. Interfilament interaction between IMPDH and CTPS cytoophidia. *The FEBS Journal* **285**:3753–3768. doi:10.1111/febs.14624

Chang Y-F, Carman GM. 2008. CTP synthetase and its role in phospholipid synthesis in the yeast Saccharomyces cerevisiae. *Progress in Lipid Research* **47**:333–339. doi:10.1016/j.plipres.2008.03.004

Chiarelli LR, Mori G, Orena BS, Esposito M, Lane T, de Jesus Lopes Ribeiro AL, Degiacomi G, Zemanová J, Szádocka S, Huszár S, Palčeková Z, Manfredi M, Gosetti F, Lelièvre J, Ballell L, Kazakova E, Makarov V, Marengo E, Mikusova K, Cole ST, Riccardi G, Ekins S, Pasca MR. 2018. A multitarget approach to drug discovery inhibiting Mycobacterium tuberculosis PyrG and PanK. *Sci Rep* **8**:3187. doi:10.1038/s41598-018-21614-4

Choi M-G, Park T-S, Carman GM. 2003. Phosphorylation of Saccharomyces cerevisiae CTP Synthetase at Ser424 by Protein Kinases A and C Regulates Phosphatidylcholine Synthesis by the CDP-choline Pathway. *Journal of Biological Chemistry* **278**:23610–23616. doi:10.1074/jbc.M303337200

Chovancova E, Pavelka A, Benes P, Strnad O, Brezovsky J, Kozlikova B, Gora A, Sustr V, Klvana M, Medek P, Biedermannova L, Sochor J, Damborsky J. 2012. CAVER 3.0: A Tool for the Analysis of Transport Pathways in Dynamic Protein Structures. *PLoS Comput Biol* **8**:e1002708. doi:10.1371/journal.pcbi.1002708

Cohen RJ, Judith A J, George B. B. 1976. The functional relationship between polymerization and catalytic activity of beef liver glutamate dehydrogenase: II. *jmb* **108**:179–199. doi:https://doi.org/10.1016/S0022-2836(76)80102-7

Croll TI. 2018. ISOLDE: a physically realistic environment for model building into low-resolution electron-density maps. *Acta Cryst D* **74**:519–530. doi:10.1107/S2059798318002425

Curnow AW, Hong K -w., Yuan R, Kim S -i., Martins O, Winkler W, Henkin TM, Soll D. 1997. Glu-tRNAGln amidotransferase: A novel heterotrimeric enzyme required for correct decoding of glutamine codons during translation. *Proceedings of the National Academy of Sciences* **94**:11819–11826. doi:10.1073/pnas.94.22.11819

Daumann M, Hickl D, Zimmer D, DeTar RA, Kunz H-H, Möhlmann T. 2018. Characterization of filament-forming CTP synthases from Arabidopsis thaliana. *The Plant Journal* **96**:316–328. doi:10.1111/tpj.14032

Dayton S, Turka A, Thompson B, Mitchell S. 1992. Comparison of the Effects of Mizoribine with Those of Azathioprine, 6-Mercaptopurine, and Mycophenolic Acid on T Lymphocyte Proliferation and Purine Ribonucleotide Metabolism 671–676.

Egelman EH. 2003. Actin's prokaryotic homologs. *Current Opinion in Structural Biology* **13**:244–248. doi:10.1016/S0959-440X(03)00027-7

Ellims PH, Gan TE, Medley G. 1983. Cytidine Triphosphate Synthetase Activity in Lymphoproliferative Disorders. *Cancer Res* **43**:1432–1435.

Emsley P, Cowtan K. 2004. *Coot* : model-building tools for molecular graphics. *Acta Crystallogr D Biol Crystallogr* **60**:2126–2132. doi:10.1107/S0907444904019158

Endrizzi JA, Kim H, Anderson PM, Baldwin EP. 2004. Crystal Structure of *Escherichia coli* Cytidine Triphosphate Synthetase, a Nucleotide-Regulated Glutamine Amidotransferase/ATP-Dependent Amidoligase Fusion Protein and Homologue of Anticancer and Antiparasitic Drug Targets [†,‡]. *Biochemistry* **43**:6447–6463. doi:10.1021/bi0496945

Fagerberg L, Hallström BM, Oksvold P, Kampf C, Djureinovic D, Odeberg J, Habuka M, Tahmasebpoor S, Danielsson A, Edlund K, Asplund A, Sjöstedt E, Lundberg E, Szigyarto CA-K, Skogs M, Takanen JO, Berling H, Tegel H, Mulder J, Nilsson P, Schwenk JM, Lindskog C, Danielsson F, Mardinoglu A, Sivertsson Å, von Feilitzen K, Forsberg M, Zwahlen M, Olsson I, Navani S, Huss M, Nielsen J, Ponten F, Uhlén M. 2014. Analysis of the Human Tissue-specific Expression by Genome-wide Integration of Transcriptomics and Antibody-based Proteomics. *Mol Cell Proteomics* **13**:397–406. doi:10.1074/mcp.M113.035600

Fairbanks LD, Bofill M, Ruckemann K, Simmonds HA. 1995. Importance of Ribonucleotide Availability to Proliferating T-lymphocytes from Healthy Humans. *Journal of Biological Chemistry* **270**:29682–29689. doi:10.1074/jbc.270.50.29682

Frenz B, Walls AC, Egelman EH, Veesler D, DiMaio F. 2017. RosettaES: a sampling strategy enabling automated interpretation of difficult cryo-EM maps. *Nat Methods* **14**:797–800. doi:10.1038/nmeth.4340

Frey TG, Eisenberg D, Eiserling FA. 1975. Glutamine synthetase forms three- and seven-stranded helical cables. *Proc Natl Acad Sci U S A* **72**:3402–3406.

Garcia-Seisdedos H, Empereur-Mot C, Elad N, Levy ED. 2017. Proteins evolve on the edge of supramolecular self-assembly. *Nature* **548**:244–247. doi:10.1038/nature23320

Goffeau A, Barrell BG, Bussey H, Davis RW, Dujon B, Feldmann H, Galibert F, Hoheisel JD, Jacq C, Johnston M, Louis EJ, Mewes HW, Murakami Y, Philippsen P, Tettelin H, Oliver SG. 1996. Life with 6000 Genes. *Science*. doi:10.1126/science.274.5287.546

Goto M, Omi R, Nakagawa N, Miyahara I, Hirotsu K. 2004. Crystal Structures of CTP Synthetase Reveal ATP, UTP, and Glutamine Binding Sites. *Structure* **12**:1413–1423. doi:10.1016/j.str.2004.05.013

Gou K-M, Chang C-C, Shen Q-J, Sung L-Y, Liu J-L. 2014. CTP synthase forms cytoophidia in the cytoplasm and nucleus. *Experimental Cell Research* **323**:242–253. doi:10.1016/j.yexcr.2014.01.029

Grant T, Rohou A, Grigorieff N. 2018. cisTEM, user-friendly software for single-particle image processing. *eLife* **7**:e35383. doi:10.7554/eLife.35383

Hansen JM, Horowitz A, Lynch EM, Farrell DP, Quispe J, DiMaio F, Kollman JM. 2021. Cryo-EM structures of CTP synthase filaments reveal mechanism of pH-sensitive assembly during budding yeast starvation. *eLife* **10**:e73368. doi:10.7554/eLife.73368

Hofer A, Steverding D, Chabes A, Brun R, Thelander L. 2001. Trypanosoma brucei CTP synthetase: A target for the treatment of African sleeping sickness. *Proceedings of the National Academy of Sciences* **98**:6412–6416. doi:10.1073/pnas.111139498

Huang X, Holden HM, Raushel FM. 2001. Channeling of Substrates and Intermediates in Enzyme-Catalyzed Reactions. *Annual Review of Biochemistry* **70**:149–180. doi:10.1146/annurev.biochem.70.1.149

Hunkeler M, Hagmann A, Stuttfeld E, Chami M, Guri Y, Stahlberg H, Maier T. 2018. Structural basis for regulation of human acetyl-CoA carboxylase. *Nature* **558**:470–474. doi:10.1038/s41586-018-0201-4

Hurlbert RB, Kammen HO. 1960. Formation of Cytidine Nucleotides from Uridine Nucleotides by Soluble Mammalian Enzymes: Requirements for Glutamine and Guanosine Nucleotides. *Journal of Biological Chemistry* **235**:443–449. doi:10.1016/S0021-9258(18)69544-4

Ingerson-Mahar M, Briegel A, Werner JN, Jensen GJ, Gitai Z. 2010. The metabolic enzyme CTP synthase forms cytoskeletal filaments. *Nat Cell Biol* **12**:739–746. doi:10.1038/ncb2087

Jiang Q, Lin L, Wang T. 2006. A New Model for Apoptosis Research: Yeast. *Progress in Biochemistry and Biophysics* **0**.

JimÉnez BM, O'sullivan WJ. 1994. CTP synthetase and enzymes of pyrimidine ribonucleotide metabolism in Giardia intestinalis. *International Journal for Parasitology* **24**:713–718. doi:10.1016/0020-7519(94)90125-2

Johnson MC, Kollman JM. 2020. Cryo-EM structures demonstrate human IMPDH2 filament assembly tunes allosteric regulation. *eLife* **9**:e53243. doi:10.7554/eLife.53243

Kaibuchi K, Takai Y, Nishizuka Y. 1985. Protein kinase C and calcium ion in mitogenic response of macrophage-depleted human peripheral lymphocytes. *Journal of Biological Chemistry* **260**:1366–1369. doi:10.1016/S0021-9258(18)89597-7

Kassel KM, Au DR, Higgins MJ, Hines M, Graves LM. 2010. Regulation of Human Cytidine Triphosphate Synthetase 2 by Phosphorylation*. *Journal of Biological Chemistry* **285**:33727–33736. doi:10.1074/jbc.M110.178566

Kemp RG. 1971. Rabbit Liver Phosphofructokinase. *Journal of Biological Chemistry* **246**:245–252. doi:10.1016/S0021-9258(18)62556-6

Keppeke GD, Calise SJ, Chan EKL, Andrade LEC. 2015. Assembly of IMPDH2-Based, CTPS-Based, and Mixed Rod/Ring Structures Is Dependent on Cell Type and Conditions of Induction. *Journal of Genetics and Genomics* **42**:287–299. doi:10.1016/j.jgg.2015.04.002

Kizaki H, Williams JC, Morris HP, Weber G. 1980. Increased Cytidine 5′-Triphosphate Synthetase Activity in Rat and Human Tumors. *Cancer Res* **40**:3921–3927.

Kleinschmidt AK, Moss J, Lane D. 1969. Acetyl coenzyme A carboxylase: filamentous nature of the animal enzymes. *Science* **166**:1276–1278.

Levitzki A, Koshland DE. 1971. Cytidine triphosphate synthetase. Covalent intermediates and mechanisms of action. *Biochemistry* **10**:3365–3371. doi:10.1021/bi00794a008

Lewis DA, Villafranca JJ. 1989. Investigation of the mechanism of CTP synthetase using rapid quench and isotope partitioning methods. *Biochemistry* **28**:8454–8459. doi:10.1021/bi00447a027

Li H, Ye F, Ren J-Y, Wang P-Y, Du L-L, Liu J-L. 2018. Active transport of cytoophidia in Schizosaccharomyces pombe. *The FASEB Journal* **32**:5891–5898. doi:10.1096/fj.201800045RR

Lieberman I. 1956. ENZYMATIC AMINATION OF URIDINE TRIPHOSPHATE TO CYTIDINE TRIPHOSPHATE. *Journal of Biological Chemistry* **222**:765–775. doi:10.1016/S0021-9258(20)89934-7

Liu J-L. 2010. Intracellular compartmentation of CTP synthase in Drosophila. *Journal of Genetics and Genomics* **37**:281–296. doi:10.1016/S1673-8527(09)60046-1

Long CW, Pardee AB. 1967. Cytidine Triphosphate Synthetase of Escherichia coli B. *Journal of Biological Chemistry* **242**:4715–4721. doi:10.1016/S0021-9258(18)99515-3

Lynch EM, DiMattia MA, Albanese S, Zundert GCP van, Hansen JM, Quispe JD, Kennedy MA, Verras A, Borrelli K, Toms AV, Kaila N, Kreutter KD, McElwee JJ, Kollman JM. 2021. Structural basis for isoform-specific inhibition of human CTPS1. *PNAS* **118**. doi:10.1073/pnas.2107968118

Lynch EM, Hicks DR, Shepherd M, Endrizzi JA, Maker A, Hansen JM, Barry RM, Gitai Z, Baldwin EP, Kollman JM. 2017. Human CTP synthase filament structure reveals the active enzyme conformation. *Nat Struct Mol Biol* **24**:507–514. doi:10.1038/nsmb.3407

Lynch EM, Kollman JM. 2020. Coupled structural transitions enable highly cooperative regulation of human CTPS2 filaments. *Nat Struct Mol Biol* **27**:42–48. doi:10.1038/s41594-019-0352-5

MacDonnell JE, Lunn FA, Bearne SL. 2004. Inhibition of E. coli CTP synthase by the “positive” allosteric effector GTP. *Biochimica et Biophysica Acta (BBA) - Proteins and Proteomics* **1699**:213–220. doi:10.1016/j.bbapap.2004.03.002

Maehara Y, Nakamura H, Nakane Y, Kawai K, Okamoto M, Nagayama S, Shirasaka T, Fujii S. 1982. Activities of various enzymes of pyrimidine nucleotide and DNA syntheses in normal and neoplastic human tissues. *Gann* **73**:289–298.

Martin E, Palmic N, Sanquer S, Lenoir C, Hauck F, Mongellaz C, Fabrega S, Nitschké P, Esposti MD, Schwartzentruber J, Taylor N, Majewski J, Jabado N, Wynn RF, Picard C, Fischer A, Arkwright PD, Latour S. 2014. CTP synthase 1 deficiency in humans reveals its central role in lymphocyte proliferation. *Nature* **510**:288–292. doi:10.1038/nature13386

Massière F, Badet-Denisot M-A. 1998. The mechanism of glutamine-dependent amidotransferases. *CMLS, Cell Mol Life Sci* **54**:205–222. doi:10.1007/s000180050145

Mendz G l., Jimenez B m., Hazell S l., Gero A m., O’Sullivan W j. 1994. De novo synthesis of pyrimidine nucleotides by Helicobacter pylori. *Journal of Applied Bacteriology* **77**:1–8. doi:10.1111/j.1365-2672.1994.tb03036.x

Meuth M. 1989. The molecular basis of mutations induced by deoxyribonucleoside triphosphate pool imbalances in mammalian cells. *Experimental Cell Research* **181**:305–316. doi:10.1016/0014-4827(89)90090-6

Miller RE, Shelton E, Stadtman ER. 1974. Zinc-induced paracrystalline aggregation of glutamine synthetase. *Archives of Biochemistry and Biophysics* **163**:155–171. doi:10.1016/0003-9861(74)90465-2

Mouilleron S, Golinelli-Pimpaneau B. 2007. Conformational changes in ammonia-channeling glutamine amidotransferases. *Current Opinion in Structural Biology*, Catalysis and regulation / Proteins **17**:653–664. doi:10.1016/j.sbi.2007.09.003

Munder MC, Midtvedt D, Franzmann T, Nüske E, Otto O, Herbig M, Ulbricht E, Müller P, Taubenberger A, Maharana S, Malinovska L, Richter D, Guck J, Zaburdaev V, Alberti S. 2016. A pH-driven transition of the cytoplasm from a fluid- to a solid-like state promotes entry into dormancy. *eLife* **5**:e09347. doi:10.7554/eLife.09347

Nadkarni AK, McDonough VM, Yang W-L, Stukey JE, Ozier-Kalogeropoulos O, Carman GM. 1995. Differential Biochemical Regulation of the URA7- and URA8-encoded CTP Synthetases from Saccharomyces cerevisiae. *Journal of Biological Chemistry* **270**:24982–24988. doi:10.1074/jbc.270.42.24982

Narayanaswamy R, Levy M, Tsechansky M, Stovall GM, O'Connell JD, Mirrielees J, Ellington AD, Marcotte EM. 2009. Widespread reorganization of metabolic enzymes into reversible assemblies upon nutrient starvation. *PNAS* **106**:10147–10152. doi:10.1073/pnas.0812771106

Noree C, Begovich K, Samilo D, Broyer R, Monfort E, Wilhelm JE. 2019. A quantitative screen for metabolic enzyme structures reveals patterns of assembly across the yeast metabolic network. *MBoC* **30**:2721–2736. doi:10.1091/mbc.E19-04-0224

Noree C, Sato BK, Broyer RM, Wilhelm JE. 2010. Identification of novel filament-forming proteins in Saccharomyces cerevisiae and Drosophila melanogaster. *Journal of Cell Biology* **190**:541–551. doi:10.1083/jcb.201003001

Orij R, Postmus J, Ter Beek A, Brul S, Smits GJ. 2009. In vivo measurement of cytosolic and mitochondrial pH using a pH-sensitive GFP derivative in Saccharomyces cerevisiae reveals a relation between intracellular pH and growth. *Microbiology* **155**:268–278. doi:10.1099/mic.0.022038-0

Ozier-Kalogeropoulos O, Adeline M-T, Yang W-L, Carman GM, Lacroute F. 1994. Use of synthetic lethal mutants to clone and characterize a novel CTP synthetase gene in Saccharomyces cerevisiae. *Molec Gen Genet* **242**:431–439. doi:10.1007/BF00281793

Ozyamak E, Kollman J, Agard DA, Komeili A. 2013. The Bacterial Actin MamK: IN VITRO ASSEMBLY BEHAVIOR AND FILAMENT ARCHITECTURE* *This work was supported, in whole or in part, by National Institutes of Health Grants R01GM084122 (to A. K.) and GM031627 (to D. A. A.). This work was also supported by a Howard Hughes Medical Institute grant (to D. A. A.). This article contains supplemental Figs. S1–S11. *Journal of Biological Chemistry* **288**:4265–4277. doi:10.1074/jbc.M112.417030

Park CK, Horton NC. 2019. Structures, functions, and mechanisms of filament forming enzymes: a renaissance of enzyme filamentation. *Biophys Rev* **11**:927–994. doi:10.1007/s12551-019-00602-6

Park T-S, O'Brien DJ, Carman GM. 2003. Phosphorylation of CTP Synthetase on Ser36, Ser330, Ser354, and Ser454 Regulates the Levels of CTP and Phosphatidylcholine Synthesis in Saccharomyces cerevisiae. *Journal of Biological Chemistry* **278**:20785–20794. doi:10.1074/jbc.M301394200

Park T-S, Ostrander DB, Pappas A, Carman GM. 1999. Identification of Ser ^{424} as the Protein Kinase A Phosphorylation Site in CTP Synthetase from *Saccharomyces cerevisiae*. *Biochemistry* **38**:8839–8848. doi:10.1021/bi990784x

Petrovska I, Nüske E, Munder MC, Kulasegaran G, Malinovska L, Kroschwald S, Richter D, Fahmy K, Gibson K, Verbavatz J-M, Alberti S. 2014. Filament formation by metabolic enzymes is a specific adaptation to an advanced state of cellular starvation. *eLife* **3**:e02409. doi:10.7554/eLife.02409

Pettersen EF, Goddard TD, Huang CC, Couch GS, Greenblatt DM, Meng EC, Ferrin TE. 2004.

UCSF Chimera?A visualization system for exploratory research and analysis. *J Comput Chem* **25**:1605–1612. doi:10.1002/jcc.20084

Postnikoff SDL, Johnson JE, Tyler JK. 2017. The integrated stress response in budding yeast lifespan extension. *Microb Cell* **4**:368–375. doi:10.15698/mic2017.11.597

Punjani A, Rubinstein JL, Fleet DJ, Brubaker MA. 2017. cryoSPARC: algorithms for rapid unsupervised cryo-EM structure determination. *Nat Methods* **14**:290–296. doi:10.1038/nmeth.4169

Purich DL. 1998. Advances in the enzymology of glutamine synthesis. *Adv Enzymol Relat Areas Mol Biol* **72**:9–42. doi:10.1002/9780470123188.ch2

Rambotti P. 1985. Biochemical markers in lymphoproliferative diseases. *Critical Reviews in Oncology/Hematology* **2**:297–321. doi:10.1016/S1040-8428(85)80006-8

Richards, Nigel G. J., Humkey, Robert N., Li, Kai, Meyer, Megan E., Cordova de Sintjago, Tania C. 2010. Tunnels and Intermediates in the Glutamine-Dependent AmidotransferasesComprehensive Natural Products II. Elsevier. pp. 161–230.

Rishavy MA, Cleland WW, Lusty CJ. 2000. ^{15} N Isotope Effects in Glutamine Hydrolysis Catalyzed by Carbamyl Phosphate Synthetase: Evidence for a Tetrahedral Intermediate in the Mechanism. *Biochemistry* **39**:7309–7315. doi:10.1021/bi000435z

Rohou A, Grigorieff N. 2015. CTFFIND4: Fast and accurate defocus estimation from electron micrographs. *Journal of Structural Biology*, Recent Advances in Detector Technologies and Applications for Molecular TEM **192**:216–221. doi:10.1016/j.jsb.2015.08.008

Roux B, Walsh CT. 1992. p-Aminobenzoate synthesis in Escherichia coli: kinetic and mechanistic characterization of the amidotransferase PabA. *Biochemistry* **31**:6904–6910. doi:10.1021/bi00145a006

Sakamoto K, Ishibashi Y, Adachi R, Matsumoto S, Oki H, Kamada Y, Sogabe S, Zama Y, Sakamoto J, Tani A. 2017. Identification of cytidine-5-triphosphate synthase1-selective inhibitory peptide from random peptide library displayed on T7 phage. *Peptides* **94**:56–63. doi:10.1016/j.peptides.2017.06.007

Scheres SHW. 2012. RELION: Implementation of a Bayesian approach to cryo-EM structure determination. *J Struct Biol* **180**:519–530. doi:10.1016/j.jsb.2012.09.006

Schmidt TT, Reyes G, Gries K, Ceylan CÜ, Sharma S, Meurer M, Knop M, Chabes A, Hombauer H. 2017. Alterations in cellular metabolism triggered by *URA7* or *GLN3* inactivation cause imbalanced dNTP pools and increased mutagenesis. *Proc Natl Acad Sci USA* **114**:E4442–E4451. doi:10.1073/pnas.1618714114

Schmitz H, Hurlbert RB, Potter VR, Brumm AF, White DM. 1954. NUCLEOTIDE METABOLISM. *Journal of Biological Chemistry* **209**:41–54. doi:10.1016/S0021-9258(18)65529-2

Sheff MA, Thorn KS. 2004. Optimized cassettes for fluorescent protein tagging in Saccharomyces cerevisiae. *Yeast* **21**:661–670. doi:10.1002/yea.1130

Shen Q-J, Kassim H, Huang Y, Li H, Zhang J, Li G, Wang P-Y, Yan J, Ye F, Liu J-L. 2016. Filamentation of Metabolic Enzymes in Saccharomyces cerevisiae. *Journal of Genetics and Genomics* **43**:393–404. doi:10.1016/j.jgg.2016.03.008

Simon JA, Bedalov A. 2004. Yeast as a model system for anticancer drug discovery. *Nat Rev Cancer* **4**:481–487. doi:10.1038/nrc1372

Simonet JC, Foster MJ, Lynch EM, Kollman JM, Nicholas E, O'Reilly AM, Peterson JR. 2020. CTP synthase polymerization in germline cells of the developing *Drosophila* egg supports egg production. *Biology Open* bio.050328. doi:10.1242/bio.050328

Stoddard PR, Lynch EM, Farrell DP, Dosey AM, DiMaio F, Williams TA, Kollman JM, Murray AW, Garner EC. 2020. Polymerization in the actin ATPase clan regulates hexokinase activity in yeast. *Science* **367**:1039–1042. doi:10.1126/science.aay5359

Strochlic TI, Stavrides KP, Thomas SV, Nicolas E, O'Reilly AM, Peterson JR. 2014. Ack kinase regulates CTP synthase filaments during Drosophila oogenesis. *EMBO reports* **15**:1184–1191. doi:10.15252/embr.201438688

Suloway C, Pulokas J, Fellmann D, Cheng A, Guerra F, Quispe J, Stagg S, Potter CS, Carragher B. 2005. Automated molecular microscopy: the new Leginon system. *J Struct Biol* **151**:41–60. doi:10.1016/j.jsb.2005.03.010

Tamborini L, Pinto A, Smith TK, Major LL, Iannuzzi MC, Cosconati S, Marinelli L, Novellino E, Lo Presti L, Wong PE, Barrett MP, De Micheli C, Conti P. 2012. Synthesis and Biological Evaluation of CTP Synthetase Inhibitors as Potential Agents for the Treatment of African Trypanosomiasis. *ChemMedChem* **7**:1623–1634. doi:10.1002/cmdc.201200304

Terwilliger TC, Ludtke SJ, Read RJ, Adams PD, Afonine PV. 2020. Improvement of cryo-EM maps by density modification. *Nat Methods* **17**:923–927. doi:10.1038/s41592-020-0914-9

Thevelein JM. 1994. Signal transduction in yeast. *Yeast* **10**:1753–1790. doi:10.1002/yea.320101308

Thoden JB, Raushel FM, Benning MM, Rayment I, Holden HM. 1999. The structure of carbamoyl phosphate synthetase determined to 2.1 Å resolution. *Acta Cryst D* **55**:8–24. doi:10.1107/S0907444998006234

Traut TW. 1994. Physiological concentrations of purines and pyrimidines. *Mol Cell Biochem* **140**:1–22. doi:10.1007/BF00928361

Traut TW, Evans DR. 1988. Enzymes of Nucleotide Metabolism: The Significance of Subunit Size and Polymer Size for Biological Function and Regulatory Propertie. *Critical Reviews in Biochemistry* **23**:121–169. doi:10.3109/10409238809088318

Trotta PP, Wellner VP, Pinkus LM, Meister A. 1973. Observations on the pH Dependence of the Glutaminase Activity of a Glutamine Amidotransferase, Carbamylphosphate Synthetase. *Proceedings of the National Academy of Sciences* **70**:2717–2721. doi:10.1073/pnas.70.10.2717

van den BERG AA, van LENTHE H, Busch S, de KORTE D, Roos D, van KUILENBURG ABP, van GENNIP AH. 1993. Evidence for transformation-related increase in CTP synthetase activity in situ in human lymphoblastic leukemia. *European Journal of Biochemistry* **216**:161–167. doi:10.1111/j.1432-1033.1993.tb18128.x

van den Berg AA, van Lenthe H, Busch S, de Korte D, van Kuilenburg AB, van Gennip AH. 1994. The roles of uridine-cytidine kinase and CTP synthetase in the synthesis of CTP in malignant human T-lymphocytic cells. *Leukemia* **8**:1375–1378.

Verschuur AC, Van Gennip AH, Leen R, Meinsma R, Voute PA, Van Kuilenburg ABP. 2000. In vitro inhibition of cytidine triphosphate synthetase activity by cyclopentenyl cytosine in paediatric acute lymphocytic leukaemia. *British Journal of Haematology* **110**:161–169. doi:10.1046/j.1365-2141.2000.02136.x

Verschuur AC, van Gennip AH, Muller EJ, Voûte PA, van Kuilenburg ABP. 1998. Increased Activity of Cytidinetriphosphate Synthetase in Pediatric Acute Lymphoblastic Leukemia In: Griesmacher A, Müller MM, Chiba P, editors. Purine and Pyrimidine Metabolism in Man IX, Advances in Experimental Medicine and Biology. Boston, MA: Springer US. pp. 667–671. doi:10.1007/978-1-4615-5381-6_129

von der Saal W, Anderson PM, Villafranca JJ. 1985. Mechanistic investigations of Escherichia coli cytidine-5'-triphosphate synthetase. Detection of an intermediate by positional isotope exchange experiments. *Journal of Biological Chemistry* **260**:14993–14997. doi:10.1016/S0021-9258(18)95692-9

Wagner T, Merino F, Stabrin M, Moriya T, Antoni C, Apelbaum A, Hagel P, Sitsel O, Raisch T, Prumbaum D, Quentin D, Roderer D, Tacke S, Siebolds B, Schubert E, Shaikh TR, Lill P, Gatsogiannis C, Raunser S. 2019. SPHIRE-crYOLO is a fast and accurate fully automated particle picker for cryo-EM. *Commun Biol* **2**:1–13. doi:10.1038/s42003-019-0437-z

Webb BA, Dosey AM, Wittmann T, Kollman JM, Barber DL. 2017. The glycolytic enzyme phosphofructokinase-1 assembles into filaments. *Journal of Cell Biology*

216:2305–2313. doi:10.1083/jcb.201701084

Weeks A, Lund L, Raushel FM. 2006. Tunneling of intermediates in enzyme-catalyzed reactions. *Current Opinion in Chemical Biology*, Analytical techniques / Mechanisms **10**:465–472. doi:10.1016/j.cbpa.2006.08.008

Wendland J. 2003. PCR-based methods facilitate targeted gene manipulations and cloning procedures. *Curr Genet* **44**:115–123. doi:10.1007/s00294-003-0436-x

Whelan J, Phear G, Yamauchi M, Meuth M. 1993. Clustered base substitutions in CTP synthetase conferring drug resistance in Chinese hamster ovary cells. *Nat Genet* **3**:317–322. doi:10.1038/ng0493-317

Williams JC, Kizaki H, Weber G, Morris HP. 1978. Increased CTP synthetase activity in cancer cells. *Nature* **271**:71–73. doi:10.1038/271071a0

Winderickx J, Holsbeeks I, Lagatie O, Giots F, Thevelein J, de Winde H. 2003. From feast to famine; adaptation to nutrient availability in yeast In: Hohmann S, Mager WH, editors. Yeast Stress Responses, Topics in Current Genetics. Berlin, Heidelberg: Springer. pp. 305–386. doi:10.1007/3-540-45611-2_7

Wu Z, Liu J-L. 2019. Cytoophidia respond to nutrient stress in Drosophila. *Experimental Cell Research* **376**:159–167. doi:10.1016/j.yexcr.2019.02.003

Wylie JL, Wang LL, Tipples G, McClarty G. 1996. A Single Point Mutation in CTP Synthetase of Chlamydia trachomatis Confers Resistance to Cyclopentenyl Cytosine *. *Journal of Biological Chemistry* **271**:15393–15400. doi:10.1074/jbc.271.26.15393

Yang W-L, Bruno MEC, Carman GM. 1996. Regulation of Yeast CTP Synthetase Activity by Protein Kinase C. *Journal of Biological Chemistry* **271**:11113–11119. doi:10.1074/jbc.271.19.11113

Yang W-L, Carman GM. 1996. Phosphorylation and Regulation of CTP Synthetase from Saccharomyces cerevisiae by Protein Kinase A. *Journal of Biological Chemistry* **271**:28777–28783. doi:10.1074/jbc.271.46.28777

Yang W-L, McDonough VM, Ozier-Kalogeropoulos O, Adeline M-T, Flocco MT, Carman GM. 1994. Purification and Characterization of CTP Synthetase, the Product of the URA7 Gene in Saccharomyces cerevisiae. *Biochemistry* **33**:10785–10793. doi:10.1021/bi00201a028

Yoshida T, Nasu H, Namba E, Ubukata O, Yamashita M 2012. 2012. Discovery of a compound that acts as a bacterial PyrG (CTP synthase) inhibitor. *Journal of Medical Microbiology* **61**:1280–1285. doi:10.1099/jmm.0.046052-0

Zhang J, Liu J-L. 2019. Temperature-sensitive cytoophidium assembly in Schizosaccharomyces pombe. *Journal of Genetics and Genomics* **46**:423–432. doi:10.1016/j.jgg.2019.09.002

Zhang K. 2016. Gctf: Real-time CTF determination and correction. *Journal of Structural Biology* **193**:1–12. doi:10.1016/j.jsb.2015.11.003

Zhang N, Cao L. 2017. Starvation signals in yeast are integrated to coordinate metabolic reprogramming and stress response to ensure longevity. *Curr Genet* **63**:839–843. doi:10.1007/s00294-017-0697-4

Zhang S, Ding K, Shen Q-J, Zhao S, Liu J-L. 2018. Filamentation of asparagine synthetase in Saccharomyces cerevisiae. *PLoS Genet* **14**:e1007737. doi:10.1371/journal.pgen.1007737

Zhang S, Feng H-C, Liu J-L. 2021. ASNS disruption shortens CTPS cytoophidia in Saccharomyces cerevisiae. *G3 Genes|Genomes|Genetics* **11**:jkaa060. doi:10.1093/g3journal/jkaa060

Zheng SQ, Palovcak E, Armache J-P, Verba KA, Cheng Y, Agard DA. 2017. MotionCor2: anisotropic correction of beam-induced motion for improved cryo-electron microscopy. *Nat Methods* **14**:331–332. doi:10.1038/nmeth.4193

Zhou S, Xiang H, Liu J-L. 2020. CTP synthase forms cytoophidia in archaea. *Journal of Genetics and Genomics* **47**:213–223. doi:10.1016/j.jgg.2020.03.004

Zhou X, Guo C-J, Chang C-C, Zhong J, Hu H-H, Lu G-M, Liu J-L. 2021. Structural basis for ligand binding modes of CTP synthase. *PNAS* **118**. doi:10.1073/pnas.2026621118

Zhou X, Guo C-J, Hu H-H, Zhong J, Sun Q, Liu D, Zhou S, Chang CC, Liu J-L. 2019. Drosophila CTP synthase can form distinct substrate- and product-bound filaments. *Journal of Genetics and Genomics* **46**:537–545. doi:10.1016/j.jgg.2019.11.006